Dinàmica no lineal de sistemes làsers: potencials de Lyapunov i diagrames de bifurcacions

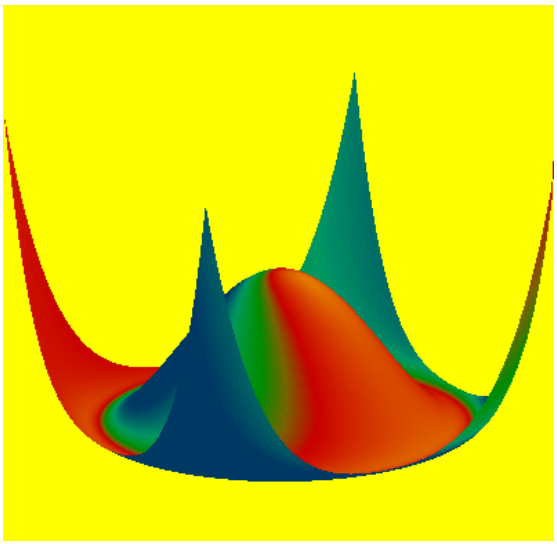

Departament de Física

Universitat de les Illes Balears

Març de 2002

Memòria presentada per Catalina Mayol Serra
per optar al Grau de Doctora en Ciències Físiques
per la Universitat de les Illes Balears.

Part III

Làsers de Classe B

Capítol 7

Làsers de Classe B: Potencial de Lyapunov

En aquest capítol s'estudia la dinàmica del làser de classe B (capítol 4), primer a partir de l'anàlisi numèrica de les equacions i, seguidament aquesta dinàmica s'explica emprant el potencial de Lyapunov (capítol 2) que s'obté.

La dinàmica d'un làser de classe B es descriu mitjançant dues equacions d'evolució, una per a l'amplitud lentament variable del camp elèctric dins la cavitat làser i l'altra per al nombre de portadors. El camp elèctric es pot escriure en termes d'intensitat òptica i fase. En el tractament que es fa en aquest capítol, es menyspreen els termes aleatoris, però es manté el valor mig de l'emissió espontània en l'equació per a la intensitat, Eqs. (7.1 - 7.3). En el cas determinístic, les equacions per a la intensitat del camp elèctric i els portadors no depenen de la variable fase del camp, per tant aquesta variable no es considera en el tractament inicial. L'evolució dinàmica de la intensitat i portadors és tal que ambdues variables arriben a l'estat estacionari realitzant oscil·lacions esmorteïdes amb un període que decreix en el temps, Figs. 7.1, 7.2 i 7.3 .

La dinàmica de la intensitat i portadors es pot explicar mitjançant un potencial de Lyapunov. Un estudi similar s'havia realitzat prèviament [Oppo and Politi, 1985], però sense considerar ni el terme de saturació de guany, ni el valor mig del terme d'emissió espontània. En aquest capítol, s'inclouen aquests dos paràmetres en el potencial (7.14). Observant la seva forma, Fig. 7.4, té un únic mínim, i per tant una única solució estable. El moviment cap a aquest mínim té dues components: una conservativa que produeix trajectòries equipotencials i, una d'esmorteïment que és la responsable de decréixer el valor del potencial. Aquests dos efectes combinats condueixen els sistema cap al mínim seguint un moviment espiral. Els paràmetres de saturació de guany i emissió espontània, inclosos en el tractament potencial, són els responsables d'augmentar els coeficients de la part simètrica de la matriu que associa el potencial i les equacions de moviment, i d'incrementar, com a conseqüència, els termes de dissipació.

La fase del camp elèctric, que oscil·la en el temps fins a arribar a un valor

estacionari, es pot incloure fàcilment en la descripció potencial. Així, el conjunt de les tres variables que descriuen el làser de classe B és de tipus flux potencial no relaxacional (2.26), amb el potencial descrit en el paràgraf anterior (només depenent de la intensitat i el nombre de portadors) i la inclusió de termes addicionals (que contenen el paràmetre α) en la matriu antisimètrica que relaciona el potencial amb les equacions del sistema, (7.23).

Cal indicar que el potencial que s'ha obtingut només és vàlid en el cas determinista, a causa que la matriu que relaciona el gradient del potencial amb les equacions dinàmiques no satisfà la condició fluctuació–dissipació (2.35).

A partir de què el potencial en funció del temps és aproximadament constant entre dos pics de la intensitat, Fig. 7.1, es pot estimar el període de les oscil·lacions de relaxació realitzant un símil mecànic i reduint el problema a un d'energia constant. S'obté una relació entre el període i l'energia del sistema (7.26). Del càlcul numèric d'aquesta expressió, Fig. 7.6, s'observa que el període decreix quan el valor del potencial disminueix. Combinant aquest resultat amb el decreixement temporal del potencial, es pot explicar que el període de les oscil·lacions disminueix en el temps. La comparació dels resultats de l'expressió aproximada i el període real de les simulacions és molt acceptable, Fig. 7.7.

De l'expressió aproximada per al període de les oscil·lacions de relaxació, és possible quantificar la seva discrepància amb el valor exacte a prop de l'estat estacionari. La freqüència exacta de les oscil·lacions de relaxació a prop de l'estacionari és la part imaginària dels autovalors de les equacions d'evolució linealitzades al voltant de la solució estacionària. Els resultats que finalment es comparen són les expressions (7.27) i (7.35).

Per poder entendre completament la variació del període en el temps, caldria avaluar la variació temporal del potencial entre dos pics consecutius d'intensitat. Aquesta variació és deguda al termes dissipatius de les equacions de moviment. Encara que no ha sigut possible obtenir–la exactament, s'ha obtingut una expressió simple a partir d'arguments semi–empírics per a la variació temporal del potencial, Eq. (7.39) i Fig. 7.8. Aquesta expressió es basa en l'evolució de les variables en el temps a prop de l'estacionari. La forma resultant pel potencial, combinat amb què el període és linealment relacionat amb el potencial, suggereix una expressió semi–empírica per a l'evolució temporal del període, Eq. (7.40). L'expressió senzilla resultant, decaïment exponencial del període, ajusta no només a l'estacionari, sinó també en el règim transitori, Figs. 7.7 i 7.9.

Chapter 7

Class B Lasers: Lyapunov Potential

In this chapter, we describe the dynamics of class B lasers in terms of a Lyapunov potential function.

7.1 Model

The dynamics of a typical class B laser, for instance a single mode semiconductor laser, can be described in terms of two evolution equations, one for the slowly varying complex amplitude E of the electric field inside the laser cavity and the other for the carriers number N (or electron-hole pairs), Eqs. (4.11) and (4.12) [Agrawal and Dutta, 1986]. These equations include noise terms accounting for the stochastic nature of spontaneous emission and random non–radiative carrier recombination due to thermal fluctuations. Both noise sources are usually assumed to be white Gaussian noise sources.

The equation for the electric field can be written in terms of the optical intensity I (normalized in such a way that I is equal to the number of photons inside the cavity) and the phase ϕ by defining $E = \sqrt{I}\, e^{\mathrm{i}\phi}$. For simplicity, we neglect the explicit random fluctuations terms and retain, as usual [Agrawal and Dutta, 1986], the mean power of the spontaneous emission. The equations are (4.14 - 4.16) without the explicit fluctuating stochastic terms

$$\frac{dI}{dt} = [G(N,I) - \gamma]\, I + 4\,\varepsilon\, N, \tag{7.1}$$

$$\frac{d\phi}{dt} = \frac{1}{2}\,\alpha\,[G(N,I) - \gamma], \tag{7.2}$$

$$\frac{dN}{dt} = \frac{J}{e} - \gamma_N\, N - G(N,I)\, I. \tag{7.3}$$

$G(N,I)$ is the material gain given by

$$G(N,I) = g_N\, \frac{(N - N_o)}{1 + s\, I}. \tag{7.4}$$

Table 7.1: Definitions and typical values of the parameters for semiconductor lasers.

PARAMETERS		VALUES
J/e	Carriers injected per unit time	$>$ threshold
γ	Cavity decay rate	$0.5\,\mathrm{ps}^{-1}$
γ_N	Carrier decay rate	$0.001\,\mathrm{ps}^{-1}$
N_o	Number of carriers at transparency	1.5×10^8
g_N	Differential gain parameter	$1.5 \times 10^{-8}\,\mathrm{ps}^{-1}$
s	Gain saturation parameter	$10^{-8} - 10^{-7}$
ε	Spontaneous emission rate	$10^{-8}\,\mathrm{ps}^{-1}$
α	Linewidth enhancement factor	$3 - 6$

The definitions and typical values of the parameters for some semiconductor lasers are given in Table 7.1. While the first term of Eq. (7.1) accounts for the stimulated emission, the second one accounts for the mean value of the spontaneous emission in the lasing mode. Eqs. (7.1 - 7.3) are written in the reference frame in which the frequency of the *on* state is zero when spontaneous emission noise is neglected. The threshold condition for lasing is obtained by setting $G(N, I) = \gamma$, $I = 0$ and neglecting spontaneous emission. The number of carriers at threshold is given by $N_{th} = N_o + \frac{\gamma}{g_N}$, and the threshold current is $J_{th} = e\gamma_N N_{th}$, and represents the minimum injection current needed to fully compensate the losses. Eq. (7.2) shows that $\dot{\phi}$ is linear with N and slightly (due to the smallness of the saturation parameter s, see Table 7.1) nonlinear with I.

Since in the deterministic case considered henceforth the evolution equations for I and N do not depend on the phase ϕ, we can concentrate only on the evolution of I and N. One can obtain a set of simpler dimensionless equations by performing the following change of variables

$$y = \frac{2\,g_N}{\gamma}\,I,\; z = \frac{g_N}{\gamma}\,(N - N_o),\; \tau = \frac{\gamma}{2}\,t. \tag{7.5}$$

The equations then become

$$\frac{dy}{d\tau} = 2\left(\frac{z}{1+\bar{s}\,y} - 1\right) y + c\,z + d\,, \tag{7.6}$$

$$\frac{dz}{d\tau} = a - b\,z - \frac{z\,y}{1+\bar{s}\,y}, \tag{7.7}$$

where we have defined

$$a = \frac{2\,g_N}{\gamma^2}\left(\frac{J}{e} - \gamma_N\,N_o\right), \tag{7.8}$$

$$b = \frac{2\,\gamma_N}{\gamma}, \tag{7.9}$$

$$
\begin{aligned}
c &= \frac{16\,\varepsilon}{\gamma}, \\
d &= \frac{16\,\varepsilon\,g_N\,N_o}{\gamma^2}, \\
\bar{s} &= \frac{s\,\gamma}{2\,g_N}.
\end{aligned}
\tag{7.10}
$$

The injected current, J, which is externally controlled, is contained in a. The effect of the spontaneous emission term, ε, appears in c and d. Equations (7.6, 7.7) form the basis of our subsequent analysis. The steady states are

$$
y_{st} = \frac{1}{4\,(1+b\,\bar{s})}[2\,(a-b)+d\,(1+b\,\bar{s})+c\,a\,\bar{s}+\sqrt{v}], \tag{7.11}
$$

$$
z_{st} = \frac{a\,(1+\bar{s}\,y_{st})}{b+y_{st}\,(1+b\,\bar{s})}, \tag{7.12}
$$

where the constant v is given by

$$
\begin{aligned}
v &= 4\,(a-b)^2+4\,d\,(a+b)\,(1+b\,\bar{s})+d^2\,(1+b\,\bar{s})^2 \\
&+ c\,[8\,a+4\,a\,\bar{s}\,(a+b)+2\,d\,a\,\bar{s}\,(1+b\,\bar{s})]+c^2\,a^2\,\bar{s}^2.
\end{aligned}
\tag{7.13}
$$

For a value of the injected current below threshold ($J < J_{th}$ or equivalently to $a-b<0$), y_{st} is very small. This corresponds to the *off* solution in which the only emitted light corresponds to the spontaneous emission.

There is another solution for y_{st} given by Eq. (7.11) with a minus sign in front of $\sqrt{v}$ which, however, does not correspond to any possible physical situation, since it yields $y_{st}<0$.

In the absence of noise, saturation and stimulated emission terms, the steady states are: *off* state, $y_{st}=0$, $z_{st}=a/b$ and *on* state, $y_{st}=a-b$, $z_{st}=1$. Above threshold, stimulated emission occurs and the laser operates in the *on* state with large y_{st}. In what follows, we will concentrate on the evolution following the laser switch–on to the *on* state.

It is known that the dynamical evolution of y and z is such that they both reach the steady state by performing damped oscillations [Agrawal and Dutta, 1986] whose period decreases with time. This fact is different from the usual relaxation oscillations that are calculated near the steady state by linearizing the dynamical equations. The time evolution of y and z is shown in Figs. 7.1 and 7.2, while the corresponding projection in the (y,z) phase–plane is shown in Fig. 7.3.

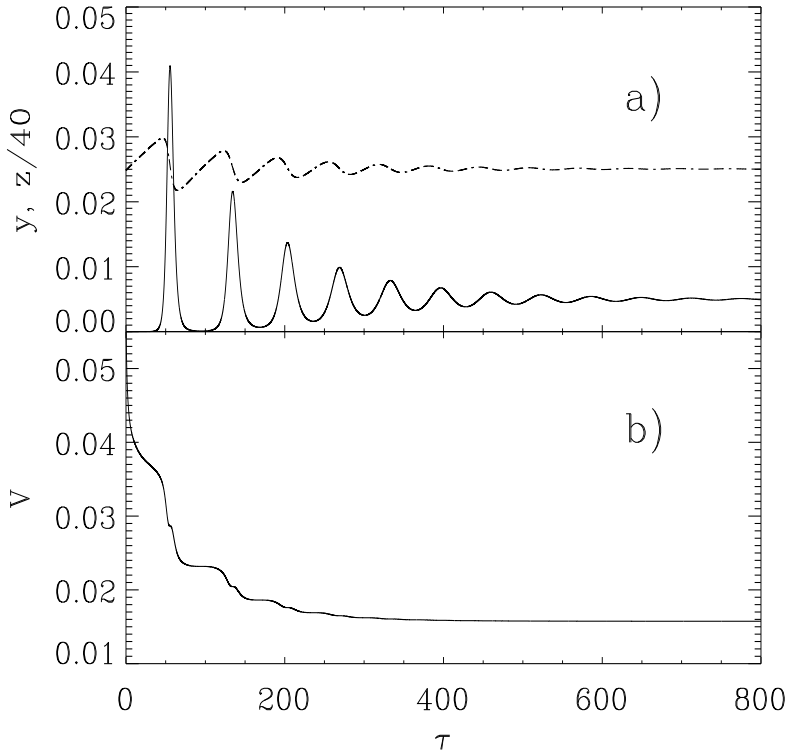

Figure 7.1: a) Normalized intensity, y (solid line) and normalized carriers number, $z/40$ (dot–dashed line) versus time in a class B laser obtained by numerical solution of Eqs. (7.6) and (7.7). b) Plot of the potential (7.14). Parameters: $a = 0.009$, $b = 0.004$, $\bar{s} = 0.5$, $c = 3.2 \times 10^{-9}$, $d = 1.44 \times 10^{-8}$ which correspond to physical parameters in Table 7.1 with $J = 1.2\, J_{th}$. The initial conditions are taken as $y = 5 \times 10^{-8}$ and $z = 0.993$. Dimensionless units.

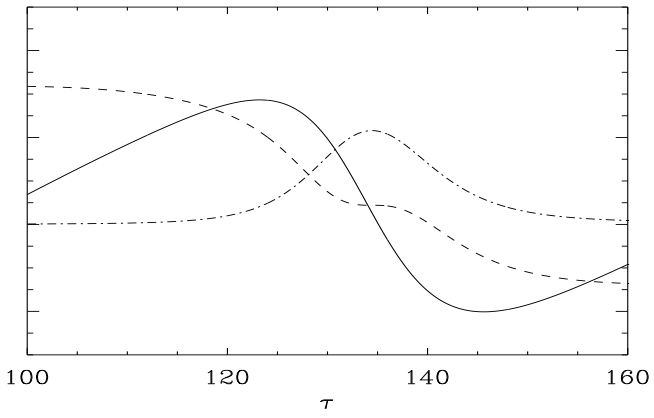

Figure 7.2: Enlargement of Fig. 7.1. z (solid line), y (dot–dashed) line and V (dashed line), (different variables have been rescaled in other to fit the same vertical scale). Same parameters than in Fig. 7.1.

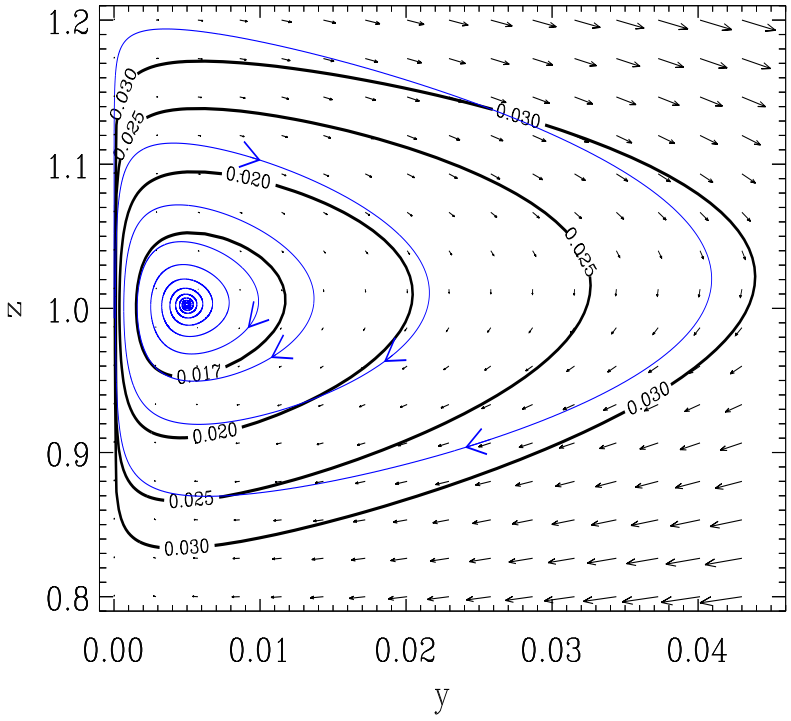

Figure 7.3: Number of carriers versus intensity (scaled variables), blue line. The vector field and contour plot (thick lines) are also represented. Same parameters than in Fig. 7.1. Dimensionless units.

7.2 Potential for class B lasers

We are interested in obtaining a Lyapunov potential that can help us to explain the dynamics observed in the previous section. A similar study was done in Toda potential [Oppo and Politi, 1985] without considering neither the saturation term nor the mean value of the spontaneous emission power, and under those conditions an expression for the period of the transient oscillations was obtained. In our work, we calculate the period of the oscillations by taking into account these two effects. However, the potential is only valid in the deterministic case, since we have not been able to obtain a potential such that the symmetric matrix S, relating the gradient of the potential to the dynamical equations [see Eq. (2.28)] satisfies the fluctuation–dissipation relation (2.35).

The period is obtained in terms of the potential, by assuming that the latter has a constant value during one period. It will be shown that this assumption works reasonably well and gives a good agreement with numerical calculations. Near the steady state, the relaxation oscillations can be also calculated in this form, but the potential is almost constant and consequently is the period.

The evolution equations (7.6, 7.7) can be cast in the form of a non–relaxational potential flow, Eq. (2.26), with the following Lyapunov potential

$$V(y,z) = a_1\, y + a_2\, y^2 + a_3 \ln(y) + \frac{a_4}{y} + \frac{1}{2}\, B^2(y,z), \tag{7.14}$$

where

$$\begin{aligned} a_1 &= \frac{1}{2} - \frac{1}{2}\, a\, \bar{s} + b\, \bar{s} - \frac{1}{4}\, \bar{s}\, d\, (1 + b\, \bar{s}) - \frac{1}{4}\, a\, \bar{s}^2\, c, \\ a_2 &= \frac{\bar{s}}{4}\, (1 + b\, \bar{s}), \qquad (7.15) \\ a_3 &= -\frac{1}{2} \left(a - b + (a\, c + b\, d)\, \bar{s} + \frac{d}{2} \right), \\ a_4 &= \frac{(a\, c + b\, d)}{4}, \\ B(y,z) &= z - 1 - \bar{s}\, y + \frac{(d + c\, z)}{2y}\, (1 + \bar{s}\, y). \qquad (7.16) \end{aligned}$$

The corresponding (nonconstant) matrix D is given by

$$D = \begin{pmatrix} 0 & -D_{12} \\ D_{12} & D_{22} \end{pmatrix}, \tag{7.17}$$

being

$$D_{12} = \frac{4\, y^2}{(1 + \bar{s}\, y)\, [2\, y + c\, (1 + \bar{s}\, y)]}, \tag{7.18}$$

$$D_{22} = \frac{4\, y\, [(1 + 2\, \bar{s} + b\, \bar{s})\, y^2 + b\, y + d + c\, z]}{(1 + \bar{s}\, y)\, [2\, y + c\, (1 + \bar{s}\, y)]^2}. \tag{7.19}$$

According to the general results of section 2.2, it is possible to split the dynamics in purely relaxational part plus a conservative part. The conservative part corresponds to the antisymmetric components of matrix D and, in this case, can be obtained simply by setting $D_{22} = 0$.

The form of the potential appears in Fig. 7.4.

This potential reduces to the one obtained in Ref. [Oppo and Politi, 1985] when setting $c = d = \bar{s} = 0$ (which corresponds to setting the laser parameters $\varepsilon = s = 0$). The potential in this case takes an easier form

$$V(y,z) = \frac{1}{2}[y - (a - b) \ln(y)] + \frac{1}{2}(z - 1)^2, \tag{7.20}$$

with the corresponding matrix

$$D = \begin{pmatrix} 0 & -2y \\ 2y & b + y \end{pmatrix}. \tag{7.21}$$

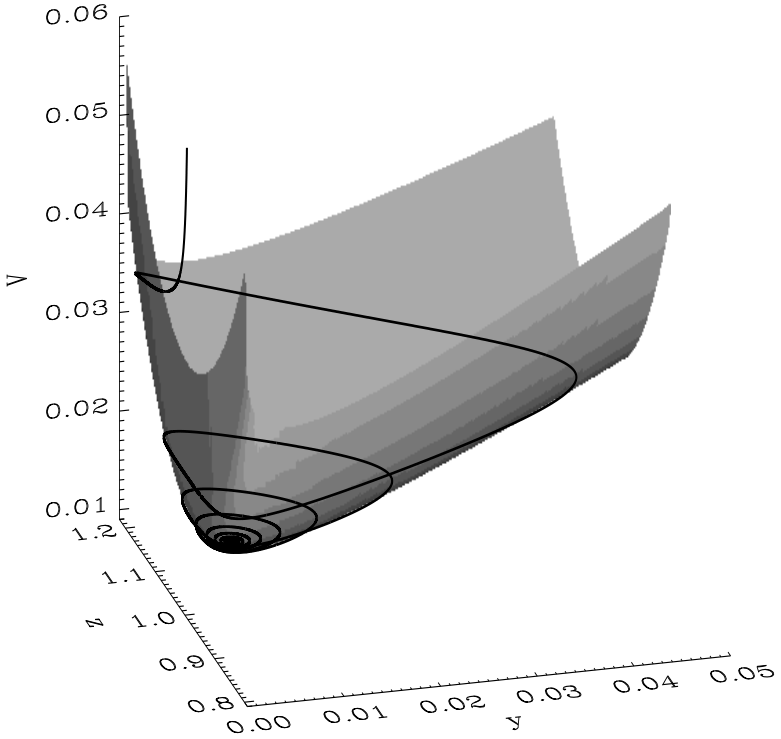

Figure 7.4: Potential for a class B laser. Solid line: simulation of Eqs. (7.6) and (7.7). Same parameters than in Fig. 7.1. Dimensionless units.

As expected, non–vanishing values for the parameters s and ε increase the dissipative part of the potential (D_{22}) associated with the damping term. This is in accordance with the result of Lee and Shin [Lee and Shin, 1989] when linearizing the rate equations around the steady state.

The equipotential lines of (7.14) are also plotted in Fig. 7.3. It is observed that there is only one minimum for V and hence the only stable solution (for this range of parameters) is that the laser switches to the *on* state and relaxes to the minimum of V. The movement towards the minimum of V has two components: a conservative one that produces closed equipotential trajectories and a damping that decreases the value of the potential. The combined effects drives the system to the minimum following a spiral movement, best observed in Figs. 7.3 and 7.4.

In the absence of saturation and noise, $\bar{s} = 0$, $c = 0$, $d = 0$, the maxima and minima of the dynamical variable $y(t)$ occur always at $z = 1$. This is because the equipotential lines of V in the plane (y, z) are symmetric around the line $z = 1$, see Eq. (7.20). However, for other nonzero values of $\bar{s}$, c, d, the potential changes slighty its "orientation" in the plane (y, z) and the maxima of $y(t)$ are not at the previous value of z, but instead satisfy the relationship obtained by cancelling (7.6),

see Fig. 7.3.

Let us consider again the potential (7.14). This potential only depends on the intensity and not on the phase of the electric field. However, the equation for the phase, in the normalized variables,

$$\frac{d\phi}{d\tau} = \left[\frac{z}{(1+\bar{s}\,y)} - 1\right]\alpha, \tag{7.22}$$

can be also deduced from the potential. The full system can be written as

$$\begin{pmatrix} \frac{dy}{d\tau} \\ \frac{d\phi}{d\tau} \\ \frac{dz}{d\tau} \end{pmatrix} = \begin{pmatrix} 0 & 0 & -D_{12} \\ 0 & 0 & -D_{13} \\ D_{12} & D_{13} & D_{22} \end{pmatrix} \begin{pmatrix} \frac{\partial V}{\partial y} \\ \frac{\partial V}{\partial \phi} \\ \frac{\partial V}{\partial z} \end{pmatrix}, \tag{7.23}$$

where

$$D_{13} = -\frac{\left(\frac{d\phi}{d\tau}\right)}{\left(\frac{\partial V}{\partial z}\right)} = -\frac{\left(\frac{z}{(1+\bar{s}y)} - 1\right)}{B(y,z)\left[1 + \frac{c}{2y}(1+\bar{s}y)\right]}\,\alpha, \tag{7.24}$$

and $B(y,z)$ is defined by (7.16). D_{13} it can be introduced as an antisymmetric term in the matrix D because the potential does not depend on ϕ, so the equation for z is not modified. In the case $\bar{s} = c = d = 0$, it is $D_{13} = -\alpha$.

An interesting feature of the phase is that it oscillates until it arrives to a stationary value, see Fig. 7.5. This change in time is due to the extra dependence on the variable z. This behaviour is different from the one of the class A laser in which the phase increases or decreases monotonously, see Fig. 5.1 (b).

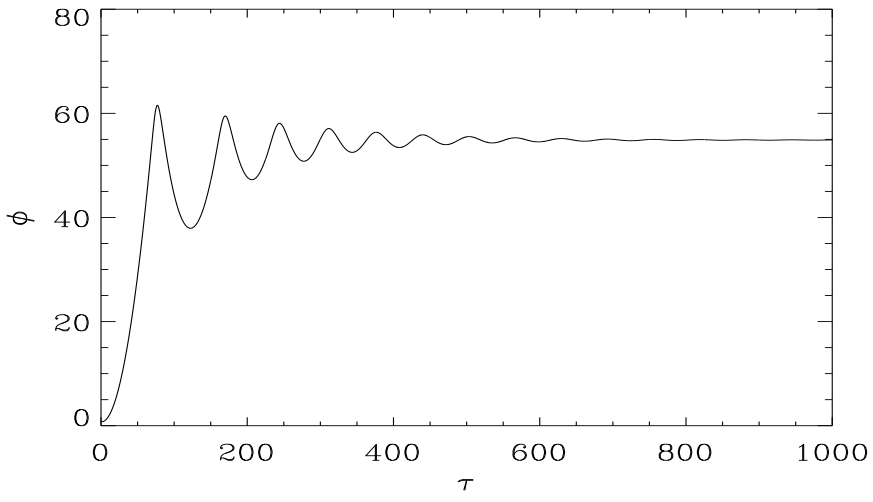

Figure 7.5: Phase of the electric field versus time in a class B laser obtained by numerical solution of Eqs. (7.1 - 7.3). Same parameters than in Fig. 7.1. $\alpha = 5$. Dimensionless units.

7.2.1 Period of the relaxation oscillations

The time evolution of the potential is plotted in Fig. 7.1. In this figure it can be seen that the Lyapunov potential is approximately constant between two consecutive peaks of the relaxation oscillations as it can be also observed with the equipotential lines of Fig. 7.3 (however, in the peak of intensity, the potential decreases steeply, as can be seen in Fig. 7.2). This fact allows us to estimate the relaxation oscillation period by approximating $V(y,z) = E$, constant, during this time interval. When the potential is considered as constant, the period can be evaluated by the standard method of elementary Mechanics: z is replaced by its expression obtained from (7.6) in terms of y and $\dot{y}$ in $V(y,z)$. Using the condition that $V(y,z) = E$, we obtain

$$E = a_1\, y + a_2\, y^2 + a_3\, \ln(y) + a_4 \frac{1}{2} + \frac{1}{2}\left[\frac{\dot{y}}{y}\frac{(1+\bar{s}\, y)}{2}\right]^2 . \tag{7.25}$$

From this equation, we can calculate the relaxation oscillation period T, by using $\dot{y} = \frac{dy}{dt}$ and integrating over a cycle. This leads to the expression

$$T = \int_{y_a}^{y_b} \frac{1+\bar{s}\, y}{y} \frac{dy}{\left[2\left(E - a_1\, y - a_2\, y^2 - a_3\, \ln(y) - a_4\, y^{-1}\right)\right]^{1/2}}, \tag{7.26}$$

where y_a and y_b are the values of y that cancel the denominator. We stress the fact that the only approximation used in the derivation of this expression is that the Lyapunov potential is constant during two maxima of the intensity oscillations. In other words, we have made a mechanical simile and reduced the problem to one with constant energy. A numerical evaluation of this integral yields the dependence of the period, T, with the value of the energy, $E = V$, as plotted in Fig. 7.6.

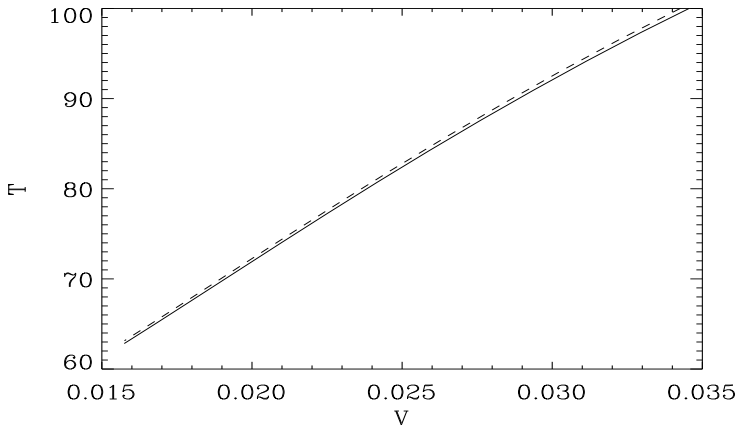

Figure 7.6: Period versus potential for a class B laser obtained with (7.26). Solid line $\bar{s} = 0$, dashed line $\bar{s} = 2$. Other parameters, same than in Fig. 7.1. Dimensionless units.

Equation (7.26) reduces, in the case $c = d = \bar{s} = 0$, to the one previously obtained by using the relation between the laser dynamics and the Toda oscillator derived in [Oppo and Politi, 1985].

According to Fig. 7.6, the period T decreases as the potential V decreases. Since the Lyapunov potential decreases with time, this explains the fact that the period of the oscillations in the transient regime decreases with time. In Fig. 7.7, we compare the results obtained with the expression (7.26) for the period with the ones obtained from numerical simulations of the rate equations (7.6, 7.7). In the simulations we compute the period as the time between two peaks in the evolution of the variable y. As seen in this figure, the above expression for the period, when using the numerical value of the potential V, accurately reproduces the simulation results although it is systematically lower than the numerical result. The discrepancy is less than one percent over the whole range of times.

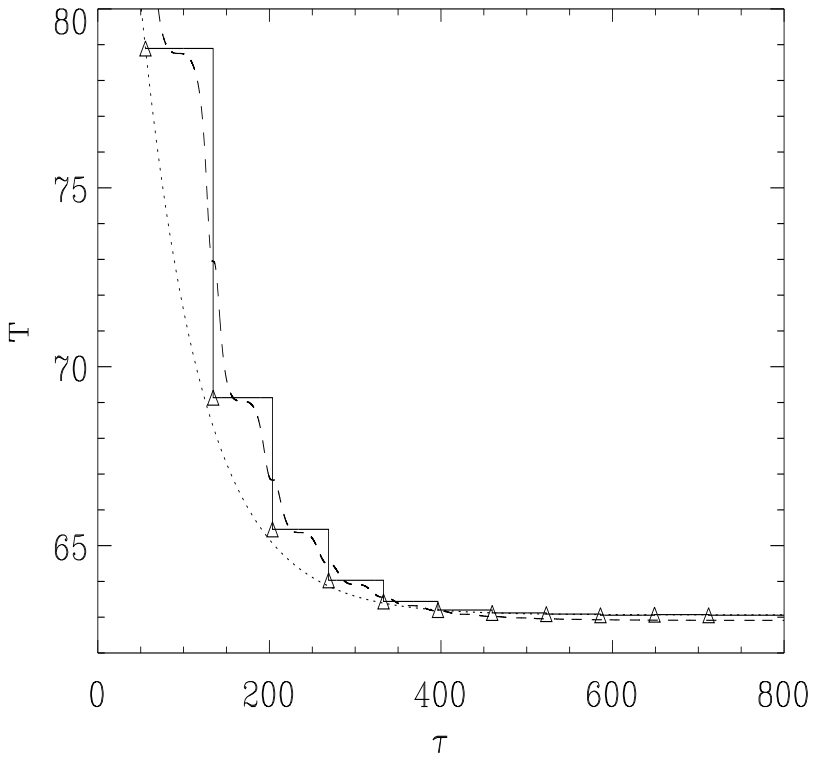

Figure 7.7: Period versus time in a class B laser. Solid line has been calculated as the distance between two peaks of intensity, with triangles plotted at the beginning of each period; dashed line has been calculated using the expression (7.26), with the value of the potential V obtained also from the simulation; dotted line corresponds to the semi-empirical expression (7.40). Same parameters than in Fig. 7.1. We have used $\tau_0 = 55.55$, coinciding with the position of the first intensity peak. Dimensionless units.

It is possible to quantify the difference between the approximate expression (7.26) and the exact values near the stationary state.

By considering (7.26) near the steady state with $y = y_{st} + \delta y$, $E = V_{st} + \delta V$ ($V_{st} = V(y_{st}, z_{st})$) and retaining the lowest terms in δy and δV, one can perform the integral analytically, obtaining an approximation for the period of the steady state

$$T_{st,ap} = \frac{2\,\pi}{D_{12,st}\,\sqrt{K\,F - H^2}}, \tag{7.27}$$

where

$$\begin{aligned} K &= 2\left(a_2 - \frac{1}{2}\,\frac{a_3}{y_{st}^2} + \frac{a_4}{y_{st}^3} + \frac{1}{2}\left[\bar{s} + \frac{(d + c\,z_{st})}{2\,y_{st}^2}\right]^2\right), \\ F &= \left[1 + c\,\frac{(1 + \bar{s}\,y_{st})}{2\,y_{st}}\right]^2, \\ H &= -\left[1 + \frac{c\,(1 + \bar{s}\,y_{st})}{2\,y_{st}}\right]\left[\bar{s} + \frac{(d + c\,z_{st})}{2\,y_{st}^2}\right], \end{aligned} \tag{7.28}$$

and $D_{12,st}$ is the coefficient D_{12} calculated in the steady state.

The result (7.27) could be obtained starting from the linearization of potential (7.25), expanding this expression near the steady state, and then calculate the period from the resulting expression.

The period of the relaxation oscillations near the steady state can also be obtained by the standard procedure of linearizing the evolution equations near the steady state solution. Applying a small perturbation $y = y_{st} + \delta y$ and $z = z_{st} + \delta z$ to Eqs. (7.6) and (7.7), one has after linearization

$$\dot{\delta y} = a_{11}\,\delta y + a_{12}\,\delta z, \tag{7.29}$$

$$\dot{\delta z} = a_{21}\,\delta y + a_{22}\,\delta z, \tag{7.30}$$

where

$$\begin{aligned} a_{11} &= 2\left(\frac{z_{st}}{(1 + \bar{s}\,y_{st})^2} - 1\right), \\ a_{12} &= \left(\frac{2\,y_{st}}{1 + \bar{s}\,y_{st}} + c\right), \\ a_{21} &= -\frac{z_{st}}{(1 + \bar{s}\,y_{st})^2}, \\ a_{22} &= -\left(b + \frac{y_{st}}{1 + \bar{s}\,y_{st}}\right). \end{aligned} \tag{7.31}$$

The eigenvalues of the linearized equations (7.29) and (7.30) are

$$\lambda = -\frac{\varrho}{2} \pm i\,\omega, \tag{7.32}$$

with

$$\varrho = -(a_{11} + a_{22}), \tag{7.33}$$

$$\omega = \frac{1}{2}\sqrt{|(a_{11} - a_{22})^2 + 4\, a_{12}\, a_{21}|}. \tag{7.34}$$

The frequency ω of the relaxation oscillations near the steady state is the imaginary part of the eigenvalues of the linearized equations (7.29) and (7.30). This yields a period $T_{st} = 2\,\pi/\omega$ which can be rewritten in terms of K, F, H, $D_{12,st}$ and $D_{22,st}$ in order to have a better comparison with the approximate period (7.27)

$$T_{st} = \frac{2\,\pi}{D_{12,st}\,\sqrt{K\,F - H^2}}\left[1 - \frac{D_{22,st}^2}{D_{12,st}^2}\frac{F^2}{4\,(K\,F - H^2)}\right]^{-1/2}. \tag{7.35}$$

The difference between (7.27) and (7.35) vanishes with $D_{22,st}$ (i.e. D_{22} in the stationary state). Since $K\,F - H^2$ is always a positive quantity, our approximation will give, at least asymptotically, a smaller value for the period.

In order to have a complete understanding of the variation of the period with time, we need to compute the time variation of the potential $V(\tau)$ between two consecutive intensity peaks. This variation is induced by the dissipative terms in the equations of motion. Although we were not able to derive an expression for the variation of the potential (see [Oppo and Politi, 1985] for an approximate expression in a simpler case), we found that a semi–empirical argument can yield a very simple law which is well reproduced by the simulations. We start by studying the decay to the stationary state in the linearized equations. After expanding around the steady state, the dynamical equations (7.29) and (7.30) show that the variables decay to the steady state as

$$\delta y(\tau), \delta z(\tau) \propto \exp(-\frac{\varrho}{2}\tau), \tag{7.36}$$

where ϱ, (7.33), can be rewritten as

$$\varrho = D_{22,st}\; F. \tag{7.37}$$

In the case of $\bar{s} = 0$, $c = 0$ and $d = 0$ (neither saturation term nor spontaneous emission term are considered) $\varrho = a$.

Expanding $V(y, z)$ around the steady state (y_{st} and z_{st} correspond to extrema of the potential), it is found that

$$V - V_{st} \propto \delta y^2, \delta z^2, \delta y\, \delta z\,. \tag{7.38}$$

Using (7.36) and taking the initial condition at an arbitrary τ_0 we find an expression for the decay of the potential

$$V(\tau) - V_{st} = [V(\tau_0) - V_{st}] \exp\left(-\varrho\,(\tau - \tau_0)\right). \tag{7.39}$$

In Fig. 7.8 we plot $\ln[V(\tau) - V_{st}]$ versus time and compare it with the approximation (7.39). One can see that it fits $\ln[V(\tau) - V_{st}]$ reasonably well not only near the steady state (where it was derived), but also during the transient dynamics. The value of τ_0, being a free parameter, was chosen at the time at which the first peak of the intensity appeared. Although other values of τ_0 might produce a better fit, the one chosen here has the advantage that it can be calculated analytically by following the technique of Ref. [Balle *et al.*, 1991]. It can be derived from Eq. (7.26) that the period T depends linearly on the potential V. This fact, combined with the result of Eq. (7.39), suggests the semi–empirical law for the evolution of the period

$$T(\tau) - T_{st} = [T(\tau_0) - T_{st}] \exp\left(-\varrho\,(\tau - \tau_0)\right). \tag{7.40}$$

This simple expression fits well the calculated period not only near the steady state, but also in the transient regime, see Figs. 7.7 and 7.9. The small differences observed near the steady state are due to the fact that the semi–empirical law, Eq. (7.40), is based on the validity of Eq. (7.26) between the period and the potential. As it was already discussed above, that expansion slightly underestimates the asymptotic (stationary) value of the period. By complementing this study with the procedure given in [Balle *et al.*, 1991] to describe the switch–on process of a laser, and valid until the first intensity peak is reached, we can obtain a complete description of the variation of the oscillations period in the dynamical evolution following the laser switch–on.

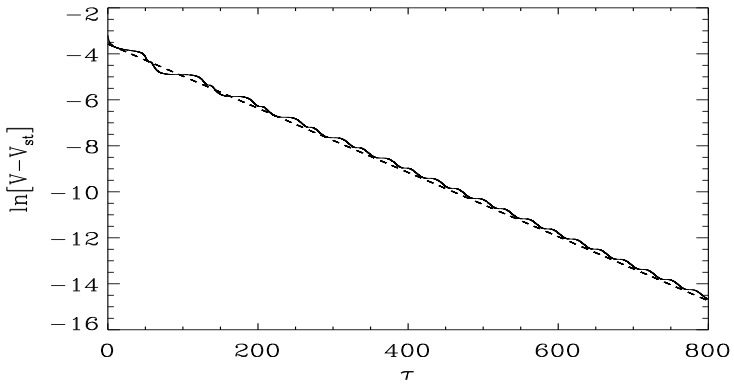

Figure 7.8: Logarithm of the potential difference versus time in a class B laser (solid line), compared with the theoretical expression in the steady state (7.39) (dashed line). Same parameters than in Fig. 7.1 and τ_0 as in Fig. 7.7. Dimensionless units.

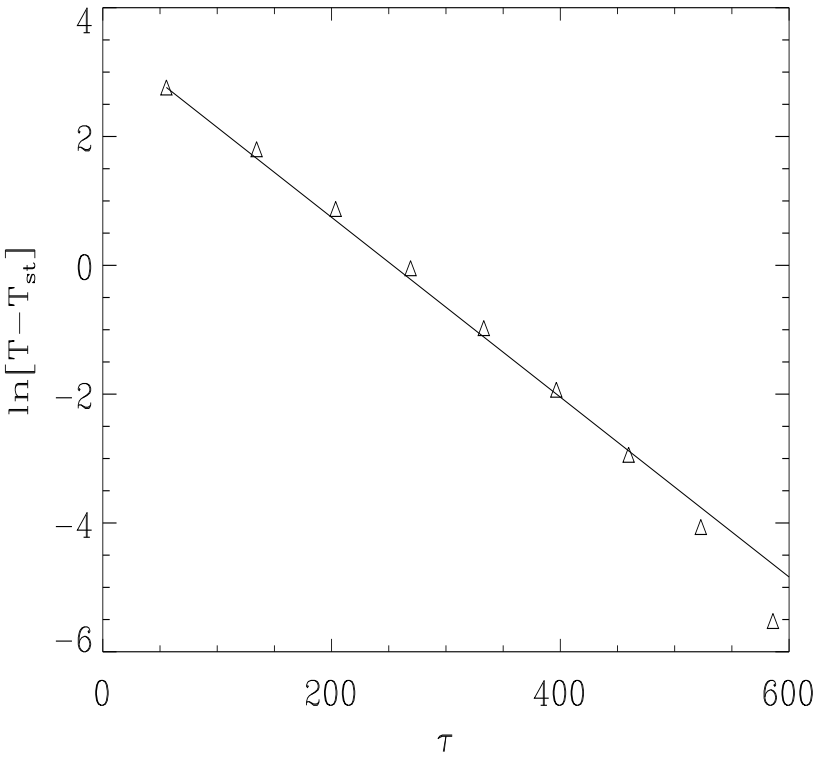

Figure 7.9: Logarithm of the period difference versus time in a class B laser. Triangles correspond to the period calculated from the simulations as the distance between two consecutive intensity peaks, at the same position than in Fig. 7.8. The solid line is the semi–empirical expression Eq. (7.40). Same parameters than in Fig. 7.1 and τ_0 as in Fig. 7.7. Dimensionless units.

Capítol 8

Estructura de resonàncies en un làser de classe B amb senyal injectat

En aquest capítol es descriu la dinàmica qualitativa i el conjunt parcial de bifurcacions (capítol 3) per a un làser de classe B amb senyal injectat amb termes de disintonia petits. El treball d'aquest capítol completa una sèrie d'estudis (veure la secció 1.2) sobre bifurcacions en làsers amb senyal injectat en la proximitat de la singularitat Hopf–sella–node.

Les equacions de balanç (capítol 4) en un sistema de referència que gira a la freqüència del senyal injectat són les (8.1) per al camp elèctric, E, i el nombre de portadors, W. El camp injectat està caracteritzat per l'amplitud β, i la freqüència η. Per al tractament que es fa en aquest capítol s'agafa un valor pel paràmetre de disintonia amb el qual les equacions queden tipus II de la bifurcació Hopf–sella–node.

En les distintes seccions d'aquest capítol es van introduint a poc a poc els distints conjunts invariants del sistema i les seves bifurcacions a causa de la complexitat del conjunt complet de bifurcacions. S'han seleccionat distints colors per a cada tipus de bifurcacions. El conjunt final obtingut és el de la figura 8.22.

La bifurcació sella–node (punts vermells) i la bifurcació de Hopf (punts blaus) dels punts fixos de les equacions, es poden calcular analíticament (8.4 - 8.6). La seva intersecció dóna el punt Hopf–sella–node. Aquestes bifurcacions separen les regions de l'espai de paràmetres (β, η) segons l'estabilitat dels punts fixos A, B i C, Fig. 8.1. A la regió 1, A és estable, B inestable i C sella; un parell d'aquests punts fixos s'aniquilen quan es creua els costats del triangle: cap a la regió 4, B i C col·lapsen; cap a les regions 6, 3 i $3'$, A i B s'aniquilen deixant en aquestes regions el punt C. Un punt fix estable existeix en les regions 1, 4 i 5, que correspon, en termes físics, a tenir una freqüència de sortida sintonitzada amb la d'entrada. El punt fix C correspon a l'estat del làser apagat, i en totes les regions d'interès és un punt sella.

La bifurcació de Hopf (primària) ocorr o bé en el punt fix A ò B, creant una òrbita periòdica transversal, T, al pla $W = 0$. Realitzant un circuit tancat al voltant

del punt Hopf–sella–node: de 1 a 5, el punt B inestable torna sella i es crea l'òrbita T inestable. Aquesta òrbita existeix fins a la regió 3, allà sofreix una bifurcació de Hopf (secundària) quan passa a la regió $3'$, creant un torus transversal inestable, Fig. 8.3. L'òrbita T estable continua existint en la regió 2, i mor en la bifurcació de Hopf (primària) amb el punt fix A. L'òrbita T té un període que divergeix per a valors de β petits (Fig. 8.10), desapareixent a l'òrbita homoclínica a C, Fig. 8.2.

Per completar el conjunt d'invariants en les regions 3 i $3'$, cal incloure una òrbita periòdica longitudinal, L, que és aproximadament coplanar al pla $W = 0$. Aquesta òrbita, estable a 3 però inestable a $3'$, té un període que divergeix a la bifurcació sella–node (bifurcació d'Andronov, Fig. 8.21).

Els punts fixos A i B, juntament amb l'òrbita T corresponen a l'escenari Hopf–sella–node tipus *II*. L'òrbita L és una part integral del conjunt de bifurcacions, i la interacció de les bifurcacions que sofreixen aquestes dues òrbites organitza l'estructura de resonàncies. La bifurcació de Hopf secundària s'interrompeix en una illa de bifurcacions de període doble d'òrbites periòdiques (cercle blau figura 8.2) i acaba en una bifurcació sella–node d'òrbites periòdiques (triangle rosa).

El moviment quasi–periòdic pot sofrir fenòmens de resonància i generar òrbites periòdiques. Aquestes òrbites poden ésser classificades per un nombre p de voltes seguint l'òrbita primària, T, i q que denota el nombre de voltes fetes al voltant l'òrbita primària abans de tancar–se. A la figura 8.7, es veu l'estructura de resonàncies per distints valors de q. Les línies en color rosa corresponen a bifurcacions sella–node d'òrbites periòdiques. Per a $q > 4$ es comporten com l'estructura estàndard de llengües d'Arnold i es van acumulant cap el punt Hopf–sella–node.

L'estructura de les òrbites periòdiques dins cada resonància és bastant similar. Com exemple s'estudia la resonància 3, Fig. 8.9. A la figura 8.10 (a), es veu que per a β a prop de la bifurcació de Hopf secundària de T, una òrbita periòdica inestable i una sella neixen i tornen a col·lapsar en un valor de β més gran a la bifurcació sella–node revers. Per a un valor de η més baix, Fig. 8.10 (b), la branca inestable té un període que divergeix i s'originen dues bifurcacions homoclíniques (cercle verd de la figura 8.9). El tall de la figura 8.10 (c) indica que l'òrbita periòdica resonant es junta amb l'òrbita L. Aquest procés d'unió de les resonàncies transversal en la solució de l'òrbita periòdica s'observa a totes les resonàncies. A prop del procés d'unió s'observa que l'òrbita L també bifurca en una Hopf secundària (línies negres per valors de β grans), que té així mateix té resonàncies 1/2 (cercles color blau corresponents a bifurcacions de període doble).

Les resonàncies fortes ($q \leq 4$) tenen una estructura més complicada que la indicada. En particular, les bifurcacions sella–node de les llengües no ocorr en el torus. El torus pot créixer quan els paràmetres canvien i col·lisionar amb una òrbita resonant. Això corresponen a una bifurcació homoclínica a una òrbita periòdica amb la destrucció final del torus (diamands negres). Els punts d'intersecció d'aquestes homoclíniques, les Hopf secundàries i les resonàncies corresponen a singularitat tipus Takens–Bogdanov, Fig. 8.15.

Entre les resonàncies transversals indicades, s'han obtingut altres resonàncies, Fig. 8.18, encara que una classificació de les mateixes és prou complicada.

Chapter 8

Resonance structure in a class B laser with injected signal

In this chapter, we describe the qualitative dynamics and bifurcation set for a laser with injected signal for small cavity detunings by using the definitions included in chapter 3.

The work presented in this chapter completes the above series of studies of bifurcations of a laser with injected signal in the neighbourhood of the Hopf–saddle–node (HSN) singularity, as it was reviewed in section 1.2. We numerically analyse the weak cavity detuning regime for a fixed value of the detuning parameter $\theta = 0.5$ (in adequate units), where type *II* Hopf–saddle–node is expected. The small–detuning case is particularly relevant for applications, since a natural ambition when constructing laser cavities is to obtain low detunings. Long–time behaviour depending on the amplitude and the frequency shift of the applied signal is studied. The main bifurcation structure consists of a (secondary) Hopf bifurcation on the periodic orbit associated to the Hopf–saddle–node bifurcation. We have analysed in detail the resonance structure which reveals a rich interaction with other bifurcations *not* present in the usual Hopf–saddle–node scenario.

In the next section we review the representative equations for a laser with injected signal, together with the unfolding of the Hopf–saddle–node bifurcation. In Sec. 8.2, the resonance structure is described, while Sec. 8.3 discusses the Andronov global bifurcation occurring in this laser, and its interaction with other bifurcations. Finally, a global outlook and discussion is given in Sec. 8.4.

8.1 Equations for the laser with injected signal

The model for a laser system is given in terms of the Maxwell–Bloch equations, chapter 4. In a great variety of lasers, the decay times associated with the population inversion and the electric field have different time scales, allowing for the adiabatic elimination of the fast decaying polarization variable (class B) [Solari and Oppo, 1994]. The dimensionless rate equations in a reference frame that rotates with the

injected signal may be written as

$$\begin{aligned} \frac{dE}{dt} &= EW + i(\theta W + \eta)E + \beta, \\ \frac{dW}{dt} &= A^2 - \chi W(1 + g|E|^2) - |E|^2, \end{aligned} \tag{8.1}$$

where E is the complex envelope of the electric field and W is proportional to the population inversion. θ represents the detuning between the atomic and the nearest eigenfrequency of the cavity, A is proportional to the amount of pumped atoms, $\chi \geq 0$ is proportional to the inverse of the decay time of the population inversion and g is inversely proportional to $1+\theta^2$. For typical lasers, χ is small. η is the detuning of the perturbation frequency and the unperturbed laser operating frequency and $\beta \geq 0$ is the intensity of the injected signal. The relationship between the parameters used in this model and the parameters in the Maxwell–Bloch equations can be found in [Solari and Oppo, 1994]. The model can be justified for small signal intensity ratio, $\beta/A^2 \ll 1$, although it has been argued that it can be successfully applied beyond this limit [Oppo *et al.*, 1986]. Our present study centers in this limit and in some cases we have explored a region beyond this limit in order to understand the fate of some invariant sets. The set of equations (8.1) can be obtained from Eqs. (4.11) and (4.12), in the absence of noise terms and without injected signal, by performing the suitable change of variables.

Solari and Oppo [1994] performed a reduction of the three–equations model by averaging over the fast relaxation oscillation motion, reducing the dynamics to a two–equations system. In this way, the difficulty of finding analytic expressions for most of the local bifurcations is simplified. A close analysis of the singularities of this model, reveals that the system organizes around the codimension–2 Hopf–saddle–node local bifurcation. One finds that after a suitable change of coordinates one may arrive to its normal form representation (3.1) [Guckenheimer and Holmes, 1983]

$$\begin{aligned} r' &= (\mu + \bar{a}\, v)\, r + \mathcal{O}(3), \\ v' &= \nu + \bar{b}\, r^2 - v^2 + \mathcal{O}(3), \\ \zeta' &= \bar{c} + \bar{a}\, v + \mathcal{O}(2), \end{aligned} \tag{8.2}$$

where $\bar{a}$, $\bar{b}$, $\bar{c} \neq 0$ and μ and ν are the bifurcation parameters, all function of the laser parameters. The signs of $\bar{a}$ and $\bar{b}$ classify different types of flows: type I for ($\bar{a} > 0$, $\bar{b} > 0$), type II for ($\bar{a} < 0$, $\bar{b} > 0$), type III for ($\bar{a} > 0$, $\bar{b} < 0$), type IV for ($\bar{a} < 0$, $\bar{b} < 0$).

One of the main achievements of the Solari and Oppo average model is that they have established that the actual laser with injected signal operation is controlled by the cavity detuning parameter θ in the following way:

type II: $0 < \theta < 1$,
type I: $1 < \theta < \sqrt{3}$,
type III: $\sqrt{3} < \theta$.

We refer the reader to [Zimmermann *et al.*, 2001] for a detailed account of the normal form computations for the three–dimensional laser with injected signal equations (8.1), where the above results are validated up to order $O(\chi^2)$, for

$$\begin{aligned}
\bar{a}(\theta) &= (1+gA^2)\frac{(\theta^2-1)}{4\theta}\chi + O(\chi^2), \\
\bar{b}(\theta) &= -(1+gA^2)\frac{(1+\theta^2)(\theta^2-3)}{8\theta}\chi + O(\chi^2), \\
\bar{c} &= \sqrt{2}A + O(\chi^2), \\
\mu(\beta,\eta) &= \theta\left(\frac{2}{1+\theta^2} - \frac{\chi}{\beta\theta\sqrt{1+\theta^2}}\right), \\
\nu(\beta,\eta) &= 2\left(\frac{\beta\sqrt{1+\theta^2}+\eta}{\beta(1+\theta^2)}\right).
\end{aligned} \tag{8.3}$$

The main characteristics of each type of flow may be summarized as follows. A saddle–node bifurcation occurs for $\nu = \nu_{\rm sn} = 0$, where a pair of saddle–focus fixed points are born at $(r, v) = (\pm\sqrt{\nu}, 0)$. These fixed points may as well bifurcate in a Hopf bifurcation along a parabola in parameter space, $\nu = \nu_{\rm Hopf} = \mu^2/\bar{a}^2$. The periodic orbit will be at $v_{\rm Hopf} = -\mu/\bar{a}$ and its radius is given by $r^2_{\rm Hopf} = (\mu^2/\bar{a}^2 - \nu)/\bar{b}$. The main differences between type *I-III*, lie in the region of existence and stability of the periodic orbit. In type *III* the periodic orbit always co–exists with the fixed points ($\nu > \mu^2/\bar{a}^2 > 0$), while in type *I* the periodic orbit exists before the creation of the fixed points (for $\nu < 0$, $r_{\rm Hopf} > 0$). Type *II* is similar to type *I*, but the stability of the periodic orbit may change. A degenerate (secondary) Hopf bifurcation occurs on the semiaxis $\mu = 0, \nu < 0$, where the periodic orbit becomes a center. Addition of appropriate third order terms to the normal form (8.2) breaks, in general, this degeneracy resulting in a bifurcation to a torus. The fate of the torus will depend on the perturbation applied to (8.2) and results concerning this type are unknown. Kirk [Kirk, 1991] has analysed these kind of perturbations for type *III*, where the secondary Hopf bifurcation occurs in the semiaxis $\mu = 0, \nu > 0$, coexisting with the fixed points. In her analysis she found that the torus breaks–up in Arnold tongues [Arnold, 1983], which in turn ends up as *resonances of another secondary Hopf bifurcation*. Below a similar scenario will be found.

In this work we investigate the small detuning regime $0 < \theta < 1$ corresponding to type *II*, a case not studied in complete detail in previous works. In terms of bifurcations and periodic orbit organization, the most prominent feature is the (secondary) Hopf bifurcation of periodic orbits associated to the Hopf–saddle–node singularity. This will be one of our main objects of study, where we will discuss the interaction of its resonances with other bifurcations not present in the (local) normal form analysis.

8.2 Bifurcation set for small detuning

We have integrated numerically equations (8.1) with fixed parameters $A = 1$, $\chi = 0.3$ and $g = 0$[1]. Most computations were done with the AUTO97 [Doedel *et al.*, 1997] continuation package, in the parameters (β, η) and $0 < \theta = 0.5 < 1$. In general, the locus in parameter space of a particular bifurcation will be presented as points, representing the actual computation performed. To guide the reader we have selected different colours for each type of bifurcation.

Given the complexity of the full bifurcation set found, we will introduce in steps the different invariant sets and their bifurcations. Readers not interested in the technical details of the calculation may refer to Fig. 8.22 for the full bifurcation set discussed in this chapter.

8.2.1 Invariant sets close to the Hopf–saddle–node bifurcation

We begin our numeric exploration with the locus of the saddle–node, Hopf and Hopf–saddle–node bifurcations of fixed points. These may be explicitly computed, with the relevant equations being:

1. The fixed point equation may be reduced to,

$$\begin{aligned}(1+\theta^2)Y^3 &- 2[A^2(1+\theta^2)+\chi\eta\theta]Y^2 \\ &+ [A^4(1+\theta^2)+2A^2\chi\eta\theta+\chi^2\eta^2]Y-\chi^2\beta^2=0,\end{aligned} \tag{8.4}$$

   a cubic polynomial in $Y = |E|^2$.

2. The saddle–node condition, i.e., when one of the eigenvalues of the Jacobian is zero,

$$3(1+\theta^2)Y^2-4[A^2(1+\theta^2)+\chi\eta\theta]Y+A^4(1+\theta^2)+2A^2\chi\eta\theta+\chi^2\eta^2=0. \tag{8.5}$$

3. The Hopf condition (i.e., when two (complex conjugated) eigenvalues of the Jacobian are pure imaginary) reads

$$\begin{aligned}&(1+\theta^2)Y^3-[3A^2(1+\theta^2)+\chi^2(\theta^2-3)+2\eta\chi\theta]Y^2 \\ +\;&[3A^4(1+\theta^2)+A^2[(\theta^2-5)\chi^2+4\eta\chi\theta]+2\chi^4+\theta\chi^3\eta+\eta^2\chi^2]\,Y \\ -\;&[(1+\theta^2)A^6+2A^4(\eta\chi\theta-\chi^2)+A^2(\eta^2\chi^2+\chi^4)]=0.\end{aligned} \tag{8.6}$$

The fixed point equation reveals that there are regions of one or three fixed points, separated by saddle–node bifurcations. The simultaneous solution of (8.4) and (8.5) (the fixed point equation will then have a double root) gives the locus of

[1] In real lasers $g \in [0, 1]$. However, the qualitative features of the bifurcations around the Hopf–saddle–node bifurcation will not change if g is kept small. In [Zimmermann *et al.*, 2001] it is found to slightly modify the second–order coefficients in the Hopf–saddle–node normal form.

the saddle–node curve, while solution of (8.4) with (8.6) gives the locus of the Hopf curve. When all three equations are simultaneously satisfied there is a tangency point where the Hopf–saddle–node occurs [Zimmermann *et al.*, 2001],

$$\begin{aligned} \eta_{\rm hsn}(\theta) &= -\frac{(1+\theta^2)}{2\theta}\left(1-\frac{1}{4\,\theta^2 A^2}\,\chi^2\right)\,\chi+\mathcal{O}(\chi)^4, \\ \beta_{\rm hsn}(\theta) &= \frac{A\,\sqrt{1+\theta^2}}{2\theta}\left(1-\frac{(1+\theta^2)}{4\,\theta^2 A^2}\,\chi^2\right)\,\chi+\mathcal{O}(\chi)^4. \end{aligned} \tag{8.7}$$

A typical bifurcation set displaying these bifurcations is shown in Fig. 8.1. Inside the "triangle" shaped region, three fixed points exist, while outside this region only one fixed point remains. Let us label the fixed points in region 1 as: A stable, B unstable and C saddle. A pair of the above fixed points are annihilated crossing the sides of the triangle: moving into region 4, B and C collide, while entering region 6 or (3, 3′), A and B annihilates leaving in these regions only the fixed point C.[2] In physical terms, *locking* behaviour (output frequency tuned to that of the injected signal) occurs whenever the laser is operated in any of the regions (1, 4, 5), where a stable fixed point exists. On the other hand, fixed point C exists in all regions except 4 in Fig. 8.1 and is approximately situated in $(|E|, W) \approx (0, A^2/\chi)$ for $\beta \ll 1$, which corresponds to the laser–off state. In all regions of interest it is a saddle fixed point.

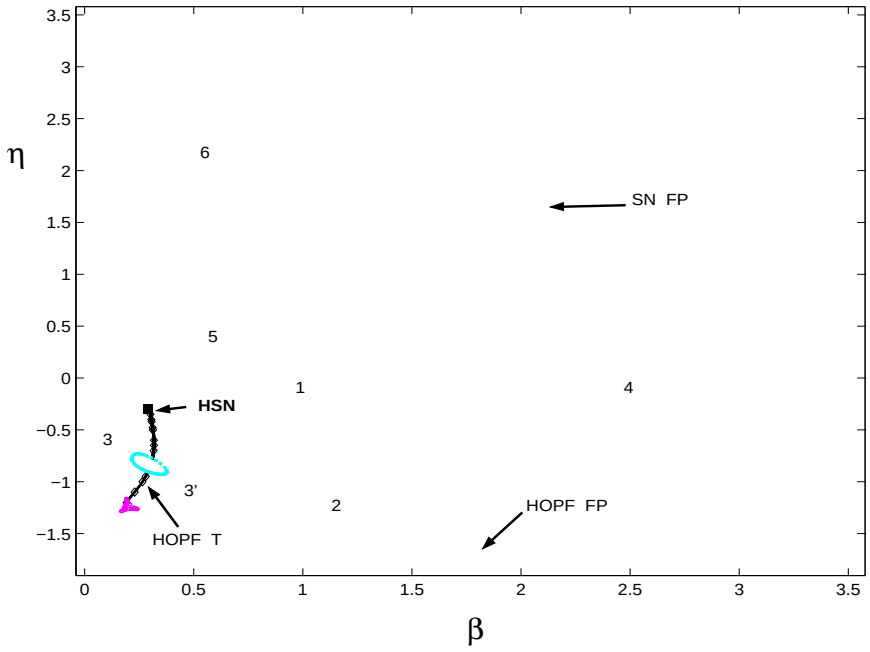

Figure 8.1: Numerical bifurcation set in parameters (β, η) for type *II*. Red line: saddle–node of fixed points (SN FP). Blue line: Hopf bifurcation of fixed points (HOPF FP). The secondary Hopf bifurcation of transversal periodic orbits (HOPF T) separates region 3 and 3'.

[2]Notice that choosing a path far out from the "triangle" shaped region, we have to identify fixed point C in regions (6, 3, 3′) with fixed point A in region 4.

The (primary) Hopf bifurcation occurs on either fixed point A or B, creating a periodic orbit *transversal* to the $W = 0$ plane, which will be referred to as T in what follows. This orbit corresponds to the undamped relaxation oscillation [van Tartwijk and Lenstra, 1995], whose main characteristic is that the phase of the electric field remains bounded. A close inspection in parameter space around the Hopf–saddle–node point reveals that moving from region 1 to region 5, the unstable node B becomes a saddle and creates an unstable T orbit. This orbit exists up to region 3, where it suffers a (secondary) Hopf bifurcation when crossing to region $3'$, creating an unstable transversal torus. The remaining stable T periodic orbit continues to exist up to region 2, when it dies in a (primary) Hopf bifurcation with fixed point A.

To complete the main invariant sets present in region 3 and $3'$, we have to include another periodic orbit. For sufficiently small β we find from (8.1) that for $W \approx 0$, $|E| \approx A$ and the phase $\arg(E(t)) = \eta\ t$, which corresponds to the *cw* (continuous-wave) laser solution [van Tartwijk and Lenstra, 1995] with an unbounded electric field phase. As this orbit lies approximately coplanar to the $W = 0$ plane, it will be referred to as L, the *longitudinal* orbit. For sufficiently small (η, β), this orbit can be easily shown to be stable. However we find that the period of L diverges at the saddle–node bifurcation of fixed point, where the orbit disappears. This global bifurcation is known as Andronov or saddle–node infinite–period bifurcation [Kuznetsov, 1997], and will be addressed in more detail in Sec. 8.3. We remark that the stability of L close to the Andronov bifurcation depends on the stability of the saddle–node fixed point, thus on which side of the Hopf–saddle–node point one is located: in region $3'$ the orbit is unstable, while in region 3 it is stable. From this, it is clear that at least a local bifurcation to L is required. Below we will show that a new secondary Hopf bifurcation on L occurs inside region $3'$.

In summary, we find that fixed points A and B together with the transversal periodic orbit T correspond to the type *II* Hopf–saddle–node scenario proposed by the normal form analysis in the previous section. The periodic orbit L is also an integral part of the bifurcation set of a laser with injected signal, and we will show in the next section how the interaction of bifurcations between these two periodic orbits organize the resonance structure.

8.2.2 Bifurcations of transversal periodic orbits

We begin with a general observation for the existence boundary of transversal T orbit born at the the Hopf bifurcation of fixed points. For a fixed value of η, we find for the continuation of this orbit for decreasing β, its period diverges at a critical $\beta \approx 0.05$, for an interval of η close to 0, where a homoclinic orbit to fixed point C occurs. Figure 8.2 shows the locus of this global bifurcation in parameter space, while Figs. 8.10 and 8.11 show the typical period versus β behaviour. This bifurcation is found not to depend on θ, and was found up to type *III* regime. We leave for Sec. 8.3 the discussion of how this bifurcation is related to the Andronov bifurcation producing L.

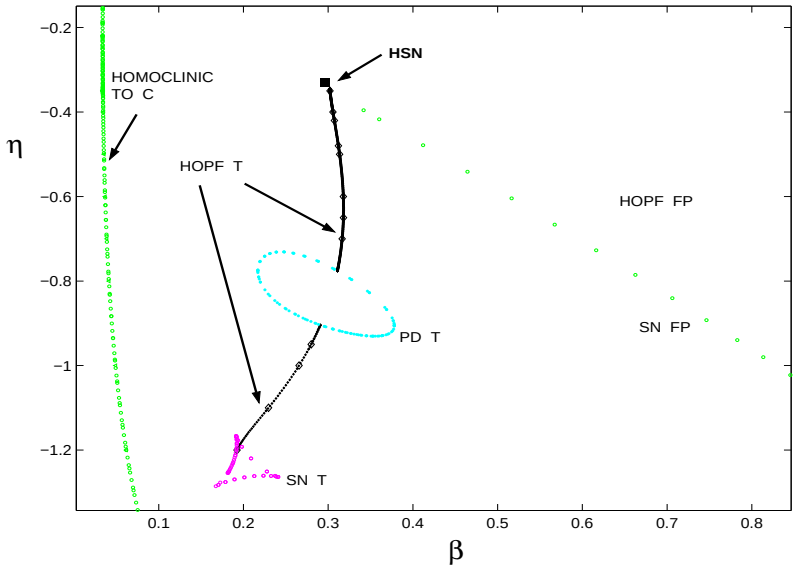

Figure 8.2: Partial numerical bifurcation set showing the homoclinic to C fixed point and the first resonances of the transversal secondary Hopf bifurcation. Saddle–node bifurcation of transversal periodic orbits (SN T) and period doubling bifurcation of transversal periodic orbits (PD T) are indicated.

In Fig. 8.3 (a) we display the main invariant sets for the parameter region bounded by the homoclinic to C and the secondary Hopf bifurcation. We have the stable longitudinal orbit L (which lies approximately on $|E| \approx A = 1, W \approx 0$), together with the unstable transversal orbit T. This orbit has a large variation in the population inversion W, and a bounded electric field phase (the phase does not make a complete turn as L does). Crossing the secondary Hopf bifurcation T and entering region $3'$, we find that T becomes stable and an unstable invariant torus is created. Figure 8.3 (b) shows the invariant sets, where only the intersections of the quasiperiodic orbit with the $W = 0$ plane are shown. A time series of the intensity $|E|^2$ on this solution is shown in Fig. 8.4.

It is well known that in generic systems quasiperiodic motion may suffer resonance phenomena. Local analysis [Arnold, 1983] around the Hopf bifurcation reveals that whenever the ratio of the two competing frequencies is rational, the quasiperiodic motion may disappear and periodic orbits arise. These orbits may be classified by an integer number of p turns following the primary or bifurcating orbit (T in this case), and another integer number q which denotes the number of turns made around the primary orbit, before closing on itself. Precisely on the (secondary) Hopf bifurcation the nontrivial Floquet multipliers are on the unit circle at $e^{\pm i2\pi p/q}$. A general result shows that in the *weak resonances* case $q > 4$ these periodic orbits are born in saddle–node pairs, and in a two–parameter space they trace a 'tongue' (known as Arnold tongue) with the tip lying on the (secondary) Hopf bifurcation. In phase space the periodic orbits are *phase locked* solution on the torus. On the other hand the case $q \leq 4$ are known as *strong resonances* and do not correspond to 'strict' Arnold tongues. The details of each strong resonance in a general study may be found in [Kuznetsov, 1997].

7.2.1 Period of the relaxation oscillations

The time evolution of the potential is plotted in Fig. 7.1. In this figure it can be seen that the Lyapunov potential is approximately constant between two consecutive peaks of the relaxation oscillations as it can be also observed with the equipotential lines of Fig. 7.3 (however, in the peak of intensity, the potential decreases steeply, as can be seen in Fig. 7.2). This fact allows us to estimate the relaxation oscillation period by approximating $V(y,z) = E$, constant, during this time interval. When the potential is considered as constant, the period can be evaluated by the standard method of elementary Mechanics: z is replaced by its expression obtained from (7.6) in terms of y and $\dot{y}$ in $V(y,z)$. Using the condition that $V(y,z) = E$, we obtain

$$E = a_1\, y + a_2\, y^2 + a_3\, \ln(y) + a_4 \frac{1}{2} + \frac{1}{2}\left[\frac{\dot{y}}{y}\frac{(1+\bar{s}\, y)}{2}\right]^2 . \tag{7.25}$$

From this equation, we can calculate the relaxation oscillation period T, by using $\dot{y} = \frac{dy}{dt}$ and integrating over a cycle. This leads to the expression

$$T = \int_{y_a}^{y_b} \frac{1+\bar{s}\, y}{y} \frac{dy}{\left[2\left(E - a_1\, y - a_2\, y^2 - a_3\, \ln(y) - a_4\, y^{-1}\right)\right]^{1/2}}, \tag{7.26}$$

where y_a and y_b are the values of y that cancel the denominator. We stress the fact that the only approximation used in the derivation of this expression is that the Lyapunov potential is constant during two maxima of the intensity oscillations. In other words, we have made a mechanical simile and reduced the problem to one with constant energy. A numerical evaluation of this integral yields the dependence of the period, T, with the value of the energy, $E = V$, as plotted in Fig. 7.6.

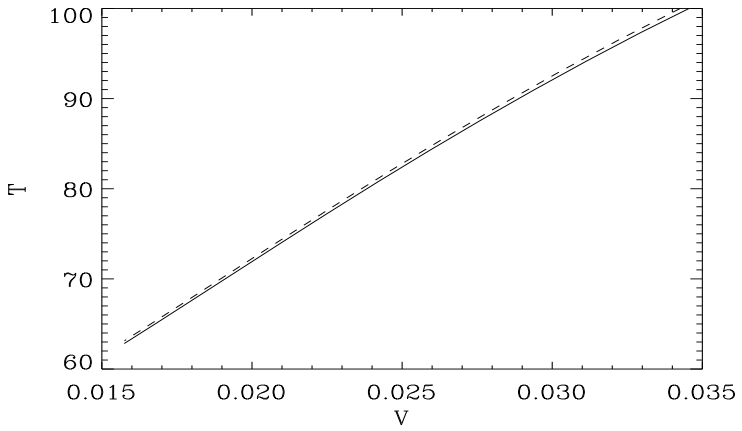

Figure 7.6: Period versus potential for a class B laser obtained with (7.26). Solid line $\bar{s} = 0$, dashed line $\bar{s} = 2$. Other parameters, same than in Fig. 7.1. Dimensionless units.

Equation (7.26) reduces, in the case $c = d = \bar{s} = 0$, to the one previously obtained by using the relation between the laser dynamics and the Toda oscillator derived in [Oppo and Politi, 1985].

According to Fig. 7.6, the period T decreases as the potential V decreases. Since the Lyapunov potential decreases with time, this explains the fact that the period of the oscillations in the transient regime decreases with time. In Fig. 7.7, we compare the results obtained with the expression (7.26) for the period with the ones obtained from numerical simulations of the rate equations (7.6, 7.7). In the simulations we compute the period as the time between two peaks in the evolution of the variable y. As seen in this figure, the above expression for the period, when using the numerical value of the potential V, accurately reproduces the simulation results although it is systematically lower than the numerical result. The discrepancy is less than one percent over the whole range of times.

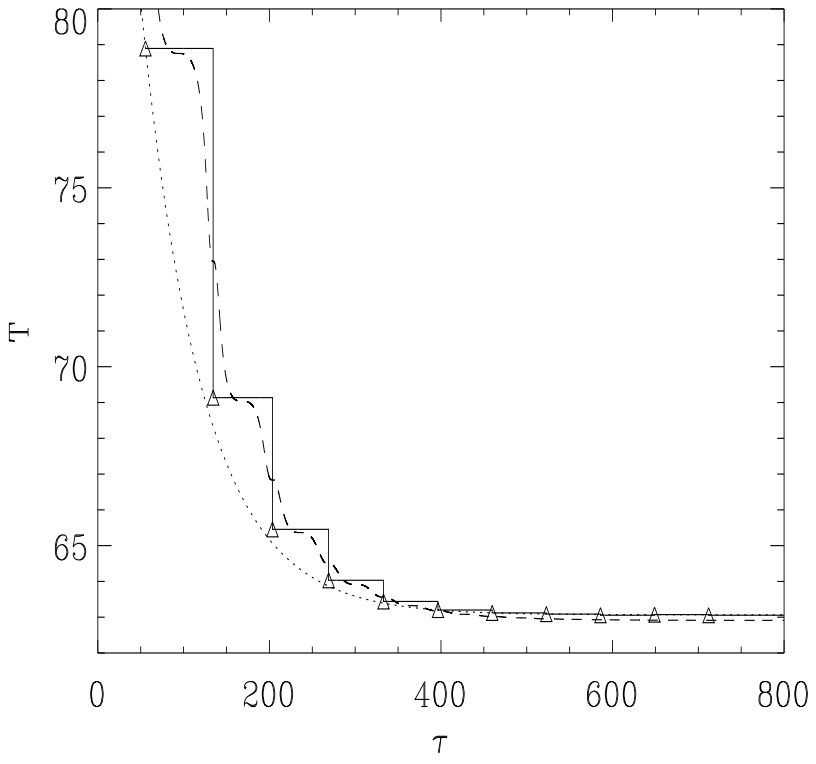

Figure 7.7: Period versus time in a class B laser. Solid line has been calculated as the distance between two peaks of intensity, with triangles plotted at the beginning of each period; dashed line has been calculated using the expression (7.26), with the value of the potential V obtained also from the simulation; dotted line corresponds to the semi-empirical expression (7.40). Same parameters than in Fig. 7.1. We have used $\tau_0 = 55.55$, coinciding with the position of the first intensity peak. Dimensionless units.

It is possible to quantify the difference between the approximate expression (7.26) and the exact values near the stationary state.

By considering (7.26) near the steady state with $y = y_{st} + \delta y$, $E = V_{st} + \delta V$ ($V_{st} = V(y_{st}, z_{st})$) and retaining the lowest terms in δy and δV, one can perform the integral analytically, obtaining an approximation for the period of the steady state

$$T_{st,ap} = \frac{2\,\pi}{D_{12,st}\,\sqrt{K\,F - H^2}}, \tag{7.27}$$

where

$$\begin{aligned} K &= 2\left(a_2 - \frac{1}{2}\,\frac{a_3}{y_{st}^2} + \frac{a_4}{y_{st}^3} + \frac{1}{2}\left[\bar{s} + \frac{(d + c\,z_{st})}{2\,y_{st}^2}\right]^2\right), \\ F &= \left[1 + c\,\frac{(1 + \bar{s}\,y_{st})}{2\,y_{st}}\right]^2, \\ H &= -\left[1 + \frac{c\,(1 + \bar{s}\,y_{st})}{2\,y_{st}}\right]\left[\bar{s} + \frac{(d + c\,z_{st})}{2\,y_{st}^2}\right], \end{aligned} \tag{7.28}$$

and $D_{12,st}$ is the coefficient D_{12} calculated in the steady state.

The result (7.27) could be obtained starting from the linearization of potential (7.25), expanding this expression near the steady state, and then calculate the period from the resulting expression.

The period of the relaxation oscillations near the steady state can also be obtained by the standard procedure of linearizing the evolution equations near the steady state solution. Applying a small perturbation $y = y_{st} + \delta y$ and $z = z_{st} + \delta z$ to Eqs. (7.6) and (7.7), one has after linearization

$$\dot{\delta y} = a_{11}\,\delta y + a_{12}\,\delta z, \tag{7.29}$$

$$\dot{\delta z} = a_{21}\,\delta y + a_{22}\,\delta z, \tag{7.30}$$

where

$$\begin{aligned} a_{11} &= 2\left(\frac{z_{st}}{(1 + \bar{s}\,y_{st})^2} - 1\right), \\ a_{12} &= \left(\frac{2\,y_{st}}{1 + \bar{s}\,y_{st}} + c\right), \\ a_{21} &= -\frac{z_{st}}{(1 + \bar{s}\,y_{st})^2}, \\ a_{22} &= -\left(b + \frac{y_{st}}{1 + \bar{s}\,y_{st}}\right). \end{aligned} \tag{7.31}$$

The eigenvalues of the linearized equations (7.29) and (7.30) are

$$\lambda = -\frac{\varrho}{2} \pm i\,\omega, \tag{7.32}$$

with

$$\varrho = -(a_{11} + a_{22}), \tag{7.33}$$

$$\omega = \frac{1}{2}\sqrt{|(a_{11} - a_{22})^2 + 4\, a_{12}\, a_{21}|}. \tag{7.34}$$

The frequency ω of the relaxation oscillations near the steady state is the imaginary part of the eigenvalues of the linearized equations (7.29) and (7.30). This yields a period $T_{st} = 2\,\pi/\omega$ which can be rewritten in terms of K, F, H, $D_{12,st}$ and $D_{22,st}$ in order to have a better comparison with the approximate period (7.27)

$$T_{st} = \frac{2\,\pi}{D_{12,st}\,\sqrt{K\,F - H^2}}\left[1 - \frac{D_{22,st}^2}{D_{12,st}^2}\frac{F^2}{4\,(K\,F - H^2)}\right]^{-1/2}. \tag{7.35}$$

The difference between (7.27) and (7.35) vanishes with $D_{22,st}$ (i.e. D_{22} in the stationary state). Since $K\,F - H^2$ is always a positive quantity, our approximation will give, at least asymptotically, a smaller value for the period.

In order to have a complete understanding of the variation of the period with time, we need to compute the time variation of the potential $V(\tau)$ between two consecutive intensity peaks. This variation is induced by the dissipative terms in the equations of motion. Although we were not able to derive an expression for the variation of the potential (see [Oppo and Politi, 1985] for an approximate expression in a simpler case), we found that a semi–empirical argument can yield a very simple law which is well reproduced by the simulations. We start by studying the decay to the stationary state in the linearized equations. After expanding around the steady state, the dynamical equations (7.29) and (7.30) show that the variables decay to the steady state as

$$\delta y(\tau), \delta z(\tau) \propto \exp(-\frac{\varrho}{2}\tau), \tag{7.36}$$

where ϱ, (7.33), can be rewritten as

$$\varrho = D_{22,st}\; F. \tag{7.37}$$

In the case of $\bar{s} = 0$, $c = 0$ and $d = 0$ (neither saturation term nor spontaneous emission term are considered) $\varrho = a$.

Expanding $V(y, z)$ around the steady state (y_{st} and z_{st} correspond to extrema of the potential), it is found that

$$V - V_{st} \propto \delta y^2, \delta z^2, \delta y\, \delta z\,. \tag{7.38}$$

Using (7.36) and taking the initial condition at an arbitrary τ_0 we find an expression for the decay of the potential

$$V(\tau) - V_{st} = [V(\tau_0) - V_{st}] \exp\left(-\varrho\,(\tau - \tau_0)\right). \tag{7.39}$$

In Fig. 7.8 we plot $\ln[V(\tau) - V_{st}]$ versus time and compare it with the approximation (7.39). One can see that it fits $\ln[V(\tau) - V_{st}]$ reasonably well not only near the steady state (where it was derived), but also during the transient dynamics. The value of τ_0, being a free parameter, was chosen at the time at which the first peak of the intensity appeared. Although other values of τ_0 might produce a better fit, the one chosen here has the advantage that it can be calculated analytically by following the technique of Ref. [Balle *et al.*, 1991]. It can be derived from Eq. (7.26) that the period T depends linearly on the potential V. This fact, combined with the result of Eq. (7.39), suggests the semi–empirical law for the evolution of the period

$$T(\tau) - T_{st} = [T(\tau_0) - T_{st}] \exp\left(-\varrho\,(\tau - \tau_0)\right). \tag{7.40}$$

This simple expression fits well the calculated period not only near the steady state, but also in the transient regime, see Figs. 7.7 and 7.9. The small differences observed near the steady state are due to the fact that the semi–empirical law, Eq. (7.40), is based on the validity of Eq. (7.26) between the period and the potential. As it was already discussed above, that expansion slightly underestimates the asymptotic (stationary) value of the period. By complementing this study with the procedure given in [Balle *et al.*, 1991] to describe the switch–on process of a laser, and valid until the first intensity peak is reached, we can obtain a complete description of the variation of the oscillations period in the dynamical evolution following the laser switch–on.

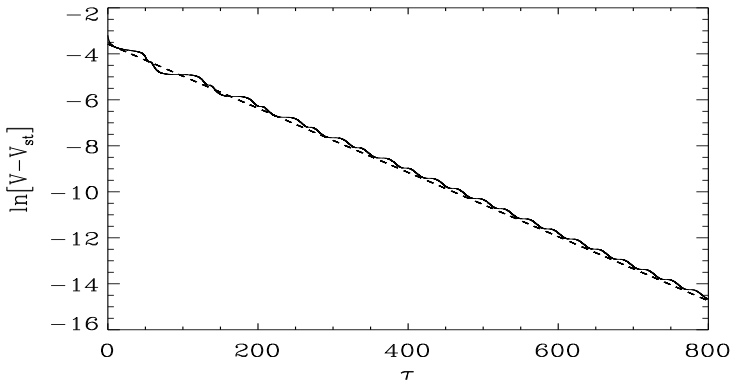

Figure 7.8: Logarithm of the potential difference versus time in a class B laser (solid line), compared with the theoretical expression in the steady state (7.39) (dashed line). Same parameters than in Fig. 7.1 and τ_0 as in Fig. 7.7. Dimensionless units.

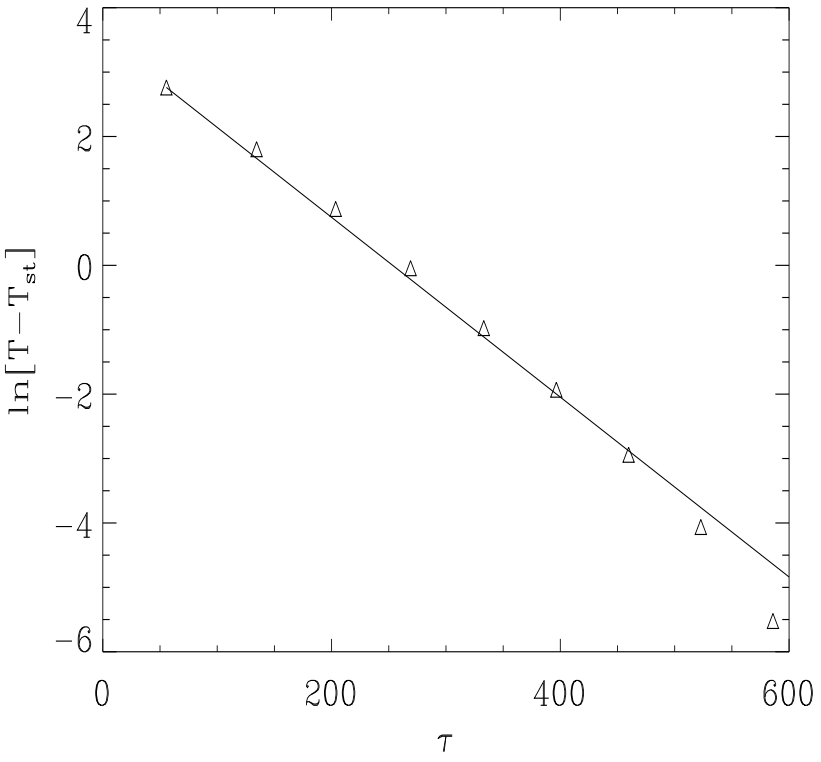

Figure 7.9: Logarithm of the period difference versus time in a class B laser. Triangles correspond to the period calculated from the simulations as the distance between two consecutive intensity peaks, at the same position than in Fig. 7.8. The solid line is the semi–empirical expression Eq. (7.40). Same parameters than in Fig. 7.1 and τ_0 as in Fig. 7.7. Dimensionless units.

Capítol 8

Estructura de resonàncies en un làser de classe B amb senyal injectat

En aquest capítol es descriu la dinàmica qualitativa i el conjunt parcial de bifurcacions (capítol 3) per a un làser de classe B amb senyal injectat amb termes de disintonia petits. El treball d'aquest capítol completa una sèrie d'estudis (veure la secció 1.2) sobre bifurcacions en làsers amb senyal injectat en la proximitat de la singularitat Hopf–sella–node.

Les equacions de balanç (capítol 4) en un sistema de referència que gira a la freqüència del senyal injectat són les (8.1) per al camp elèctric, E, i el nombre de portadors, W. El camp injectat està caracteritzat per l'amplitud β, i la freqüència η. Per al tractament que es fa en aquest capítol s'agafa un valor pel paràmetre de disintonia amb el qual les equacions queden tipus II de la bifurcació Hopf–sella–node.

En les distintes seccions d'aquest capítol es van introduint a poc a poc els distints conjunts invariants del sistema i les seves bifurcacions a causa de la complexitat del conjunt complet de bifurcacions. S'han seleccionat distints colors per a cada tipus de bifurcacions. El conjunt final obtingut és el de la figura 8.22.

La bifurcació sella–node (punts vermells) i la bifurcació de Hopf (punts blaus) dels punts fixos de les equacions, es poden calcular analíticament (8.4 - 8.6). La seva intersecció dóna el punt Hopf–sella–node. Aquestes bifurcacions separen les regions de l'espai de paràmetres (β, η) segons l'estabilitat dels punts fixos A, B i C, Fig. 8.1. A la regió 1, A és estable, B inestable i C sella; un parell d'aquests punts fixos s'aniquilen quan es creua els costats del triangle: cap a la regió 4, B i C col·lapsen; cap a les regions 6, 3 i $3'$, A i B s'aniquilen deixant en aquestes regions el punt C. Un punt fix estable existeix en les regions 1, 4 i 5, que correspon, en termes físics, a tenir una freqüència de sortida sintonitzada amb la d'entrada. El punt fix C correspon a l'estat del làser apagat, i en totes les regions d'interès és un punt sella.

La bifurcació de Hopf (primària) ocorr o bé en el punt fix A ò B, creant una òrbita periòdica transversal, T, al pla $W = 0$. Realitzant un circuit tancat al voltant

del punt Hopf–sella–node: de 1 a 5, el punt B inestable torna sella i es crea l'òrbita T inestable. Aquesta òrbita existeix fins a la regió 3, allà sofreix una bifurcació de Hopf (secundària) quan passa a la regió $3'$, creant un torus transversal inestable, Fig. 8.3. L'òrbita T estable continua existint en la regió 2, i mor en la bifurcació de Hopf (primària) amb el punt fix A. L'òrbita T té un període que divergeix per a valors de β petits (Fig. 8.10), desapareixent a l'òrbita homoclínica a C, Fig. 8.2.

Per completar el conjunt d'invariants en les regions 3 i $3'$, cal incloure una òrbita periòdica longitudinal, L, que és aproximadament coplanar al pla $W = 0$. Aquesta òrbita, estable a 3 però inestable a $3'$, té un període que divergeix a la bifurcació sella–node (bifurcació d'Andronov, Fig. 8.21).

Els punts fixos A i B, juntament amb l'òrbita T corresponen a l'escenari Hopf–sella–node tipus *II*. L'òrbita L és una part integral del conjunt de bifurcacions, i la interacció de les bifurcacions que sofreixen aquestes dues òrbites organitza l'estructura de resonàncies. La bifurcació de Hopf secundària s'interrompeix en una illa de bifurcacions de període doble d'òrbites periòdiques (cercle blau figura 8.2) i acaba en una bifurcació sella–node d'òrbites periòdiques (triangle rosa).

El moviment quasi–periòdic pot sofrir fenòmens de resonància i generar òrbites periòdiques. Aquestes òrbites poden ésser classificades per un nombre p de voltes seguint l'òrbita primària, T, i q que denota el nombre de voltes fetes al voltant l'òrbita primària abans de tancar–se. A la figura 8.7, es veu l'estructura de resonàncies per distints valors de q. Les línies en color rosa corresponen a bifurcacions sella–node d'òrbites periòdiques. Per a $q > 4$ es comporten com l'estructura estàndard de llengües d'Arnold i es van acumulant cap el punt Hopf–sella–node.

L'estructura de les òrbites periòdiques dins cada resonància és bastant similar. Com exemple s'estudia la resonància 3, Fig. 8.9. A la figura 8.10 (a), es veu que per a β a prop de la bifurcació de Hopf secundària de T, una òrbita periòdica inestable i una sella neixen i tornen a col·lapsar en un valor de β més gran a la bifurcació sella–node revers. Per a un valor de η més baix, Fig. 8.10 (b), la branca inestable té un període que divergeix i s'originen dues bifurcacions homoclíniques (cercle verd de la figura 8.9). El tall de la figura 8.10 (c) indica que l'òrbita periòdica resonant es junta amb l'òrbita L. Aquest procés d'unió de les resonàncies transversal en la solució de l'òrbita periòdica s'observa a totes les resonàncies. A prop del procés d'unió s'observa que l'òrbita L també bifurca en una Hopf secundària (línies negres per valors de β grans), que té així mateix té resonàncies 1/2 (cercles color blau corresponents a bifurcacions de període doble).

Les resonàncies fortes ($q \leq 4$) tenen una estructura més complicada que la indicada. En particular, les bifurcacions sella–node de les llengües no ocorr en el torus. El torus pot créixer quan els paràmetres canvien i col·lisionar amb una òrbita resonant. Això corresponen a una bifurcació homoclínica a una òrbita periòdica amb la destrucció final del torus (diamands negres). Els punts d'intersecció d'aquestes homoclíniques, les Hopf secundàries i les resonàncies corresponen a singularitat tipus Takens–Bogdanov, Fig. 8.15.

Entre les resonàncies transversals indicades, s'han obtingut altres resonàncies, Fig. 8.18, encara que una classificació de les mateixes és prou complicada.

Chapter 8

Resonance structure in a class B laser with injected signal

In this chapter, we describe the qualitative dynamics and bifurcation set for a laser with injected signal for small cavity detunings by using the definitions included in chapter 3.

The work presented in this chapter completes the above series of studies of bifurcations of a laser with injected signal in the neighbourhood of the Hopf–saddle–node (HSN) singularity, as it was reviewed in section 1.2. We numerically analyse the weak cavity detuning regime for a fixed value of the detuning parameter $\theta = 0.5$ (in adequate units), where type *II* Hopf–saddle–node is expected. The small–detuning case is particularly relevant for applications, since a natural ambition when constructing laser cavities is to obtain low detunings. Long–time behaviour depending on the amplitude and the frequency shift of the applied signal is studied. The main bifurcation structure consists of a (secondary) Hopf bifurcation on the periodic orbit associated to the Hopf–saddle–node bifurcation. We have analysed in detail the resonance structure which reveals a rich interaction with other bifurcations *not* present in the usual Hopf–saddle–node scenario.

In the next section we review the representative equations for a laser with injected signal, together with the unfolding of the Hopf–saddle–node bifurcation. In Sec. 8.2, the resonance structure is described, while Sec. 8.3 discusses the Andronov global bifurcation occurring in this laser, and its interaction with other bifurcations. Finally, a global outlook and discussion is given in Sec. 8.4.

8.1 Equations for the laser with injected signal

The model for a laser system is given in terms of the Maxwell–Bloch equations, chapter 4. In a great variety of lasers, the decay times associated with the population inversion and the electric field have different time scales, allowing for the adiabatic elimination of the fast decaying polarization variable (class B) [Solari and Oppo, 1994]. The dimensionless rate equations in a reference frame that rotates with the

injected signal may be written as

$$\begin{aligned} \frac{dE}{dt} &= EW + i(\theta W + \eta)E + \beta, \\ \frac{dW}{dt} &= A^2 - \chi W(1 + g|E|^2) - |E|^2, \end{aligned} \tag{8.1}$$

where E is the complex envelope of the electric field and W is proportional to the population inversion. θ represents the detuning between the atomic and the nearest eigenfrequency of the cavity, A is proportional to the amount of pumped atoms, $\chi \geq 0$ is proportional to the inverse of the decay time of the population inversion and g is inversely proportional to $1+\theta^2$. For typical lasers, χ is small. η is the detuning of the perturbation frequency and the unperturbed laser operating frequency and $\beta \geq 0$ is the intensity of the injected signal. The relationship between the parameters used in this model and the parameters in the Maxwell–Bloch equations can be found in [Solari and Oppo, 1994]. The model can be justified for small signal intensity ratio, $\beta/A^2 \ll 1$, although it has been argued that it can be successfully applied beyond this limit [Oppo *et al.*, 1986]. Our present study centers in this limit and in some cases we have explored a region beyond this limit in order to understand the fate of some invariant sets. The set of equations (8.1) can be obtained from Eqs. (4.11) and (4.12), in the absence of noise terms and without injected signal, by performing the suitable change of variables.

Solari and Oppo [1994] performed a reduction of the three–equations model by averaging over the fast relaxation oscillation motion, reducing the dynamics to a two–equations system. In this way, the difficulty of finding analytic expressions for most of the local bifurcations is simplified. A close analysis of the singularities of this model, reveals that the system organizes around the codimension–2 Hopf–saddle–node local bifurcation. One finds that after a suitable change of coordinates one may arrive to its normal form representation (3.1) [Guckenheimer and Holmes, 1983]

$$\begin{aligned} r' &= (\mu + \bar{a}\, v)\, r + \mathcal{O}(3), \\ v' &= \nu + \bar{b}\, r^2 - v^2 + \mathcal{O}(3), \\ \zeta' &= \bar{c} + \bar{a}\, v + \mathcal{O}(2), \end{aligned} \tag{8.2}$$

where $\bar{a}$, $\bar{b}$, $\bar{c} \neq 0$ and μ and ν are the bifurcation parameters, all function of the laser parameters. The signs of $\bar{a}$ and $\bar{b}$ classify different types of flows: type I for ($\bar{a} > 0$, $\bar{b} > 0$), type II for ($\bar{a} < 0$, $\bar{b} > 0$), type III for ($\bar{a} > 0$, $\bar{b} < 0$), type IV for ($\bar{a} < 0$, $\bar{b} < 0$).

One of the main achievements of the Solari and Oppo average model is that they have established that the actual laser with injected signal operation is controlled by the cavity detuning parameter θ in the following way:

type II: $0 < \theta < 1$,
type I: $1 < \theta < \sqrt{3}$,
type III: $\sqrt{3} < \theta$.

We refer the reader to [Zimmermann *et al.*, 2001] for a detailed account of the normal form computations for the three–dimensional laser with injected signal equations (8.1), where the above results are validated up to order $O(\chi^2)$, for

$$\begin{aligned}
\bar{a}(\theta) &= (1+gA^2)\frac{(\theta^2-1)}{4\theta}\chi + O(\chi^2), \\
\bar{b}(\theta) &= -(1+gA^2)\frac{(1+\theta^2)(\theta^2-3)}{8\theta}\chi + O(\chi^2), \\
\bar{c} &= \sqrt{2}A + O(\chi^2), \\
\mu(\beta,\eta) &= \theta\left(\frac{2}{1+\theta^2} - \frac{\chi}{\beta\theta\sqrt{1+\theta^2}}\right), \\
\nu(\beta,\eta) &= 2\left(\frac{\beta\sqrt{1+\theta^2}+\eta}{\beta(1+\theta^2)}\right).
\end{aligned} \tag{8.3}$$

The main characteristics of each type of flow may be summarized as follows. A saddle–node bifurcation occurs for $\nu = \nu_{\rm sn} = 0$, where a pair of saddle–focus fixed points are born at $(r, v) = (\pm\sqrt{\nu}, 0)$. These fixed points may as well bifurcate in a Hopf bifurcation along a parabola in parameter space, $\nu = \nu_{\rm Hopf} = \mu^2/\bar{a}^2$. The periodic orbit will be at $v_{\rm Hopf} = -\mu/\bar{a}$ and its radius is given by $r^2_{\rm Hopf} = (\mu^2/\bar{a}^2 - \nu)/\bar{b}$. The main differences between type *I-III*, lie in the region of existence and stability of the periodic orbit. In type *III* the periodic orbit always co–exists with the fixed points ($\nu > \mu^2/\bar{a}^2 > 0$), while in type *I* the periodic orbit exists before the creation of the fixed points (for $\nu < 0$, $r_{\rm Hopf} > 0$). Type *II* is similar to type *I*, but the stability of the periodic orbit may change. A degenerate (secondary) Hopf bifurcation occurs on the semiaxis $\mu = 0, \nu < 0$, where the periodic orbit becomes a center. Addition of appropriate third order terms to the normal form (8.2) breaks, in general, this degeneracy resulting in a bifurcation to a torus. The fate of the torus will depend on the perturbation applied to (8.2) and results concerning this type are unknown. Kirk [Kirk, 1991] has analysed these kind of perturbations for type *III*, where the secondary Hopf bifurcation occurs in the semiaxis $\mu = 0, \nu > 0$, coexisting with the fixed points. In her analysis she found that the torus breaks–up in Arnold tongues [Arnold, 1983], which in turn ends up as *resonances of another secondary Hopf bifurcation*. Below a similar scenario will be found.

In this work we investigate the small detuning regime $0 < \theta < 1$ corresponding to type *II*, a case not studied in complete detail in previous works. In terms of bifurcations and periodic orbit organization, the most prominent feature is the (secondary) Hopf bifurcation of periodic orbits associated to the Hopf–saddle–node singularity. This will be one of our main objects of study, where we will discuss the interaction of its resonances with other bifurcations not present in the (local) normal form analysis.

8.2 Bifurcation set for small detuning

We have integrated numerically equations (8.1) with fixed parameters $A = 1$, $\chi = 0.3$ and $g = 0$[1]. Most computations were done with the AUTO97 [Doedel *et al.*, 1997] continuation package, in the parameters (β, η) and $0 < \theta = 0.5 < 1$. In general, the locus in parameter space of a particular bifurcation will be presented as points, representing the actual computation performed. To guide the reader we have selected different colours for each type of bifurcation.

Given the complexity of the full bifurcation set found, we will introduce in steps the different invariant sets and their bifurcations. Readers not interested in the technical details of the calculation may refer to Fig. 8.22 for the full bifurcation set discussed in this chapter.

8.2.1 Invariant sets close to the Hopf–saddle–node bifurcation

We begin our numeric exploration with the locus of the saddle–node, Hopf and Hopf–saddle–node bifurcations of fixed points. These may be explicitly computed, with the relevant equations being:

1. The fixed point equation may be reduced to,

$$\begin{aligned}(1+\theta^2)Y^3 &- 2[A^2(1+\theta^2)+\chi\eta\theta]Y^2 \\ &+ [A^4(1+\theta^2)+2A^2\chi\eta\theta+\chi^2\eta^2]Y-\chi^2\beta^2=0,\end{aligned} \tag{8.4}$$

   a cubic polynomial in $Y = |E|^2$.

2. The saddle–node condition, i.e., when one of the eigenvalues of the Jacobian is zero,

$$3(1+\theta^2)Y^2-4[A^2(1+\theta^2)+\chi\eta\theta]Y+A^4(1+\theta^2)+2A^2\chi\eta\theta+\chi^2\eta^2=0. \tag{8.5}$$

3. The Hopf condition (i.e., when two (complex conjugated) eigenvalues of the Jacobian are pure imaginary) reads

$$\begin{aligned}&(1+\theta^2)Y^3-[3A^2(1+\theta^2)+\chi^2(\theta^2-3)+2\eta\chi\theta]Y^2 \\ +\;&[3A^4(1+\theta^2)+A^2[(\theta^2-5)\chi^2+4\eta\chi\theta]+2\chi^4+\theta\chi^3\eta+\eta^2\chi^2]\,Y \\ -\;&[(1+\theta^2)A^6+2A^4(\eta\chi\theta-\chi^2)+A^2(\eta^2\chi^2+\chi^4)]=0.\end{aligned} \tag{8.6}$$

The fixed point equation reveals that there are regions of one or three fixed points, separated by saddle–node bifurcations. The simultaneous solution of (8.4) and (8.5) (the fixed point equation will then have a double root) gives the locus of

[1] In real lasers $g \in [0, 1]$. However, the qualitative features of the bifurcations around the Hopf–saddle–node bifurcation will not change if g is kept small. In [Zimmermann *et al.*, 2001] it is found to slightly modify the second–order coefficients in the Hopf–saddle–node normal form.

the saddle–node curve, while solution of (8.4) with (8.6) gives the locus of the Hopf curve. When all three equations are simultaneously satisfied there is a tangency point where the Hopf–saddle–node occurs [Zimmermann *et al.*, 2001],

$$\begin{aligned} \eta_{\rm hsn}(\theta) &= -\frac{(1+\theta^2)}{2\theta}\left(1-\frac{1}{4\,\theta^2 A^2}\,\chi^2\right)\,\chi+\mathcal{O}(\chi)^4, \\ \beta_{\rm hsn}(\theta) &= \frac{A\,\sqrt{1+\theta^2}}{2\theta}\left(1-\frac{(1+\theta^2)}{4\,\theta^2 A^2}\,\chi^2\right)\,\chi+\mathcal{O}(\chi)^4. \end{aligned} \tag{8.7}$$

A typical bifurcation set displaying these bifurcations is shown in Fig. 8.1. Inside the "triangle" shaped region, three fixed points exist, while outside this region only one fixed point remains. Let us label the fixed points in region 1 as: A stable, B unstable and C saddle. A pair of the above fixed points are annihilated crossing the sides of the triangle: moving into region 4, B and C collide, while entering region 6 or (3, 3′), A and B annihilates leaving in these regions only the fixed point C.[2] In physical terms, *locking* behaviour (output frequency tuned to that of the injected signal) occurs whenever the laser is operated in any of the regions (1, 4, 5), where a stable fixed point exists. On the other hand, fixed point C exists in all regions except 4 in Fig. 8.1 and is approximately situated in $(|E|, W) \approx (0, A^2/\chi)$ for $\beta \ll 1$, which corresponds to the laser–off state. In all regions of interest it is a saddle fixed point.

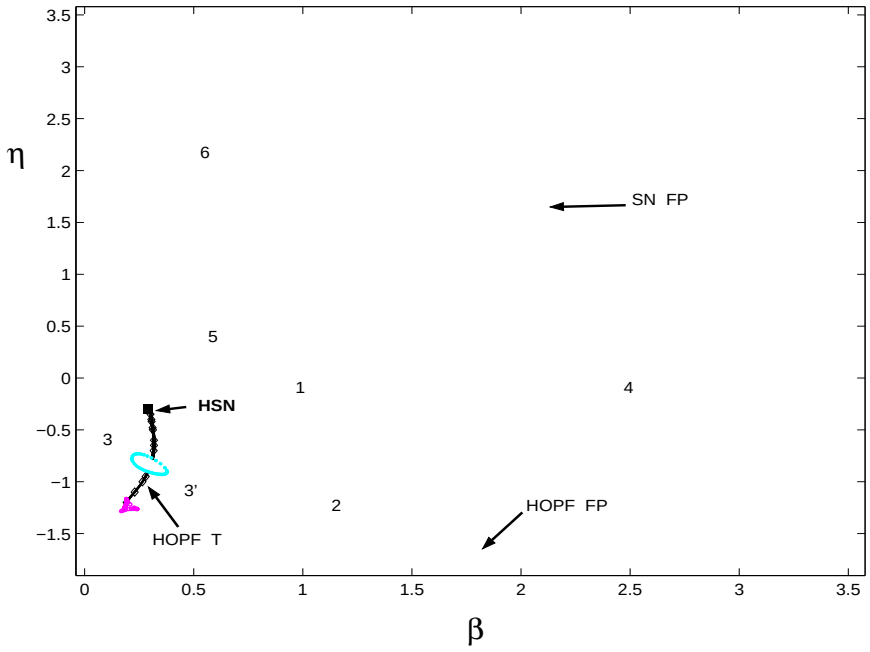

Figure 8.1: Numerical bifurcation set in parameters (β, η) for type *II*. Red line: saddle–node of fixed points (SN FP). Blue line: Hopf bifurcation of fixed points (HOPF FP). The secondary Hopf bifurcation of transversal periodic orbits (HOPF T) separates region 3 and 3'.

[2]Notice that choosing a path far out from the "triangle" shaped region, we have to identify fixed point C in regions (6, 3, 3′) with fixed point A in region 4.

The (primary) Hopf bifurcation occurs on either fixed point A or B, creating a periodic orbit *transversal* to the $W = 0$ plane, which will be referred to as T in what follows. This orbit corresponds to the undamped relaxation oscillation [van Tartwijk and Lenstra, 1995], whose main characteristic is that the phase of the electric field remains bounded. A close inspection in parameter space around the Hopf–saddle–node point reveals that moving from region 1 to region 5, the unstable node B becomes a saddle and creates an unstable T orbit. This orbit exists up to region 3, where it suffers a (secondary) Hopf bifurcation when crossing to region $3'$, creating an unstable transversal torus. The remaining stable T periodic orbit continues to exist up to region 2, when it dies in a (primary) Hopf bifurcation with fixed point A.

To complete the main invariant sets present in region 3 and $3'$, we have to include another periodic orbit. For sufficiently small β we find from (8.1) that for $W \approx 0$, $|E| \approx A$ and the phase $\arg(E(t)) = \eta\ t$, which corresponds to the *cw* (continuous-wave) laser solution [van Tartwijk and Lenstra, 1995] with an unbounded electric field phase. As this orbit lies approximately coplanar to the $W = 0$ plane, it will be referred to as L, the *longitudinal* orbit. For sufficiently small (η, β), this orbit can be easily shown to be stable. However we find that the period of L diverges at the saddle–node bifurcation of fixed point, where the orbit disappears. This global bifurcation is known as Andronov or saddle–node infinite–period bifurcation [Kuznetsov, 1997], and will be addressed in more detail in Sec. 8.3. We remark that the stability of L close to the Andronov bifurcation depends on the stability of the saddle–node fixed point, thus on which side of the Hopf–saddle–node point one is located: in region $3'$ the orbit is unstable, while in region 3 it is stable. From this, it is clear that at least a local bifurcation to L is required. Below we will show that a new secondary Hopf bifurcation on L occurs inside region $3'$.

In summary, we find that fixed points A and B together with the transversal periodic orbit T correspond to the type *II* Hopf–saddle–node scenario proposed by the normal form analysis in the previous section. The periodic orbit L is also an integral part of the bifurcation set of a laser with injected signal, and we will show in the next section how the interaction of bifurcations between these two periodic orbits organize the resonance structure.

8.2.2 Bifurcations of transversal periodic orbits

We begin with a general observation for the existence boundary of transversal T orbit born at the the Hopf bifurcation of fixed points. For a fixed value of η, we find for the continuation of this orbit for decreasing β, its period diverges at a critical $\beta \approx 0.05$, for an interval of η close to 0, where a homoclinic orbit to fixed point C occurs. Figure 8.2 shows the locus of this global bifurcation in parameter space, while Figs. 8.10 and 8.11 show the typical period versus β behaviour. This bifurcation is found not to depend on θ, and was found up to type *III* regime. We leave for Sec. 8.3 the discussion of how this bifurcation is related to the Andronov bifurcation producing L.

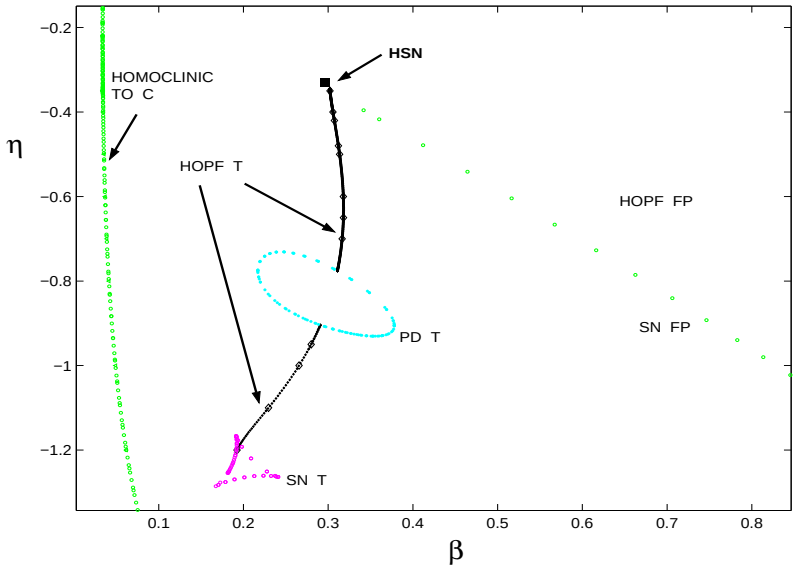

Figure 8.2: Partial numerical bifurcation set showing the homoclinic to C fixed point and the first resonances of the transversal secondary Hopf bifurcation. Saddle–node bifurcation of transversal periodic orbits (SN T) and period doubling bifurcation of transversal periodic orbits (PD T) are indicated.

In Fig. 8.3 (a) we display the main invariant sets for the parameter region bounded by the homoclinic to C and the secondary Hopf bifurcation. We have the stable longitudinal orbit L (which lies approximately on $|E| \approx A = 1, W \approx 0$), together with the unstable transversal orbit T. This orbit has a large variation in the population inversion W, and a bounded electric field phase (the phase does not make a complete turn as L does). Crossing the secondary Hopf bifurcation T and entering region $3'$, we find that T becomes stable and an unstable invariant torus is created. Figure 8.3 (b) shows the invariant sets, where only the intersections of the quasiperiodic orbit with the $W = 0$ plane are shown. A time series of the intensity $|E|^2$ on this solution is shown in Fig. 8.4.

It is well known that in generic systems quasiperiodic motion may suffer resonance phenomena. Local analysis [Arnold, 1983] around the Hopf bifurcation reveals that whenever the ratio of the two competing frequencies is rational, the quasiperiodic motion may disappear and periodic orbits arise. These orbits may be classified by an integer number of p turns following the primary or bifurcating orbit (T in this case), and another integer number q which denotes the number of turns made around the primary orbit, before closing on itself. Precisely on the (secondary) Hopf bifurcation the nontrivial Floquet multipliers are on the unit circle at $e^{\pm i2\pi p/q}$. A general result shows that in the *weak resonances* case $q > 4$ these periodic orbits are born in saddle–node pairs, and in a two–parameter space they trace a 'tongue' (known as Arnold tongue) with the tip lying on the (secondary) Hopf bifurcation. In phase space the periodic orbits are *phase locked* solution on the torus. On the other hand the case $q \leq 4$ are known as *strong resonances* and do not correspond to 'strict' Arnold tongues. The details of each strong resonance in a general study may be found in [Kuznetsov, 1997].

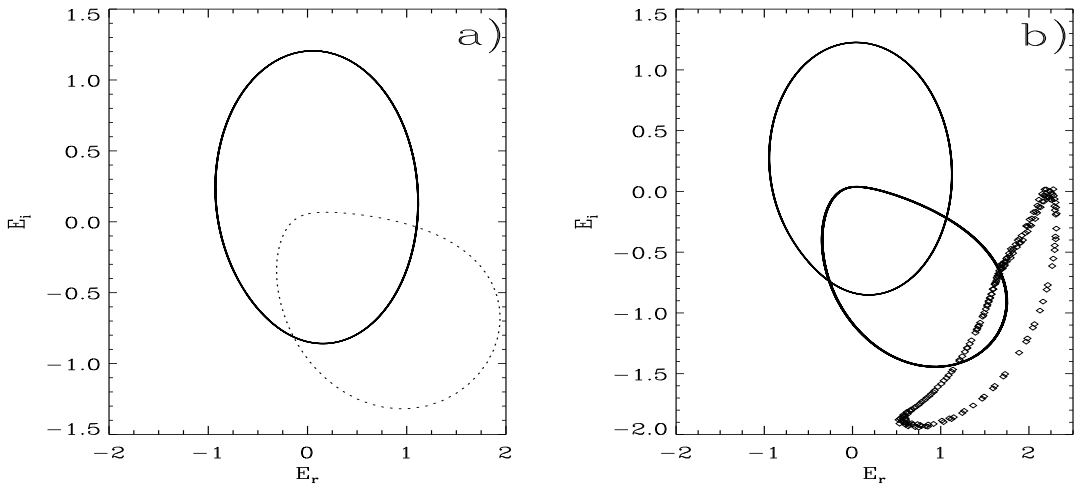

Figure 8.3: Phase portrait in $(E_r = Re(E), E_i = Im(E))$ of periodic orbits in the neighbourhood of the (secondary) Hopf bifurcation of T. Solid lines: stable orbits, dot lines: unstable trajectories. $\eta = -1$. (a) $\beta = 0.24$, (b) $\beta = 0.28$. The torus created is an unstable one.

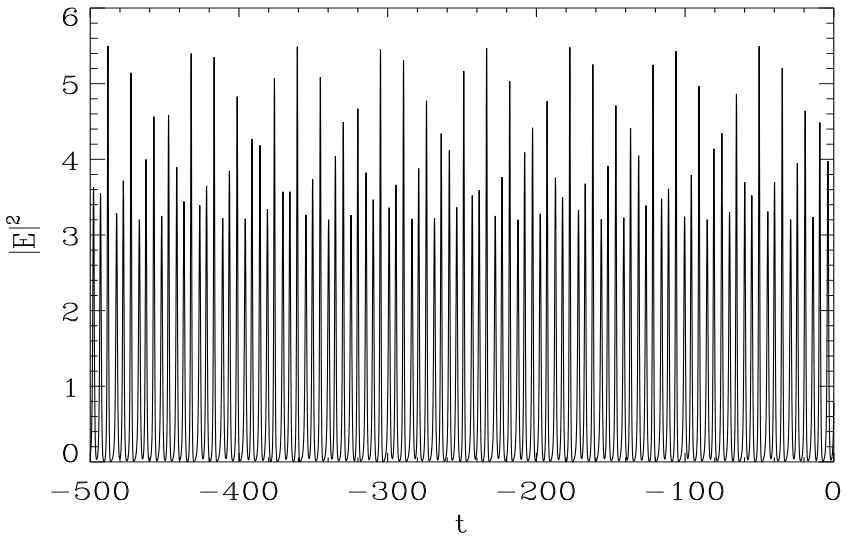

Figure 8.4: Intensity ($|E|^2$) versus time for the unstable transversal torus created in the Hopf bifurcation of T periodic orbits. $\eta = -1$, $\beta = 0.28$.

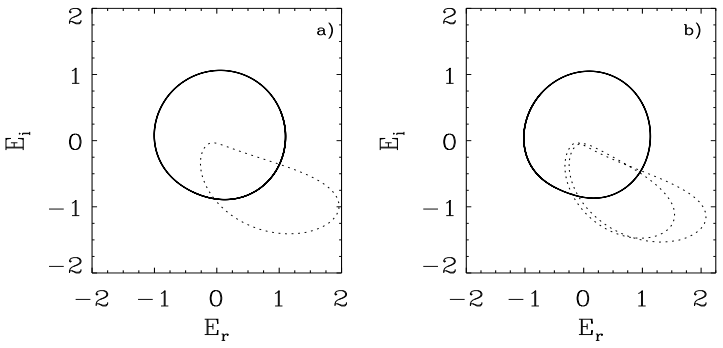

Figure 8.5: Projections in the plane (E_r, E_i) of the orbits that exist in each side of the period doubling bifurcation. Solid lines: stable orbits, dot lines: unstable trajectories. Saddle orbits are not represented. $\eta = -0.8$. (a) $\beta = 0.2$, (b) $\beta = 0.23$.

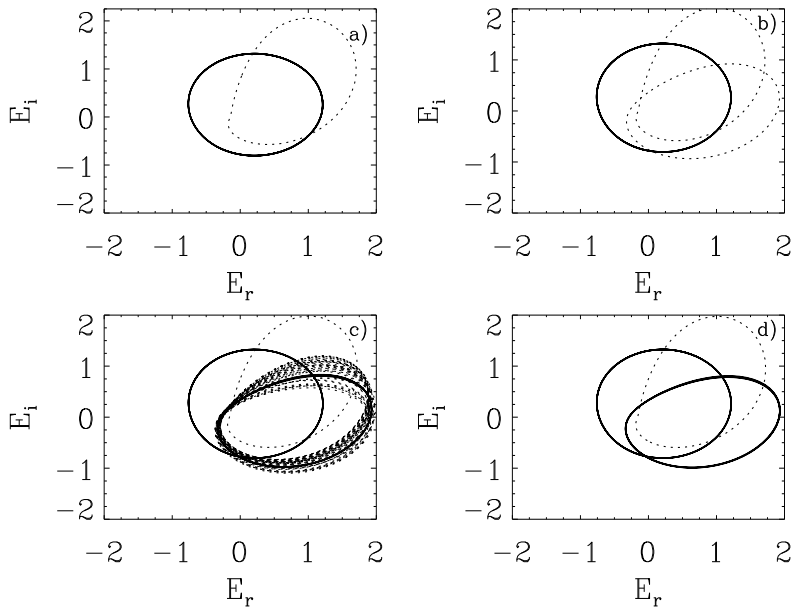

Figure 8.6: Projections in the plane (E_r, E_i) of the orbits that exist in different regions of Fig. 8.15. Solid lines: stable orbits, dot lines: unstable trajectories. Saddle orbits are not represented. $\eta = -1.2$. (a) Region B, $\beta = 0.19$, (b) Region F, $\beta = 0.192$, (c) Region G, $\beta = 0.1939$, (d) Region H, $\beta = 0.1942$. The bifurcations between the different regions are: from B to F a saddle–node bifurcation, from F to G a Hopf bifurcation of periodic orbits, and from G to H a homoclinic of periodic orbits.

In Fig. 8.7 we display the resonance structure for $1/q, q = 1, .., 12$, where the saddle–node of the resonant periodic orbits have been continued in parameter space. Of course in general one expects a countable number of tongues, one for each rational p/q. We will show below the location of other resonances with $p \neq 1$. We find that the tongues corresponding to $q > 4$ behave like standard Arnold tongues, while $q = 1, 2, 3, 4$ behave in a different way as expected. Resonance $q = 4$ is well known not to finish in a cusp singularity (compare with [Kirk, 1991]), while resonance $q = 3$ does not even finish in a cusp bifurcation (see below for a detailed description of this resonance). For lower η, resonance $q = 2$ arises whenever the nontrivial Floquet multipliers of the primary periodic orbit (T) collide in a doubly degenerate -1 eigenvalue. In this case, we find in parameter space the Hopf bifurcation is interrupted by an "isola" of period doubling bifurcations (PD T in Fig. 8.7), see Fig. 8.5. For even lower η we find that the Hopf bifurcation is finally interrupted when the two nontrivial Floquet multipliers become degenerate at $+1$. In this case a saddle–node bifurcation of periodic orbits occurs (SN T in Fig. 8.7), see Fig. 8.6, and in fact a Takens–Bogdanov [Kuznetsov, 1997] singularity takes place. In Sec. 8.2.4 we discuss this with more detail.

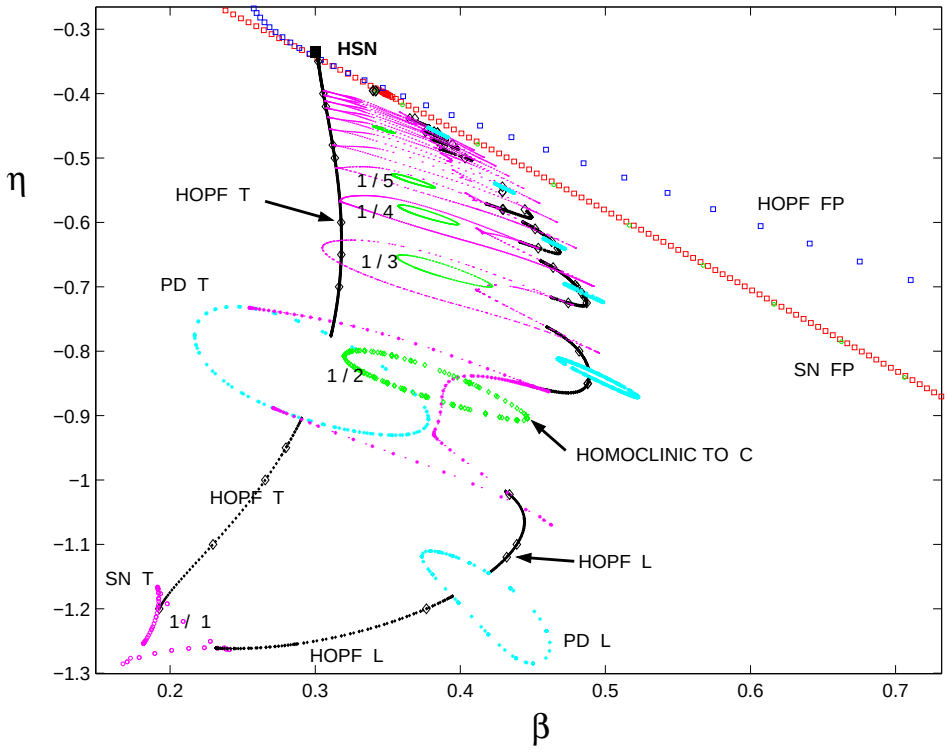

Figure 8.7: Resonance structure for the transversal and longitudinal Hopf bifurcations, together with the homoclinic bifurcation to fixed point C. Period doubling bifurcations of longitudinal orbits (PD L) and Hopf bifurcations of longitudinal orbits (HOPF L) are displayed.

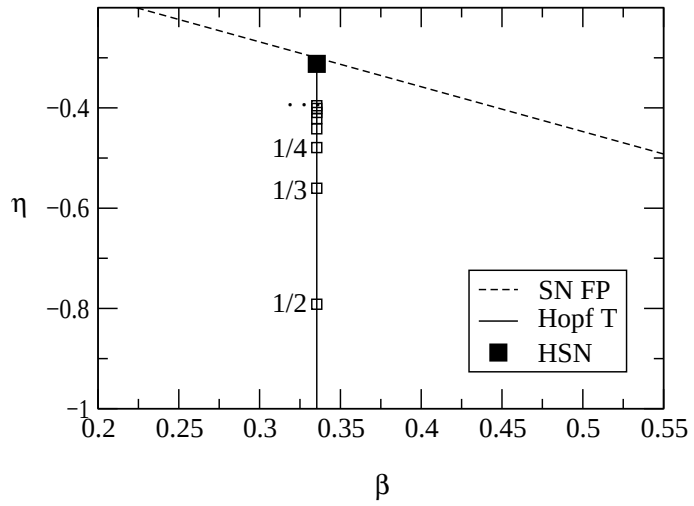

Figure 8.8: Secondary Hopf bifurcation and its resonances $p/q = \{1/2, 1/3, 1/4, ..\}$ from an estimation of the Hopf–saddle–node normal form (8.2) using the laser with injected signal parameters (β, η). The dashed line is the saddle–node of fixed points while the vertical line is the secondary Hopf bifurcation. Compare with Fig. 8.7. ($A = 1$, $\theta = 0.5$, $\chi = 0.3$).

The organization of the tongues in parameter space shows that for increasing q, the resonances appear to accumulate *towards* the Hopf–saddle–node singularity. This may be easily understood by a simple analysis from the Hopf–saddle–node normal form. Truncating the normal form (8.2), the eigenvalues of the Hopf periodic orbit (corresponding to T) at the (degenerate) secondary Hopf bifurcation $\mu = 0, \nu < 0$ are $\lambda_{1,2} = \pm i\ \omega_1 = \pm i\sqrt{2\bar{a}\nu}$. Using the expression of $\bar{a}(\theta)$ and c in (8.3) we may estimate the position of the resonances in parameter space solving

$$p\bar{c} = q\omega_1(\nu), \tag{8.8}$$

for each pair of p, q. It is clear that moving on the secondary Hopf and approaching the Hopf–saddle–node singularity ($\nu \to 0$), the typical secondary frequency ω_1 goes to zero, so a larger q is required to satisfy the resonance condition. Figure 8.8 shows the result of this estimation of the resonance condition using the approximate reparametrization of the laser with injected signal (β, η) parameters in terms of Hopf–saddle–node parameters (8.3):

$$\eta(\mu,\nu) = \frac{(1+\theta^2)(\nu-2)\chi}{2(-2\theta+\mu(1+\theta^2)}, \qquad \beta(\mu,\nu) = \frac{\sqrt{1+\theta^2}\chi}{-2\theta+\mu(1+\theta^2)}. \tag{8.9}$$

The resonance structure is very similar to the one identified by Kirk [Kirk, 1991], but for type *III* Hopf–saddle–node. The main difference is that in this type the invariant torus coexists with the two fixed point solutions, and the possible homoclinic/heteroclinic between them. Her main result was that the Arnold tongues accumulated for increasing winding number towards this homoclinic/heteroclinic bifurcation present for this particular type. In our case we observe that the accumulation of the tongues saddle–nodes is onto the Andronov global bifurcation, occurring at the saddle–node of fixed points.

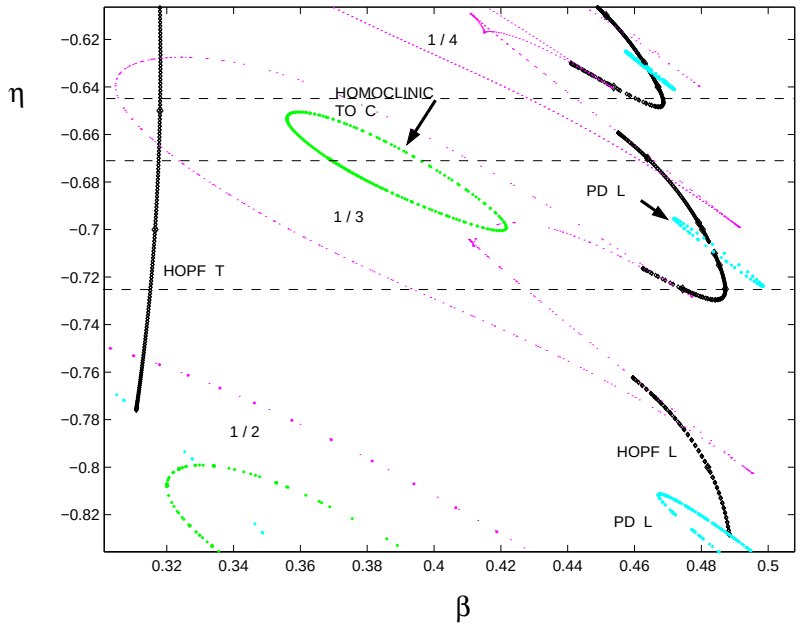

Figure 8.9: Partial numerical bifurcation set around the 1/3 resonance. The horizontal lines are constant–η parameter cuts shown in Fig. 8.10.

8.2.3 Structure and truncation of Arnold tongues

A closer look at how the periodic orbits are organized inside each resonance $q > 2$ is very interesting. To fix ideas we take resonance $q = 3$ shown in Fig. 8.9. We have performed three constant–η parameter cuts displayed in Fig. 8.10, where the period of the orbits as a function of β is shown. In each panel the unstable T periodic orbit is seen to born at $\beta \approx 0.05$ (with diverging period) in a homoclinic bifurcation to C, becoming stable at $\beta \approx 0.30$ in the (secondary) Hopf bifurcation. Also for low β we observe the stable L orbit which suffers a number of saddle–node and Hopf bifurcations as β increases, and finally its period diverge as it approaches at $\beta \approx 0.60$ the saddle–node infinite–period (Andronov) bifurcation.

In Fig. 8.10 (a), close to the Hopf bifurcation of T, a saddle and unstable periodic orbit are born in a saddle–node bifurcation and collide at a higher β in a reverse saddle–node bifurcation. Both bifurcations corresponds to the resonance boundaries shown in Fig. 8.9. For a slightly lower constant–η cut [Fig. 8.10 (b)], we find that the periof of the unstable branch of the resonant periodic orbits "explotes" and two homoclinic bifurcations to C originate. These global bifurcations correspond to the isola of homoclinics to C observed in Fig. 8.9. Finally, in a cut further away from the $q = 3$ resonances of the Hopf of T [Fig. 8.10 (c)], the homoclinics to C disappear and with the aid of another saddle–node bifurcation, the resonant periodic orbits "merge" with the L periodic orbit. Notice in Fig. 8.10 (a) that resonance $q = 4$ already merged to L. The above merging process of transversal resonances into the longitudinal periodic solution is observed for all resonances $1/q$, $q > 2$.

The $q = 2$ resonance reveals a more complex structure due to the fact that it interacts with the period doubling bifurcation of periodic orbits. In Fig. 8.11, the period of the orbits as a function of β for different values of η in this resonance is shown.

One may wonder if there is a topological restriction for the merging process, as the transversal orbit (and its associated resonances) are *linked* in phase space to the longitudinal orbit L, as shown in Fig. 8.3. For this, in Fig. 8.12 (a)–(c) we illustrate a continuation of L, T and a resonant orbit in order to show how the link of a transversal orbit remains as it merges to a longitudinal orbit.

In fact, close to the merging process, the longitudinal orbits L also bifurcates in a secondary Hopf bifurcation. Figure 8.13 (a) illustrates the unstable L longitudinal orbit born at the Andronov bifurcation, bifurcating in a secondary Hopf bifurcation and creating a new unstable longitudinal torus around L [Fig. 8.13 (b)]. Notice also that the electric field intensity time series Fig. 8.14 is also quite different of that of Fig. 8.4.

The remarkable feature is the organization in parameter space of the above bifurcations. We have found that all $1/q$ transversal resonances, end up in a cusp bifurcation with another saddle–node bifurcation. The latter bifurcation is the responsable for the merging described above, and on this branch a $1/q' = 1/1$ secondary Hopf bifurcation occurs on L. Continuation of the new Hopf bifurcation reveals that it suffers a $1/2$ resonance (with a period doubling isola), before it ends at another $1/q' = 1/1$ resonance, corresponding to a transversal tongue $1/(q-1)$. This sequence of bifurcations is seen to occur for all the transversal $1/q$ resonances found.

The complete structure of the phase diagram of Fig. 8.7 has now been described and reveals a high organization which repeats as we approach to the Hopf–saddle–node point. Several bifurcations not present in the local description of Hopf–saddle–node take part of the dynamics: (a) we have the Arnold tongues which for increasing q accumulate to the Andronov bifurcation, (b) the secondary longitudinal Hopf bifurcation connecting subsequent transversal resonances, and (c) the homoclinic bifurcations to C (the off state). The latter global bifurcations have a winding number in correspondence with the resonance to which it belongs. Thus in the limit close to Hopf–saddle–node one expects an accumulation of homoclinic orbits to C of diverging winding number. Furthermore, most turns would follow the smaller loop T, as we approach Hopf–saddle–node. This argument points to the possibility that another global connection between the Hopf–saddle–node fixed point and the laser off state C exists. This has not been explored in detail and deserves further study (see Sec. 8.3 below).

8.2.4 Homoclinics to periodic orbits

As mentioned above, all strong resonances are known to posses more bifurcation structures than those that we have pointed out. In particular, it is well known that unlike what happens in weak resonances, the saddle–node bifurcations of the tongues

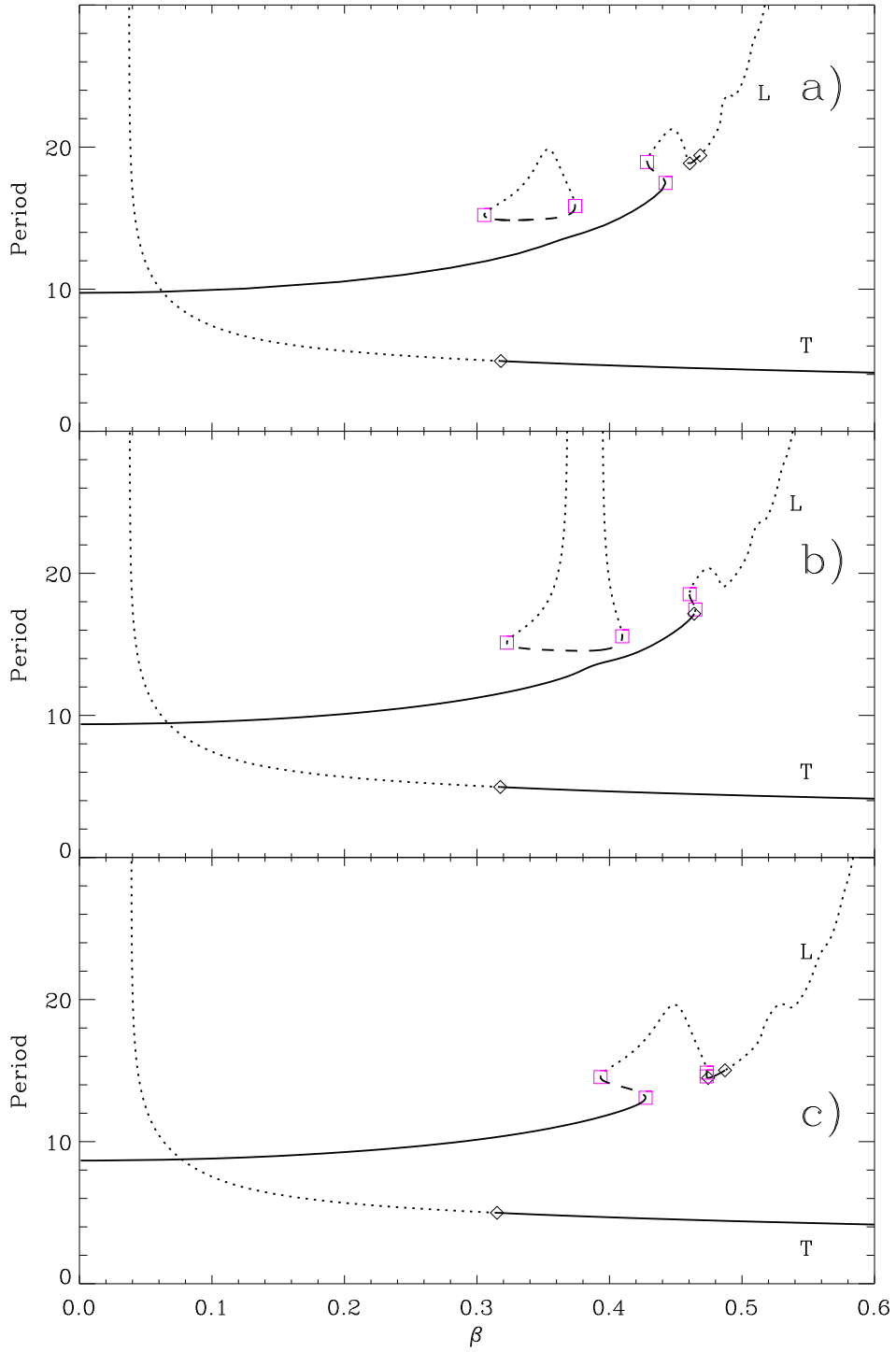

Figure 8.10: Period versus β of periodic orbits inside the resonance $q = 3$. (a) $\eta = -0.645$: the two saddle–node bifurcations forms an "isola" for the resonant periodic orbits close to the HOPF T bifurcation. (b) $\eta = -0.670$: the saddle branch of the isola "explodes" in period, creating two homoclinic bifurcations to C. (c) $\eta = -0.725$: the resonant branch of $q = 3$ periodic orbits merges with the L branch. Merging of the $q = 4$ resonance is also observed in (a). Solid line: stable orbit, dotted line: unstable orbit, dashed line: saddle orbit, squares: saddle–node bifurcations of periodic orbits, diamonds: Hopf bifurcations of periodic orbits.

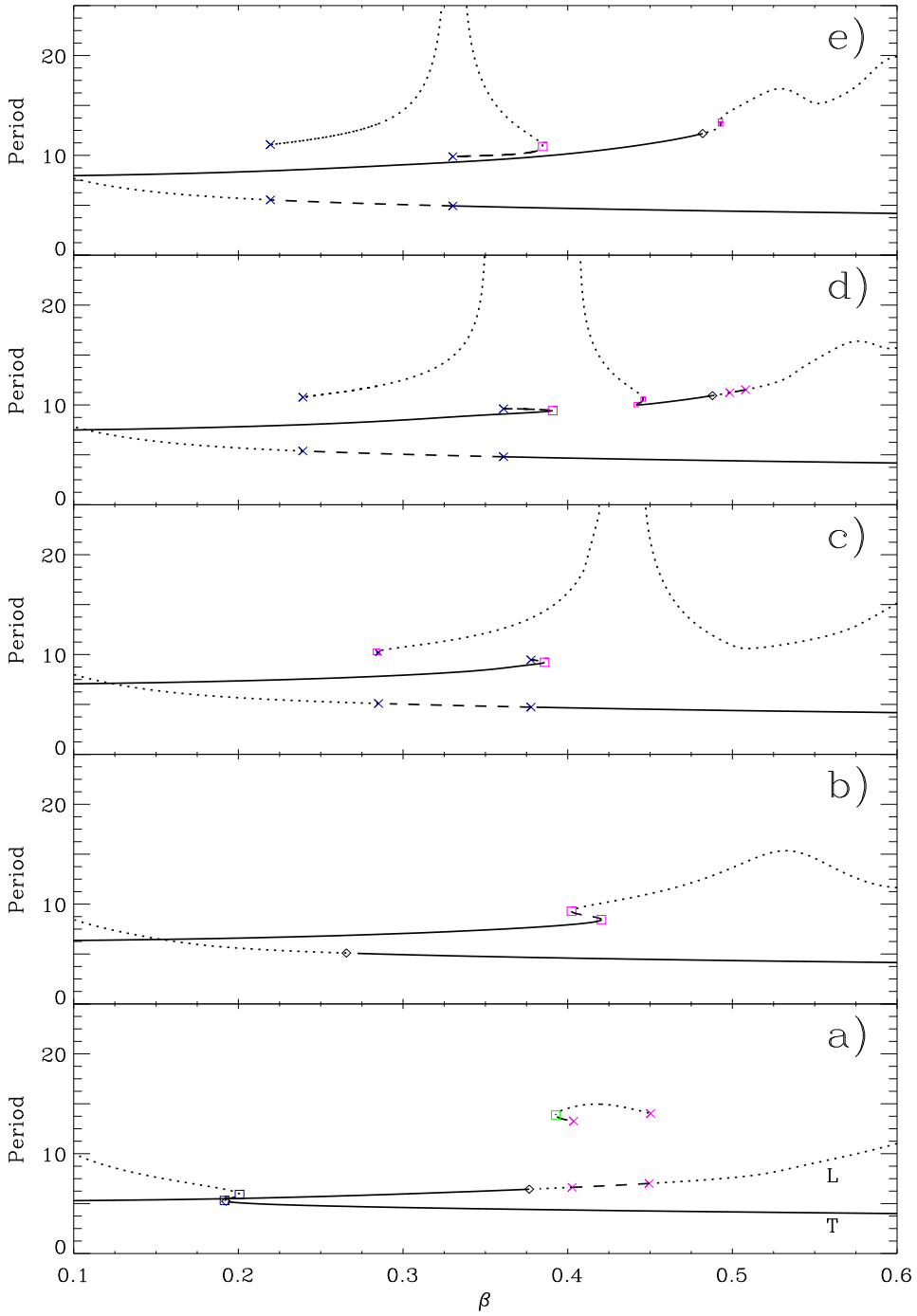

Figure 8.11: Period of the orbits versus β for different values of η: (a) $\eta = -1.2$, (b) $\eta = -1$, (c) $\eta = -0.9$, (d) $\eta = -0.85$, (e) $\eta = -0.8$. Solid line: stable orbit, dotted line: unstable orbit, dashed line: saddle orbit, squares: saddle–node bifurcations of periodic orbits, diamonds: hopf bifurcations of periodic orbits, crosses: period doubling bifurcations of periodic orbits.

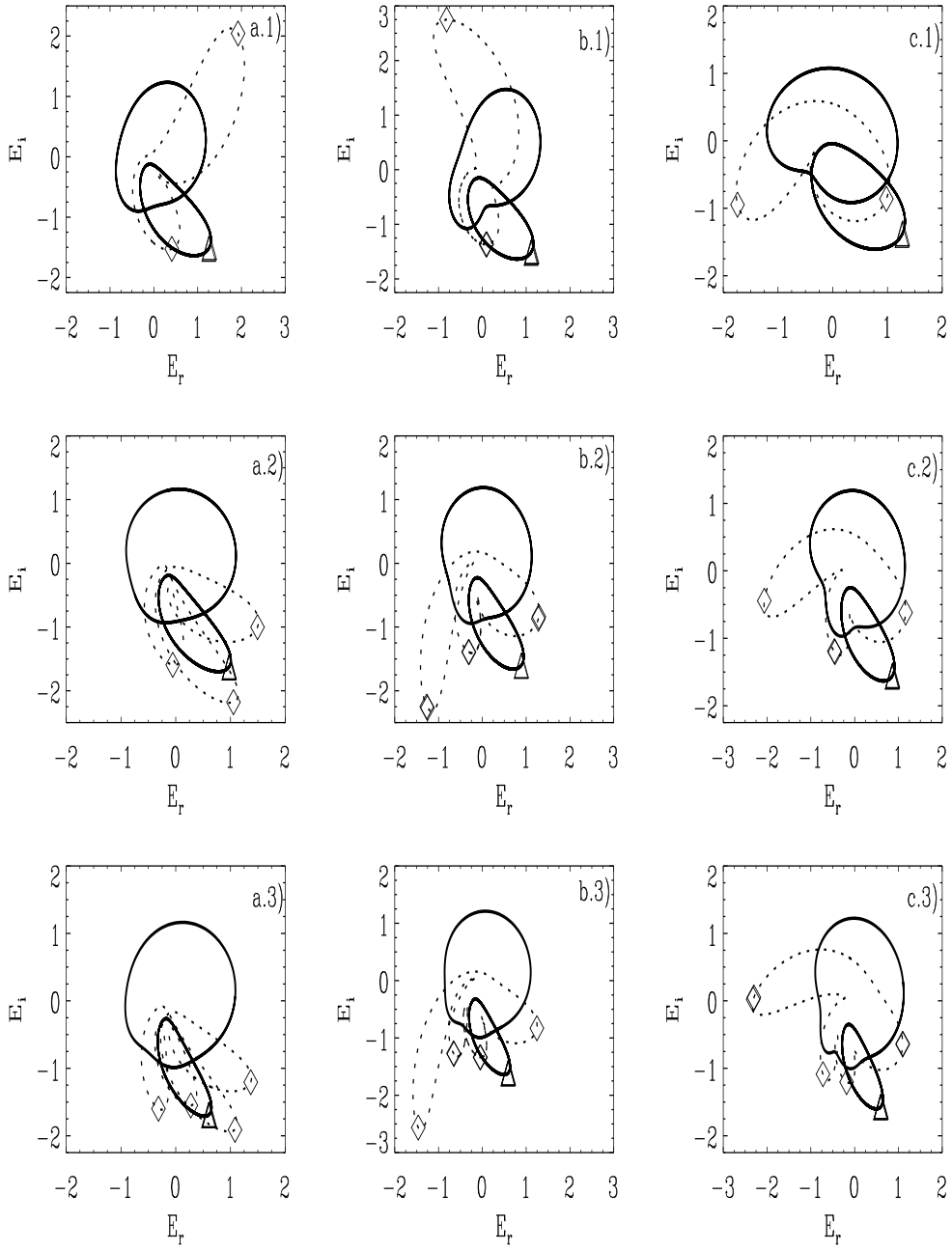

Figure 8.12: Phase portraits of resonance orbits, together with T and L. Each row shows a continuation of a transversal $1/q$ resonance on the right column, ending in a longitudinal $1/q'$ orbit on the right column. For a clear visualization only the first row displays the whole resonance orbit, while only its intersections with $W = 0$ are shown in the subsequent rows. Resonance 1/2 (η, β): (a1) $(-0.77, 0.32)$, (b1) $(-0.83, 0.40)$, (c1) $(-1, 0.41)$. Resonance 1/3: (a2) $(-0.66, 0.32)$, (b2) $(-0.70, 0.38)$, (c2) $(-0.75, 0.44)$. Resonance 1/4: (a3) $(-0.565, 0.32)$, (b3) $(-0.60, 0.38)$, (c3) $(4, -0.64, 0.43)$. Solid lines: stable orbits, dot lines: unstable trajectories. Saddle orbits are not represented.

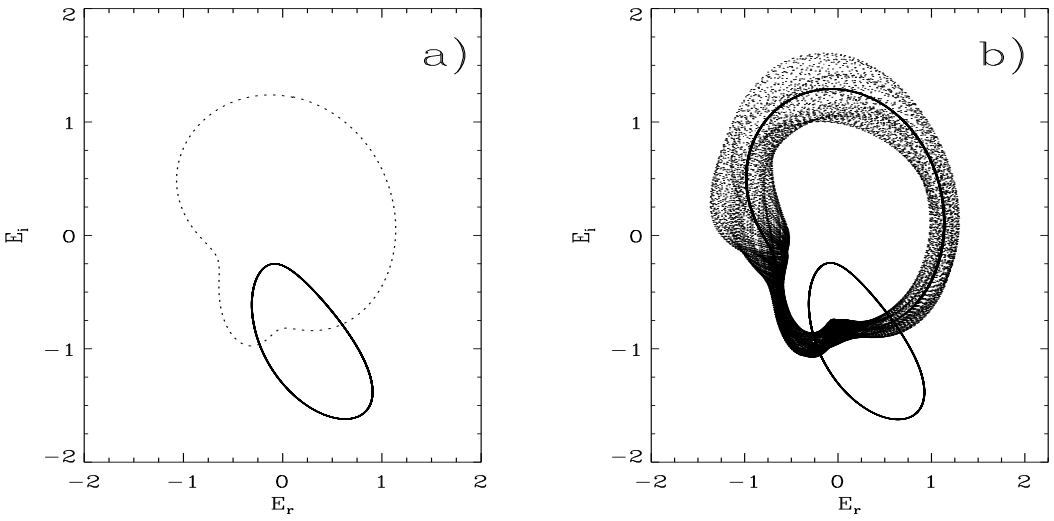

Figure 8.13: Projections in the plane (E_r, E_i) of the orbits that exist in each side of the Hopf bifurcation of L periodic orbits. Solid lines: stable orbits, dot lines: unstable trajectories. $\eta = -0.8$. (a) $\beta = 0.485$, (b) $\beta = 0.477$. The torus created is unstable.

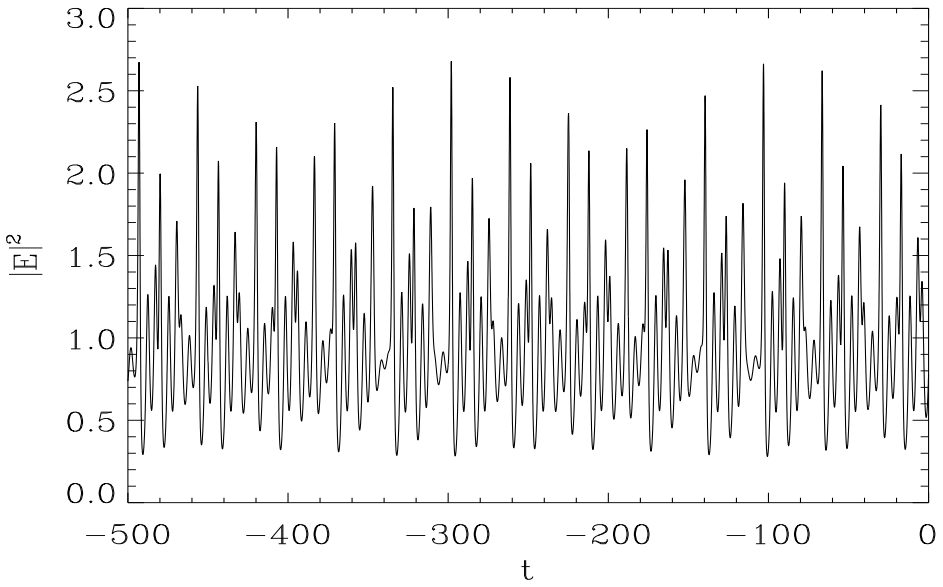

Figure 8.14: Intensity versus time for the torus created at the Hopf bifurcation of L periodic orbits. $\eta = -0.8$, $\beta = 0.477$.

do not occur on the torus. Instead the invariant torus may grow as parameters change and eventually collide with one of the resonant periodic orbits. This would correspond to a *homoclinic bifurcation* to a periodic orbit, with the final destruction of the torus.

One example may be found in the intersection point of all 1/1 resonance points with the saddle–node bifurcation of periodic orbits. At this point one may expect a Takens–Bogdanov singularity [Kuznetsov, 1997] which is well known to have such a global bifurcation. Figure 8.15 shows an enlargement of the 1/1 resonance of the transversal T and longitudinal L orbits, where the diamonds indicate the approximate values where a homoclinic tangency was observed by direct numeric computation.

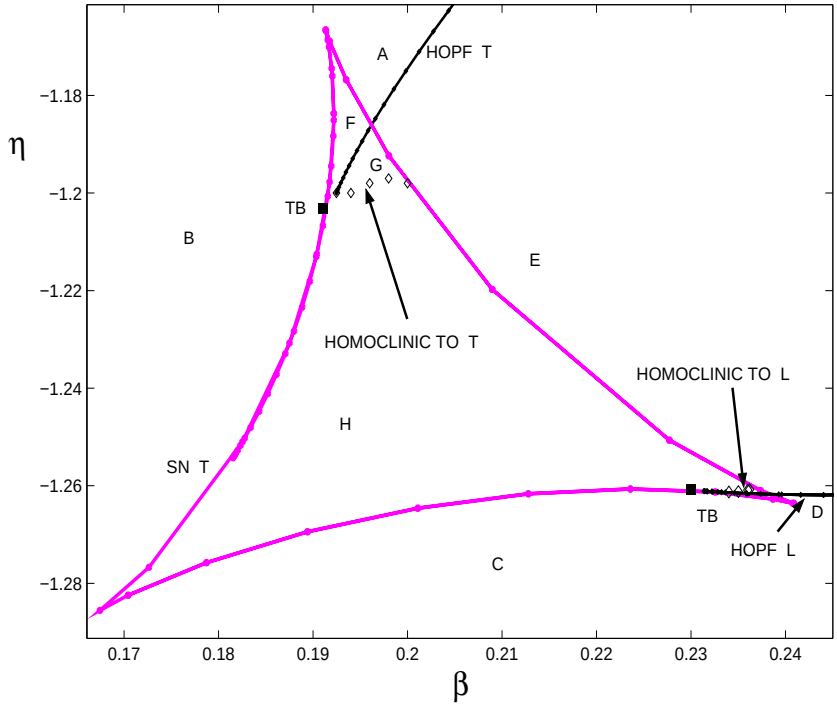

Figure 8.15: Blowup of 1/1 resonance of transversal T and longitudinal L orbits. Diamonds show the locus of homoclinic tangencies to T and L orbits.

A close loop around the Takens–Bogdanov point in Fig. 8.15 describes the main features, see Fig. 8.6 for the orbits in the parameter space. Moving from region B to F two periodic orbits are created, one saddle and one unstable. From F to G the secondary Hopf bifurcation creates an unstable torus, and the unstable periodic orbit becomes stable. In region G the radius of the torus grows as one approaches region H, and finally collides in a homoclinic bifurcation to the saddle periodic orbit. In Fig. 8.16 we illustrate a numeric computation of the stable and unstable manifold of the periodic orbit T, showing clearly a homoclinic bifurcation. Notice that one expects homoclinic tangencies as one departs from the Takens–Bogdanov point. Finally, moving from H to B, the remaining periodic orbits disappear in a saddle–node bifurcation.

An analogous scenario holds for the Takens–Bogdanov point on the longitudinal orbits seen in Fig. 8.15, denoted homoclinic to L. In general, we also find Takens–Bogdanov bifurcation points in all $1/q' = 1/1$ resonances of L described above. We emphasize that this is only an approximate view since at the Takens–Bogdanov point many other bifurcations originate (see [Hirschberg and Laing, 1995]).

A different homoclinic bifurcation to a periodic orbit is the one encountered inside the $1/3$ resonance, see Fig. 8.17. This is a well established result from the normal form analysis of this bifurcation [Arnold, 1983; Kuznetsov, 1997]. The torus is found between the secondary Hopf and the homoclinic tangency. In this case, the torus grows and collides to a saddle period $q = 3$ orbit, which exists in an neighbourhood of the T resonance point.

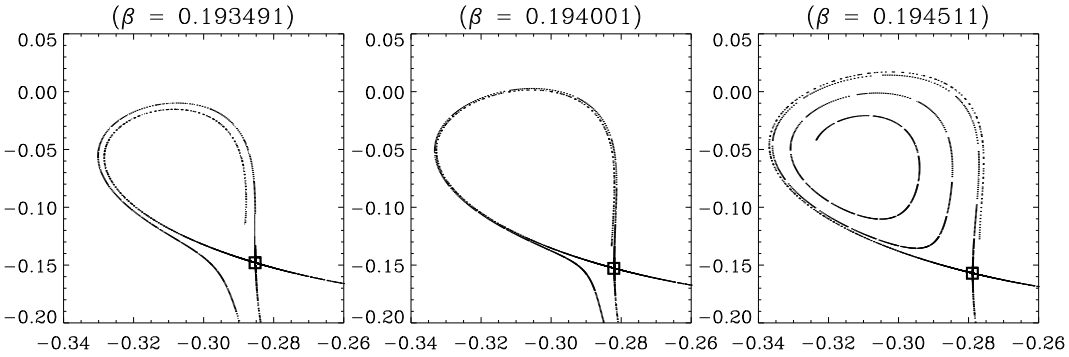

Figure 8.16: Phase portraits of the Poincaré section $W = 0$ for the homoclinic bifurcation of the $1/1$ transversal resonance, in the neighbourhood of the homoclinic tangency. The saddle periodic orbit is at the square, and next we computed the stable and unstable manifolds. ($\eta = -1.20$)

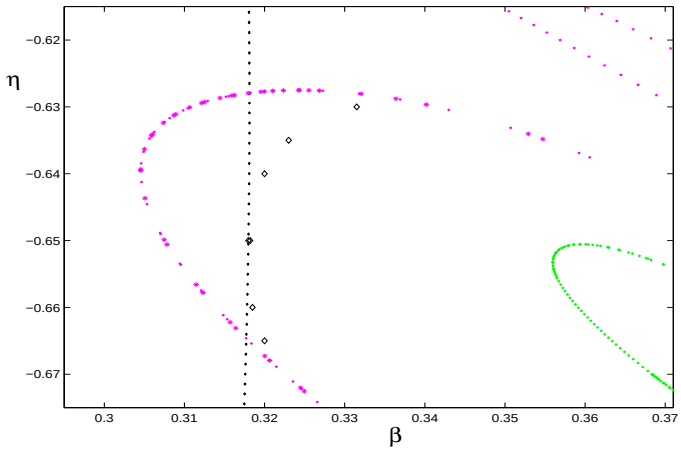

Figure 8.17: Homoclinic bifurcation in $1/3$ resonance. Diamonds account for the homoclinic to the saddle T periodic orbit.

8.2.5 Full resonance structure

In general one expects a countable number of resonances for the breakup of quasiperiodic motion, one for each rational p/q. These may be organized following the Farey sequence [Aronson *et al.*, 1982], where between resonances p/q and p'/q' one always finds resonance $(p+p')/(q+q')$. A full classification of all these resonances is quite complicated so we show the locus of two resonances with $p > 1$. In Fig. 8.18 we display two resonances in between the strong $1/1$ and $1/2$ of the transversal torus. They show basically the same structure, including the isola of homoclinic bifurcations to C and homoclinic bifurcations to the T. One of them, the transversal $5/8$ resonance, becomes a weak resonance in the neighbourhood of the L torus. The other, a transversal $2/3$ resonance becomes a strong $1/2$ resonance in the neighbourhood of the L torus. Notice also the homoclinic bifurcations to L and T periodic orbits found in this resonance.

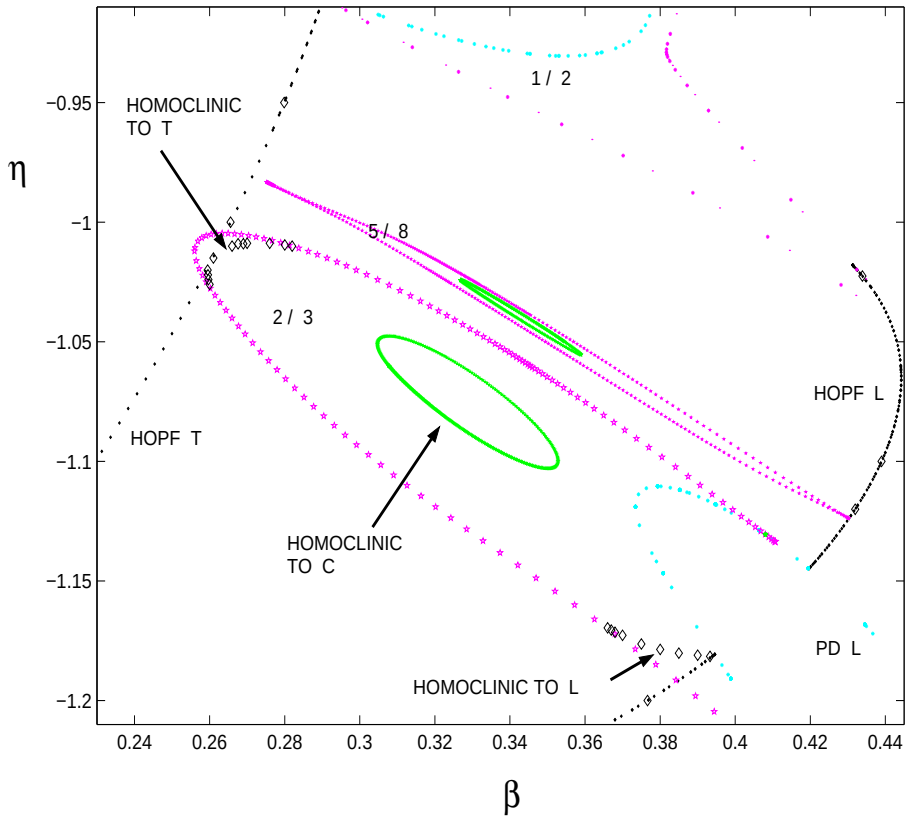

Figure 8.18: Higher order resonance structure between $1/2$ and $1/3$ transversal resonance. Transversal resonance $2/3$ becomes $1/2$ resonant to orbit L, while transversal $5/8$ resonance becomes a weak resonance to L.

8.3 Andronov bifurcation

We now describe with some more detail the Andronov bifurcation found in the laser with injected signal. In Fig. 8.19 we illustrate the phase portraits of the unfolding of this bifurcation in a one parameter cut. They correspond to the Andronov–Leontovich[3] [Kuznetsov, 1997] bifurcation: a periodic orbit in the region of no fixed point collides in a homoclinic orbit with the saddle–node (SN) fixed point. At the bifurcation point, there exists an orbit leaving the central manifold, and returning after some finite time through the other central manifold of the saddle–node fixed point.

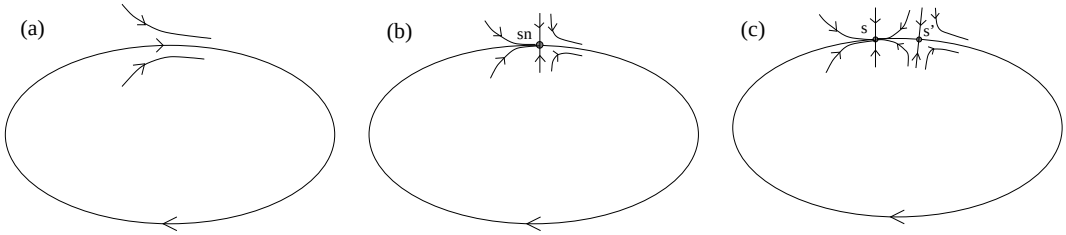

Figure 8.19: One–parameter unfolding of Andronov bifurcation. Note that the stable manifold of the fixed points in (b) and (c) are two–dimensional in a laser with injected signal.

This bifurcation is quite representative in a laser with injected signal and has been confirmed in several parameters regimes. The standard Adlers equation [van Tartwijk and Lenstra, 1995] is a one–dimensional example displaying this bifurcation. Also the two–dimensional averaged model of [Solari and Oppo, 1994], displays this bifurcation at the SN bifurcation of fixed points. This in fact motivated previous studies in global bifurcations, for in generic three–dimensional systems one expects that the global connection connecting the saddle–node to itself should break.

Results for type *III* in [Zimmermann *et al.*, 1997] show that the Andronov global bifurcation exists for sufficiently small (β, η), but become degenerate at a point close to the Hopf–saddle–node singularity, where a new codimension–2 bifurcation known as Shilnikov–saddle–node, occurs. At the bifurcation, the homoclinic orbit leaves through the central manifold the neighbourhood of the saddle–node fixed point, but now returns through the *stable* manifold of the degenerate fixed point. Results for type *I* ($1 < \theta < \sqrt{3}$) show that the Andronov bifurcation exists for the whole interval between $(\beta, \eta) = (0, 0)$ up to the Hopf–saddle–node point. However on the other side of the codimension–2 point, homoclinic tangencies to T occur near the SN bifurcation of fixed points [Zimmermann *et al.*, 2001].

For type *II* we display in Fig. 8.21 a continuation in parameter space of the Andronov bifurcation, approximated by continuation of a very high period L orbit. The locus of this global bifurcation starts at $(\beta, \eta) = (0, 0)$ and extends past the Hopf–saddle–node point. The stability of the periodic orbit depends on the stable

[3]In fact this bifurcation was studied by Andronov in 2–dimensions, while the n–dimensional case was solved by [Šil'nikov, 1966]. However we keep the term Andronov bifurcation to the generic case.

or unstable direction of the degenerate fixed point at the SN bifurcation. Therefore for $|\eta|$ small the stability of L is stable (region 3 in Fig. 8.1), while for values on the other side of the Hopf–saddle–node point, L becomes unstable (region 3′ in Fig. 8.1). In phase space, orbits born at this global bifurcation display a number of transversal oscillation ("bumps") in the region of phase space where the saddle–node fixed point (SN) disappeared. The number of these oscillations diverge as we approach from below the Hopf–saddle–node bifurcation point, for in the neighbourhood of this singular point there are *two* directions with extremely slow dynamics. Moving away from the saddle–node bifurcation, the transversal oscillations are observed to grow in phase space. We have shown in Sec. 8.2.3 how this periodic orbit is found in general to suffer saddle–node bifurcations corresponding to the resonance boundaries of the Arnold tongues, or a secondary Hopf bifurcation. This clarifies the integral role of the Andronov bifurcation in the complete bifurcation structure close to the Hopf–saddle–node bifurcation point.

A new global bifurcation was found involving the Andronov bifurcation. For sufficiently negative η, the homoclinic orbit makes a global excursion which approaches the C fixed point. In parameter space, we find that the Andronov bifurcation collides at a point with the branch of homoclinic bifurcations to C. At the collision point a heteroclinic cycle between the saddle–node (SN) and C fixed point was found. That is, there is a heteroclinic connection leaving through the central manifold of SN and enters C through the stable one–dimensional manifold, and another connection which leaves through the two–dimensional unstable manifold of C, and enters back to SN through its two–dimensional stable(–center) manifold (see Fig. 8.20). This cycle is reminiscent to the T–point bifurcations found for two *non–degenerate* fixed points [Glendinning and Sparrow, 1986; Bykov, 1993; Zimmermann and Natiello, 1998]. So far, this degenerate heteroclinic system has not been studied in detail.

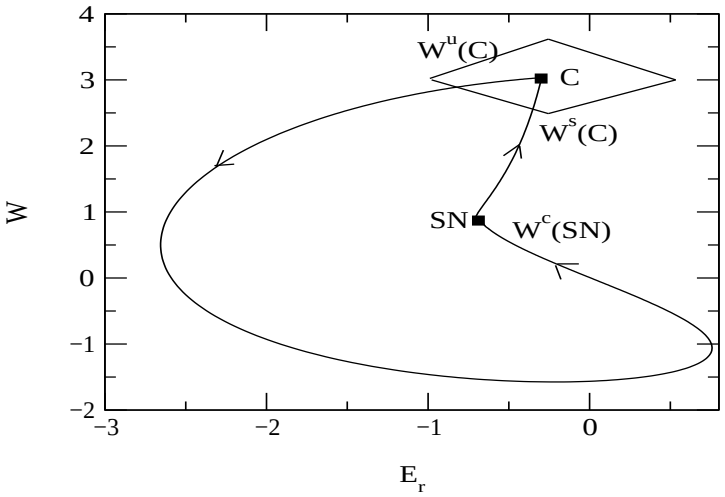

Figure 8.20: T–point bifurcation: phase portrait of heteroclinic cycle between fixed point C and saddle–node fixed point (SN) at $(\beta, \eta) = (-1.117, 0.91595)$. The stable manifold $W^s(C)$ is one–dimensional while the unstable manifold $W^u(C)$ is two–dimensional. W^c (SN) denotes the central manifold of the SN fixed point.

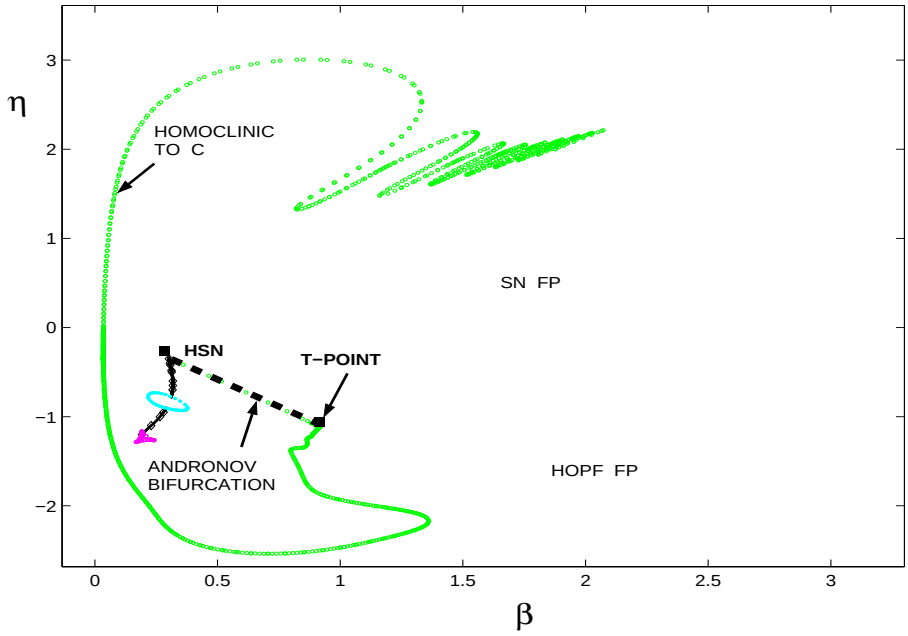

Figure 8.21: Locus of homoclinic bifurcation to C fixed point, T–point, and Andronov bifurcation at the saddle–node of fixed points.

8.4 Discussion

In this work a study of the partial bifurcation set around the type *II* regime of the Hopf–saddle–node singularity in a laser with an injected signal has been performed in order to contribute to the study of this system. It has been performed a careful analysis for one of the regimes not considered before in so detail. Secondary Hopf bifurcations to a transversal and longitudinal (to the $W = 0$ plane) periodic orbits dominate the periodic motion in a region of parameter space where non–locking solutions exists. The former periodic orbit is well described by the unfolding of the Hopf–saddle–node bifurcation, and corresponds to undamped relaxation oscillations, while the latter arises as a saddle–node infinite–period (Andronov) global bifurcation. Our results show how the Arnold tongues arising from the transversal torus are "truncated" in parameter space by resonances of the longitudinal torus. Thus in phase space the periodic orbits are observed to deform continuously from transversal into longitudinal orbits. A partial bifurcation set displaying our main result is shown in Fig. 8.22.

In chapter 6, it was described the bifurcation set for a class A laser with injected signal. The main difference between class A and class B lasers from the dynamical point of view is the number of variables that one works with. For class A lasers two variables suffice and the full bifurcation set can be described. For class B lasers, a three–dimensional system, a more complex variety of phenomena has been described. However, it has to be noticed that part of the bifurcation structure of class B lasers is already present in class A lasers. Hopf–Saddle–node and Takens–

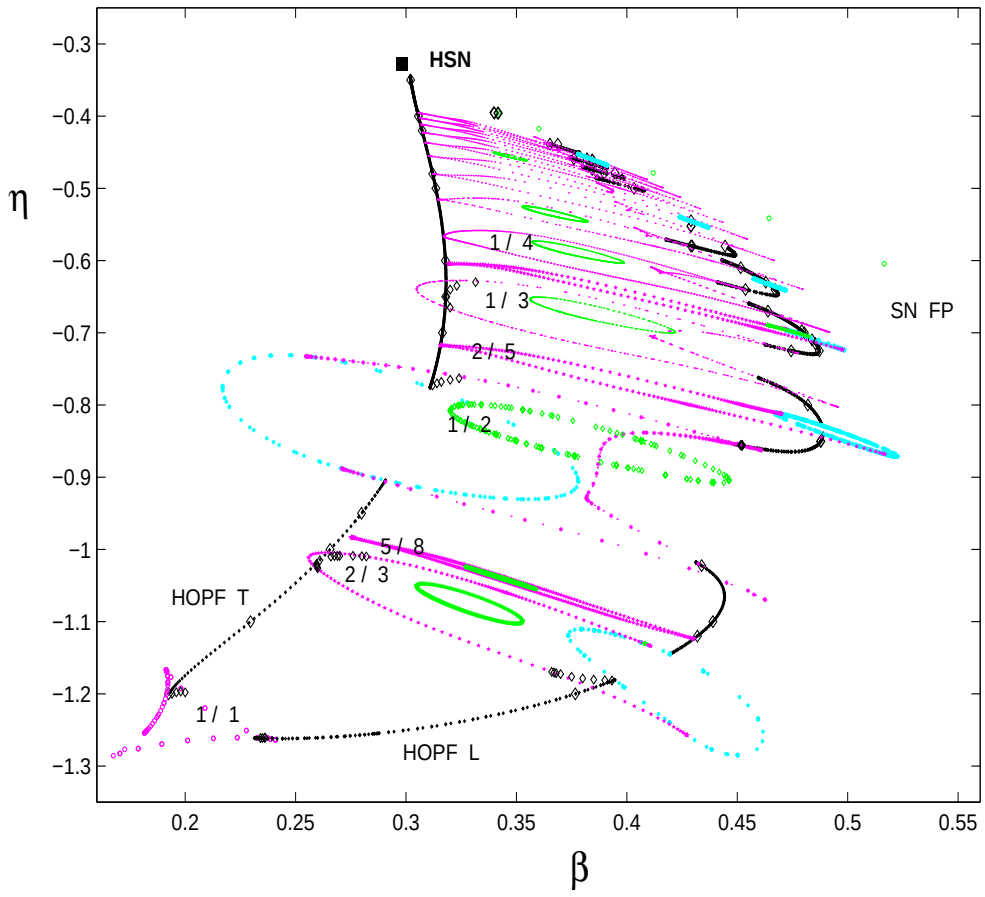

Figure 8.22: Partial numerical bifurcation set for type *II* Hopf–saddle–node in laser with injected signal.

Bogdanov singularities and Andronov global bifurcation were also present in the class *A* case.

Our work also extends [Solari and Oppo, 1994] results on the averaged laser with injected signal equations. The averaged system displays: (a) an Andronov bifurcation creating a longitudinal orbit, (b) a secondary longitudinal Hopf bifurcation on this orbit, which originates from the Hopf–saddle–node point in parameter space, and (c) the characteristic transversal secondary Hopf bifurcation of the type *II* Hopf–saddle–node singularity. However, Solari and Oppo observed as well singular behaviour (orbits going to infinity) when continuing the resulting tori in parameter space. The reason for this is the topological restriction to the deformation of transversal into longitudinal tori in a two–dimensional phase space.

In the three–dimensional setting of laser with injected signal equations we have found instead a family of homoclinic orbits to the off state fixed point, arranged in isolas in parameter space *inside each Arnold tongue* of the corresponding transversal torus. The off state fixed point appears to be at infinity in the averaged equations (due to the change of coordinates), and hence we can conjecture that the singular behaviour observed in the average model results from "bifurcations with infinity"

[Sparrow and Swinnerton-Dyer, 1995], as we move between both tori. A more detailed study of the averaged equations would be desirable to test this conjecture.

Our present work is also related to a recent work on solid–state lasers with optical injection [Yeung and Strogatz, 1998], where a complicated bifurcation diagram close to the saddle–node bifurcation was found. The rate equations studied may be shown to be rescaled to laser with injected signal equations (8.1) with $\theta = 0$ (provided that $g \neq 0$). This particular detuning was shown by Solari and Oppo to be somewhat more delicate, but type *II* Hopf–saddle–node was preserved. Yeung and Strogatz studied the attractors in a parameter cut with constant detuning η, and increasing β approaching the saddle–node bifurcation. Their diagrams showed periodic windows, interspeded by orbits with a large intensity, reminiscent of the homoclinic orbit to the off state found in our work. The most remarkable difference, is that the self–similar structure of periodic windows is reported to accumulate at the saddle–node of fixed points. Instead our work shows that (at least for $\theta = 0.5 > 0$), a *finite* number of resonances are crossed by constant–η cuts in the bifurcation diagram while approaching the saddle–node bifurcation. Nevertheless, it appears that the number of crossed resonances diverges as η approaches the codimension–2 value. Further work should confirm how the secondary Hopf bifurcation we found moves in parameter space as $\theta \to 0$.

Despite the complicated bifurcation set presented, we emphasize that most of this structure remains out of the hand of standard experimental setups due to noise terms that appear in experiments. Nevertheless we would like to point out that a partial confirmation of this bifurcation set should be possible, by following the stable *cw* solution in parameter space, and looking for stable undamped relaxation oscillations. The region of existence of these two stable invariant sets is bounded by the secondary Hopf bifurcation, and by locating the locking region, this may validate the basic features of the type *II* Hopf–saddle–node scenario.

Finally, we would like to emphasize the possible implications of the homoclinic bifurcations to the laser off state found above. The sequence of homoclinics bifurcations for each of the infinite number of resonances *accumulating* towards the Hopf–saddle–node singularity is a remarkable result which needs further detailed study. This phenomenon suggests that the Hopf–saddle–node singularity may have, on top of the saddle–node infinite–period global bifurcation, another pair of heteroclinic orbits to the Hopf–saddle–node fixed point, forming a cycle. So far, we are no longer surprised by the bizarre global bifurcations found in this laser, which provide stimulating motivation for further research.

Capítol 9

Resonàncies principals en làsers de semiconductor modulats

En aquest capítol es calculen els dominis d'existència de les resonàncies principals en làsers de semiconductor directament modulats, veure Sec. 1.3. Els resultats que s'obtenen numèricament al integrar directament les equacions es comparen amb els resultats d'aplicar la teoria quasi–conservativa. En el model es consideren explícitament els termes de saturació de guany i d'emissió espontània.

Les equacions per al làser de semiconductor (9.1) i (9.2) es tracten amb termes de modulació. Primerament es consideren modulacions en el terme de bombeig de tipus sinusoidal (9.3) amb amplitud relativa J_m i freqüència ω_m. La dinàmica de les equacions amb aquesta dimensió addicional esdevé molt més complexa que en el cas de bombeig constant (capítol 7). Per caracteritzar la resposta del sistema es mira el valor màxim de la intensitat òptica I, (I_{max}), quan es modula el làser. Per a valors petits de J_m i ω_m, el sistema es comporta de manera similar a un oscil·lador lineal amb termes d'esmorteïment: oscil·la periòdicament amb la freqüència d'entrada ω_m, i la resposta I_{max} té un màxim a la freqüència de les oscil·lacions de relaxació ω_0. Per a valors grans d'amplitud, apareixen efectes no lineals importants. El màxim de I_{max} ja es no troba a ω_0 sinó que desplaçat cap a una freqüència menor, Fig. 9.1. A més d'aquesta resposta amb la mateixa freqüència de modulació $1T$, també poden aparèixer altres respostes amb altres freqüències. Això dóna lloc a un comportament molt complex amb regions amb multiestabilitat. Les possibles respostes es poden classificar com n/l, on n i l són nombres sensers sense factors comuns, de manera que la resposta té una freqüència $l\,\omega_m/n$. Les respostes $n/1$ també s'anomenen nT atès que el període del senyal resultant és n vegades el període del senyal de modulació. L'existència d'aquestes respostes es veu a la Fig. 9.1, on s'ha dibuixat I_{max} de les respostes estables en funció de ω_m. Anant augmentant el valor de J_m, es veu com van apareixen les distintes respostes nT. A la figura 9.2 apareixen les evolucions temporals per a distints valors de ω_m per a les respostes $1T$ i $2T$. A més d'aquesta estructura bàsica, cadascuna de les respostes poden, així mateix sofrir bifurcacions de període doble, Fig. 9.1 (d), i en qualque cas

donar lloc a comportament caòtic. Cada resposta n/l té un màxim, en ω_m, per a un valor fixat de J_m: aquest màxim és la *resonància* n/l. En aquest treball ens centram en les resonàncies nT, que s'anomenen *resonàncies principals* o resonàncies primeres sella–node ja que coincideixen amb les bifurcacions sella–node on l'òrbita estable esdevé inestable (Fig. 9.1). Les corbes al pla $(\omega_m/\omega_0, J_m)$ que uneixen els punts de les resonàncies nT s'anomenen corbes "esquelet" per a la resonància nT. L'objectiu d'aquest treball és obtenir les corbes esquelet per a les resonàncies nT, Fig. 9.3. Aquesta descripció és d'interès per a treballs experimentals perquè permet determinar la freqüència en la qual es té una resposta màxima per a una amplitud d'injecció fixada. Els resultats obtinguts han ajustat amb els resultats indicats en treballs experimentals [Liu and Ngai, 1993]. El terme de saturació de guany no canvia el comportament dinàmic ni la localització de les corbes esquelet de manera qualitativa, Fig. 9.4. Per a un valor fixat de ω_m, cal un valor més gran de J_m per obtenir la resposta òptima, compatible amb què aquest terme augmenta la dissipació. El terme d'emissió espontània canvia dràsticament el comportament de la dinàmica del sistema per a valors de ω_m petits, Figs. 9.5 i 9.6. Aquest efecte pot ser causa d'un fons de fotons que evita que la intensitat del camp elèctric disminueixi per davall d'un cert valor, donant lloc a una resposta independent de la freqüència.

Els resultats obtinguts numèricament es poden explicar mitjançant la teoria quasi–conservativa. Aquesta teoria, que utilitza la forma potencial per al sistema obtinguda en el capítol 7, assumeix que les òrbites periòdiques es poden aproximar, a prop de la resonància, per òrbites conservatives amb un valor del potencial. Els resultats de la figura 9.7 indiquen que la teoria reprodueix els resultats numèrics en el cas de tenir un terme d'emissió espontània nul. En presència de termes d'emissió espontània, la predicció teòrica reprodueix qualitativament els resultats numèrics, Figs. 9.8 i 9.9. No obstant, la teoria prediu un augment molt més acusat per a l'amplitud òptima de modulació que l'obtinguda numèricament, a causa de la forma del període de les solucions conservatives en funció de l'energia per a valors grans de l'energia.

El cas de modulació al terme de pèrdues també s'estudia. Els resultats de la teoria quasi–conservativa ajusten bastant bé amb els resultats numèrics, Figs. 9.10, 9.11 i 9.12.

Finalment, s'obté en una relació entre l'efecte produït per la modulació al bombeig i la modulació al terme de pèrdues, (9.29). La validesa d'aquesta equivalència apareix en les figures 9.13 i 9.14. Aquesta relació indica que la modulació al terme de pèrdues és més eficient a l'hora de tenir bifurcacions i comportament caòtic que la modulació al bombeig (cal un valor de l'amplitud de modulació, en el cas de les pèrdues, molt menor que en el cas de la modulació al bombeig, per obtenir els mateixos efectes).

Chapter 9

Main resonances in directly modulated semiconductor lasers

In this chapter, we undertake numerical and analytical calculations in the framework of the single mode rate equation model (chapter 4) including a modulation term for the injection current with the aim of determining the parameter domains of the basic instabilities involved. The work presented in this chapter completes the above series of studies of directly modulated semiconductor lasers, as it was reviewed in section 1.3.

Domains of existence of the main resonances in directly modulated semiconductor lasers are obtained by application of the quasi–conservative theory. The predictions are compared with numerical results coming from a direct integration of the model equations and with experimental observations reported by other groups. In both cases we find a good qualitative agreement. We consider a model that contains explicitly the gain saturation and spontaneous emission terms and we focus mainly on the effect that these terms have in the regime of large amplitude of modulation.

The chapter is organized as follows. In section 9.1, we describe qualitatively the response obtained for a diode laser, as described by a single–mode rate equation model, in the presence of pump modulation. In Sec. 9.2, the quasi–conservative theory is used to obtain relations that allow the calculation of the primary saddle–node bifurcations, both for the case of modulation in the pump or in the losses. In Sec. 9.3, the theoretical estimations are compared with numerical results coming from a direct integration of the model equations. The effects of gain saturation and spontaneous emission terms in these bifurcations are explored in detail. In Sec. 9.4, we compare our results to previous experimental works reported by other groups. Finally, in Sec. 9.5, we discuss the main obtained results.

9.1 Dynamical behaviour

The dynamics of a single mode semiconductor laser was discussed in detail in chapter 7. As the evolution equations for I and N do not depend on the phase ϕ, we can concentrate only in the evolution of the former variables. The equations that

give the corresponding dynamics are equations (7.1) and (7.3):

$$\frac{dI}{dt} = \left[g_N \frac{(N - N_o)}{1 + s\,I} - \gamma \right] I + 4\,\varepsilon\,N, \tag{9.1}$$

$$\frac{dN}{dt} = \frac{J}{e} - \gamma_N\,N - g_N \frac{(N - N_o)}{1 + s\,I}\,I. \tag{9.2}$$

Typical values of the parameters involved in the equations were presented in Table 7.1. The dynamics of the equations for constant $J > J_{th}$ is such that both I and N relax to their steady states by performing damped oscillations. The frequency ω_0 of these oscillations close to the steady state can be calculated linearizing the equations of motion (7.35), for the simplest case $s = \varepsilon = 0$, $\omega_0 \approx \sqrt{g_N(J - J_{th})/e} = 25\text{ns}^{-1}$ for parameter values of Table 7.1 and $J = 1.23 J_{th}$.

The purpose of this work is to study the dynamics of Eqs. (9.1) and (9.2) under modulation. In particular, we will consider modulations mainly in the pump current J and also in the losses γ, which would be an option in distributed Bragg reflection or multisection lasers. In order to be more specific, we describe now the qualitative features of the behaviour when the pump is modulated at a given frequency ω_m. More explicitly, we consider

$$J(t) = J_b[1 + J_m \cos(\omega_m t)], \tag{9.3}$$

where J_b is a fixed value of the current (bias current), such that $J_b > J_{th}$. In our simulations we choose $J_b = 1.23 J_{th}$ and values for the relative amplitude of the modulation $J_m < 1$ (to satisfy the physical constraint that the total current has to be positive). When J becomes time dependent, the dynamics are more complex than in the case of constant J, and a very rich dynamical structure can appear depending on the values of J_m and ω_m.

For small values of J_m and for ω_m smaller than $-3dB$ modulation bandwidth frequency, the system behaves almost as a forced linear oscillator with damping terms; the optical intensity I oscillates periodically with the same frequency ω_m of the input current. To characterize the response of the system we look at the maximum value of I (I_{max}) when we modulate the laser. It is well known that, under small signal modulation, the optical response I_{max} has a maximum at the relaxation oscillation frequency ω_0 [dotted line of Fig. 9.1 (a)]. This is an example of the well known phenomenon of linear resonance [Agrawal and Dutta, 1986; Jackson, 1989].

In contrast to the small signal response just described, large amplitude modulation, i.e. large values of J_m, give rise to strong nonlinear behaviours, since the nonlinear terms become relevant in the dynamics of the system. The maximum response (maximum value of I_{max}) is not located anymore at the relaxation oscillation frequency ω_0 but it is shifted to a smaller frequency (*soft* spring oscillator)[1]. This fact can be seen in Fig. 9.1 where the response of the system, for different values of J_m, is shown. In this case we have taken $s = 0$ and $\varepsilon = 0$ in Eqs. (9.1) and (9.2). In

[1]The nonlinear terms of *hard* spring oscillators make the maximum response to be shifted to a bigger frequency than ω_0.

this nonlinear regime, in addition to a response at the same frequency of modulation ω_m, other frequencies can be excited for sufficiently high modulation amplitudes J_m. This fact gives rise to a more complex diagram for the response of the system, leading even to the phenomenon of multistability (several stable responses for the same value of the input parameters). The different possible responses of the system can be classified as n/l where n and l are integer numbers with no common factors, such that the response frequency is $l\omega_m/n$ [Jackson, 1989].

In this work, we will be mainly interested in primary resonances of the type $n/1$. Our interest in these responses is based on the fact that they usually yield the maximum output power. These $n/1$ resonances are also called nT–periodic responses because the period of the resulting signal is n times larger that T_m, where $T_m = 2\pi/\omega_m$ is the period of the external modulation. Different types of stable n/l responses (amplitude I_{max} versus the modulation frequency ω_m) are shown in Fig. 9.1 for different values of the modulation amplitude J_m; while in Fig. 9.2, the time evolution for the intensity is plotted for different values of the frequency ω_m and the common value $J_m = 0.2$. The qualitative picture described is now detailed:

- For small modulation amplitude, see Fig. 9.1 (a) ($J_m = 0.01$, dotted line), the linear approximation applies and there are only single main resonances whose maximum lies approximately at the relaxation frequency.

- For larger modulation amplitudes, Fig. 9.1 (b), the stable $1T$ resonances destabilize themselves via a saddle–node type instability. This allows a hysteresis cycle with discontinuous transitions between the different $1T$ responses. This saddle–node instability is interesting since we have observed that the maximum response appears just before the solution becomes unstable. (We will come back to this point later). When multistability is possible, and for those moderate levels of the amplitude of the modulation, the larger output intensity I_{max} always corresponds to the $1T$ response. Other n/l responses, with $l \neq 1$ can be generated for small frequencies but they have a much smaller output power and they will not be considered in this work.

- After a further increase of J_m (Fig. 9.1 (c), corresponding to $J_m = 0.2$) the $2T$ response appears continuously, when decreasing ω_m (starting, in our example, from $\omega_m/\omega_0 = 3.0$), as a period doubling bifurcation of the $1T$ response (see Fig. 9.2 for temporal trajectories). When ω_m is decreased even further, there appears a range of values of ω_m for which the $1T$ and $2T$ responses are both stable, hence allowing a hysteresis cycle in this bistable region as well as a discontinuous transition between the $1T$ and the $2T$ responses. The $1T$ response, solid line, gives a smaller output that the $2T$ response for the whole frequency range of existence of the $2T$ response, namely for $\omega_m/\omega_0 \in [0.968, 2.118]$. The $1T$ response does not exist (is unstable) in the frequency interval $[1.761, 2.118]$. For even smaller ω_m the $2T$ response finally disappears through a saddle–node instability. The $2T$ response around $\omega_m/\omega_0 \approx 2.0$ is the first subharmonic resonance (parametric resonance [Jackson, 1989]).

- For larger values of J_m [Fig. 9.1(d)] other nT responses with $n > 2$ appear. Each of these nT responses exist for a given range of values of ω_m and are unconnected to the previous $1T$ and $2T$ responses. At both ends of its frequency range, they disappear through saddle–node bifurcations.

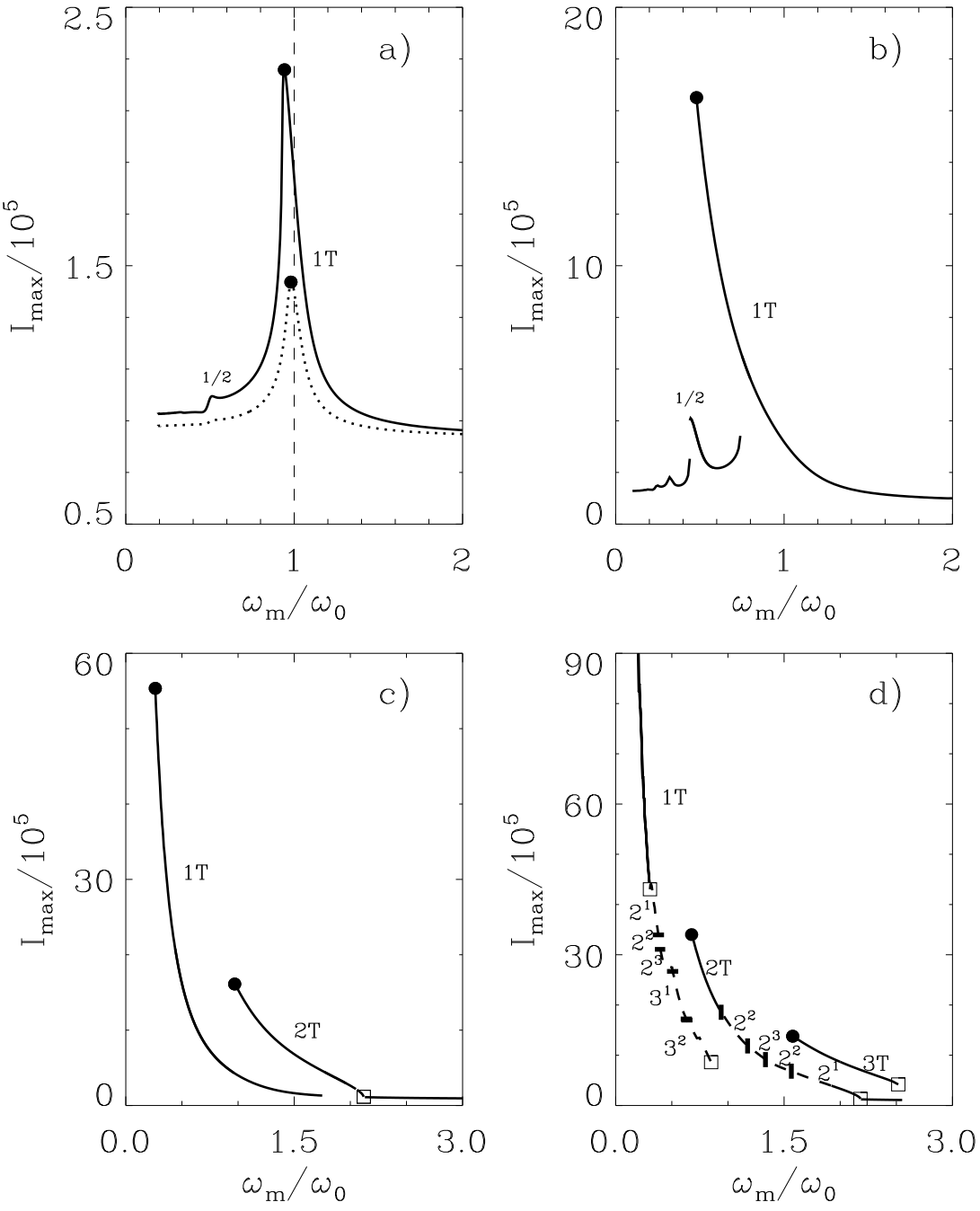

Figure 9.1: Responses, I_{max}, versus the normalized external frequency ω_m/ω_0 for different values of the modulation pump amplitude in the case $J_b = 1.23J_{th}$, $s = 0$, $\varepsilon = 0$. Other parameters as indicated in the text. (a) dotted line: $J_m = 0.01$, solid line: $J_m = 0.02$, (b) $J_m = 0.1$, (c) $J_m = 0.2$ and d) $J_m = 0.3$. The 2^k and 3^k responses correspond to further period doubling bifurcations.

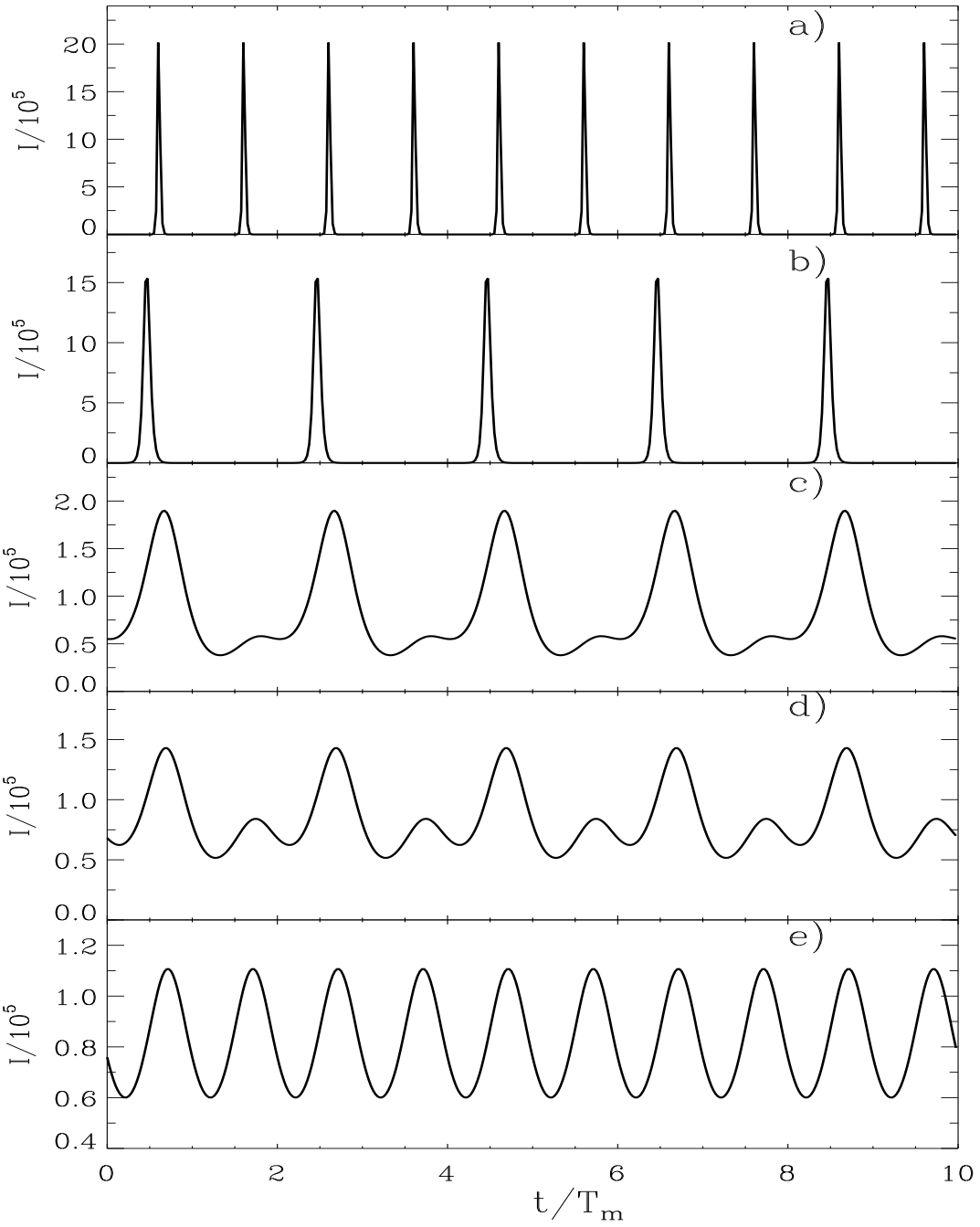

Figure 9.2: Intensity versus time for different values of ω_m/ω_0 for $J_m = 0.2$ corresponding to some points of the curve of Fig. 9.1 (c). (a) $\omega_m/\omega_0 = 0.43$, (b) $\omega_m/\omega_0 = 0.97$, (c) $\omega_m/\omega_0 = 2.08$, (d) $\omega_m/\omega_0 = 2.11$, (e) $\omega_m/\omega_0 = 2.12$. Same parameters as in Fig. 9.1. $T_m = 2\pi/\omega_m$.

Besides this general framework, all the existing nT responses can, at a given value of the modulation amplitude, suffer different types of period doubling bifurcation, period four, etc, or even chaos, following the Feigenbaum route to chaos [Jackson, 1989] or the route period doubling followed by period four, eight, period tripling, etc., as in references [Lamela *et al.*, 1998b; Lamela *et al.*, 1998a]. These are indicated with dashed lines in the corresponding diagram [Fig. 9.1 (d)] and are denoted as 2^k responses, being k an indication of the number of period doubling bifurcation that the orbit has suffered. The same meaning applies for the 3^k responses.

In Fig. 9.2 we plot, for a fixed value of the modulation amplitude [$J_m = 0.2$, corresponding to the diagram in Fig. 9.1 (c)], time evolutions for the intensity $I(t)$ for several values of the frequency ω_m/ω_0. Case (a) corresponds to $\omega_m/\omega_0 = 0.43$ where, according to Fig. 9.1 (c), the $1T$ type solution with maximum intensity appears. Case (b) corresponds to a frequency $\omega_m/\omega_0 = 0.97$ where the $2T$ solution begins to exist. We note that at this frequency, the $2T$ signal has a maximum spectral component in the first harmonic, allowing for a clean time trace of the optical intensity, with no additional peaks, as shown in Fig. 9.2 (b). As the frequency increases, Figs. 9.2 (c) and 9.2 (d), the $2T$ response deteriorates in the sense that the maximum intensity decreases and extra peaks develop in the time series. Finally, for $\omega_m/\omega_0 = 2.12$ the $1T$ response is recovered. However, and in accordance with Fig. 9.1 (c), the maximum intensity is now much smaller that the one of the optimal $1T$ response shown in Fig. 9.2 (a).

For fixed modulation amplitude J_m, each n/l response has its maximum at a given value of the modulation frequency. This maximum is called the n/l resonance. In this work, we are mainly interested in the $n/1$ resonances (or nT resonances) because they usually yield the maximum output power. In the literature, they are also known as *main resonances*. These resonances are indicated by solid dot symbols in Fig. 9.1. The curves in the $(\omega_m/\omega_0, J_m)$ plane joining the points at which nT resonances occur are called the *skeleton* curves for the nT resonances. Our main effort will be directed to finding the skeleton lines for each main resonance of the nT type. This description can be of interest to the experimentalists since it allows determination of the resonance frequency at which the maximum response is obtained for a given external amplitude of the injection current.

With this aim in mind, we have performed intensive numerical simulations to obtain the maximum responses of the system for different J_m and ω_m/ω_0. In principle, for a given J_m, one should find the value of ω_m/ω_0 that maximizes the response at each nT resonance. However, this is a very lengthy procedure that can be avoided by finding, instead, the value of ω_m/ω_0 where a saddle–node bifurcation is born, since, as we have already said, we have observed that the maximum response appears just before the solution becomes unstable. Due to this fact the main resonances are also called *primary saddle–node resonances*. This allows us to identify the position of the maximum response in the $(\omega_m/\omega_0, J_m)$ plane with the position of the bifurcation. The procedure of finding such bifurcation is easier to implement using nonlinear dynamical tools than to perform whole simulations of the rate equations [Doedel *et al.*, 1997].

In Fig. 9.3 the primary saddle–node bifurcation are shown (thick solid lines) in the case $s = 0$ and $\varepsilon = 0$ for the $1T$, $2T$ and $3T$ resonances. We show in some cases that the location of the saddle–node bifurcation coincides, with great accuracy, with that of the maximum I_{max}. The latter have been obtained by numerical simulations of the laser equations and are indicated by symbols in the figure. Notice, however, that the line of the saddle–node bifurcation do not reach the linear limit $\omega_m/\omega_0 = 1$ corresponding to very low amplitude of the modulation, because for small values of modulation amplitude there is no saddle–node bifurcation. We also plot in the same figure some additional lines that correspond to domains of existence of the above mentioned nT resonances. Within these domains, besides the "pure" nT solutions, there exist a rich variety of bifurcated solutions (period doubling, period 4, and so on, indicating the route to chaos described previously). The $1T$ solution only exists below the thin solid line of Fig. 9.3. The $2T$ solution is limited to the region below the thick solid line of $2T$ and the dashed line and it only exists within this limit. Finally, the $3T$ solution is limited to the region below the thick solid line of $3T$ and the dot–dashed line of the figure. In what follows, we will restrict ourselves to the thick lines denoting the maximum of each resonance.

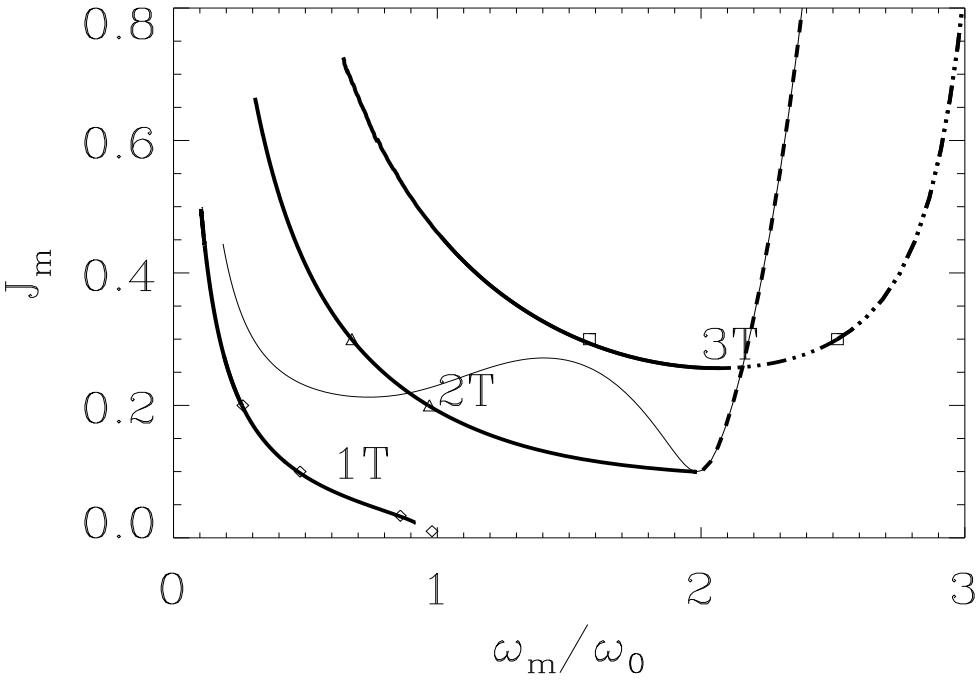

Figure 9.3: Maxima of main resonances in the plane $(\omega_m/\omega_0, J_m)$, solid thick lines. Thin solid line: Period doubling bifurcation of the $1T$ resonance to 2^1 (coincides with the limit of existence of resonance $1T$), dashed line: lowest limit for the existence of the $2T$ resonance, dot–dashed line: lowest limit for the existence of the $3T$ resonance.

We now describe the effect of the gain saturation term. We plot in Fig. 9.4, the changes on the line of main resonances (given in Fig. 9.3 for $s = \varepsilon = 0$) in the case $s \neq 0$ (but still $\varepsilon = 0$). It can be seen clearly that the saturation term does not change qualitatively, neither the location of the lines nor the overall dynamical behaviour of the system. The only difference is that, for a fixed frequency, a larger value of J_m is needed to obtain the optimal periodic response. This is clearly compatible with the fact that the main effect of the saturation term is to increase the dissipation.

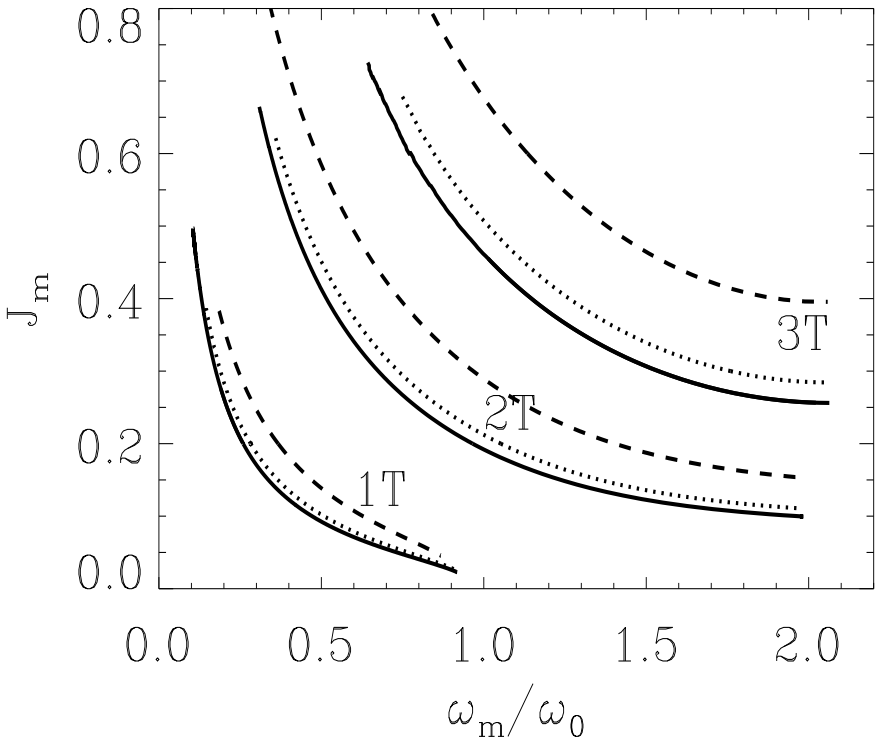

Figure 9.4: Maxima of main resonances in the plane $(\omega_m/\omega_0, J_m)$. Solid line: $s = 0$, dotted line: $s = 6 \times 10^{-9}$, dashed line: $s = 3 \times 10^{-8}$. $\varepsilon = 0$. Other parameters as in Fig. 9.1.

On the contrary, the effect of the spontaneous emission term strongly changes the response of the system. In Fig. 9.5, the lines of I_{max} in the $(\omega_m/\omega_0, J_m)$ plane are shown for the case $\varepsilon \neq 0$ and $s = 0$. One can observe the dramatic change in the behaviour of the response of the system for small frequencies with respect to that observed for $\varepsilon = 0$ (solid line). When increasing the modulation amplitude we find a steep response that indicates that the frequency ω_m for the optimal response I_{max} is less sensitive to the amplitude of the external modulation, J_m. We speculate that this effect might be due to that for $\varepsilon \neq 0$ there is a background of photons preventing the intensity decreasing below a certain value, so yielding a frequency–independent response. For the case $s \neq 0$ and $\varepsilon \neq 0$ we observe combined the same qualitative results as those shown in Fig. 9.4 and Fig. 9.5. It is important to point out that values of s and ε different from zero yield chaos suppression, a fact that has been already pointed out both numerically and experimentally [Tang and Wang, 1987]. Naively, one could expect that the gain saturation parameter plays a more important part in the dynamics. However, we observe that in some situations the main resonances can be affected more strongly by the spontaneous emission factor than by the gain saturation factor.

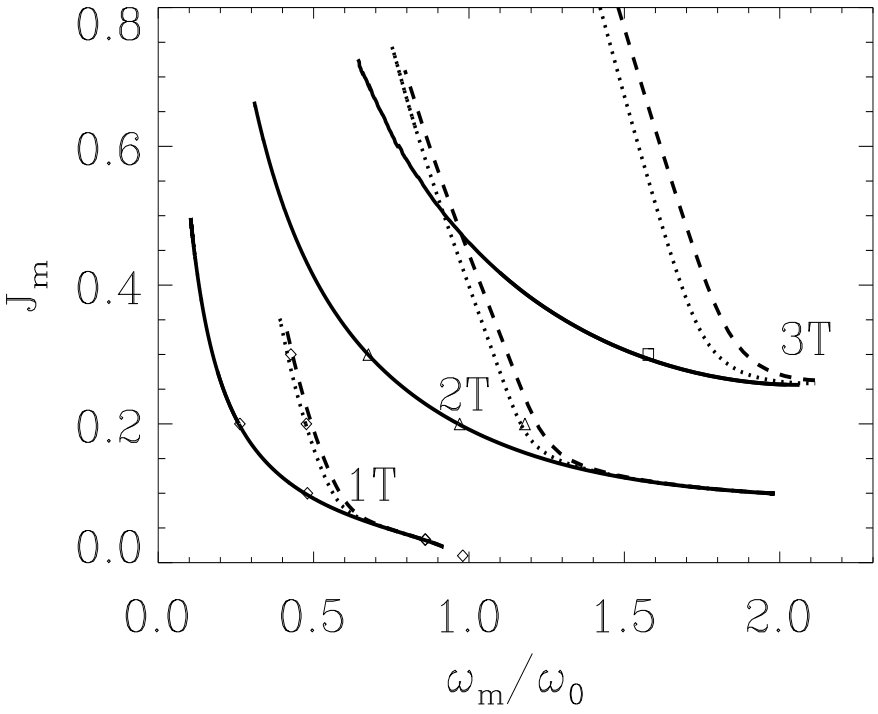

Figure 9.5: Maxima of main resonances in the plane $(\omega_m/\omega_0, J_m)$. Solid line: $\varepsilon = 0$, dotted line: $\varepsilon = 6.2 \times 10^{-11} ps^{-1}$, $\varepsilon = 2.3 \times 10^{-10} ps^{-1}$.

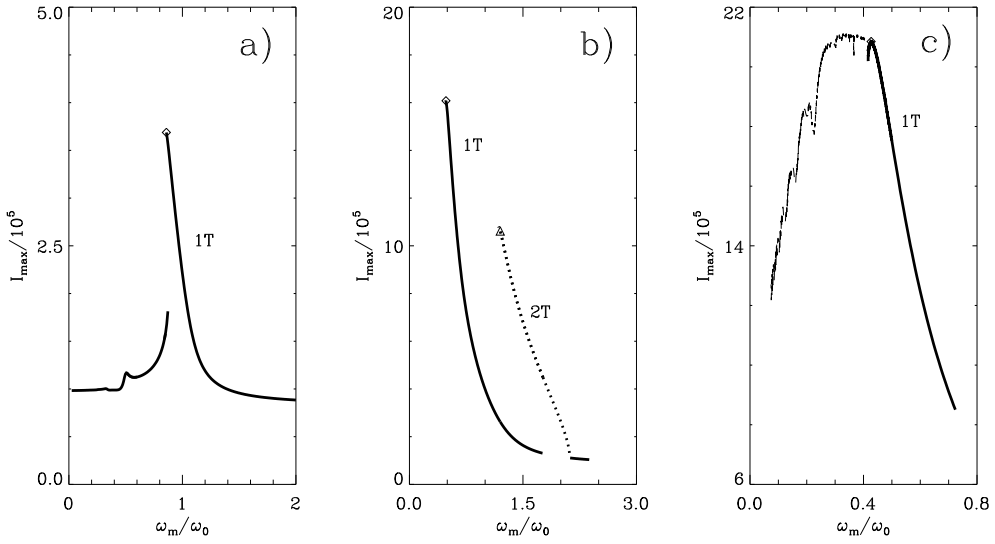

Figure 9.6: Responses, I_{max}, versus the normalized external frequency ω_m/ω_0 for different values of the modulation amplitude. $J_b = 1.23 J_{th}$. $s = 0$, $\varepsilon = 6.2 \times 10^{-11} ps^{-1}$. Other parameters as indicated in the text. (a) $J_m = 0.033$, (b) $J_m = 0.2$ and (c) $J_m = 0.3$.

In the absence of spontaneous emission, $\varepsilon = 0$, the tendency to decrease the main resonance frequency with increasing amplitude of modulation can be explained using a Toda–like potential function (7.14). Physically, it means that a maximum number of photons in the cavity is available for modulation and this number is not limited from below. However, in the presence of spontaneous emission terms, this is not true anymore and the Toda potential as a function of the intensity changes, becoming more symmetric and steeper for very low intensities. A spontaneous emission background is created and during the modulation period the number of photons can not be smaller than this value and, consequently, the response is maintained basically unchanged at any smaller frequency. As soon as the intensity of the laser reaches this background level, the dynamics changes and at low frequencies a non–resonant regime of gain switching (with no dependence on frequency in some modulation frequency interval observed) dominates. In Fig. 9.6, we plot the maxima intensity responses I_{max} against frequency ω_m for different values of J_m, in the case $\varepsilon \neq 0$. Compared with Fig. 9.1, we notice that at small modulation amplitude [$J_m = 0.033$, Fig. 9.6 (a)] the response for small value of ω_m does not change qualitatively and very little quantitative with respect to that of Fig. 9.1 (a). However, for large values of J_m, the effect of ε becomes more evident. At $J_m = 0.2$ [Fig. 9.6 (b)] the

maximum response for the resonance $1T$ is now at a larger frequency than in Fig. 9.1 (c) and, moreover, the corresponding value of I_{max} is much smaller. Increasing J_m even further [$J_m = 0.3$ in Fig. 9.6 (c)], we find that the maximum response for the resonance $1T$ (thick line) is much smaller than in the case of Fig. 9.1 (d), and corresponds to a much larger frequency. It has to be mentioned that in this case, the value of ω_m/ω_0 that maximizes the $1T$ response presents larger differences with the location of the saddle–node than in previous cases [Notice the difference between the maximum and the end of the solid line in Fig. 9.6 (c)]. In Fig. 9.6 (c) we also plot other responses for smallest values of ω_m. These responses, while having a larger output than the $1T$ responses, can either have a period larger than $1T$ or, while still being $1T$, have extra peaks in the time series. They include responses of period $1T$, $2T$, ..., being an example of the structure also reported in [Tang and Wang, 1986]. We also point out that there exists an almost flat response for some range of values of ω_m/ω_0.

9.2 Quasi–conservative theory

Equations (7.1, 7.3) [or equivalently Eqs. (9.1, 9.2)] were reduced to a set of dimensionless equations in chapter 7. These evolution equations can be cast in the form of a *potential* function (7.14) with the relating matrix D (7.17) to the equations of motion (2.26). The decrease of the Lyapunov potential is due to the function $D_{22}(y,z)$ (7.19) appearing in the evolution equation. Therefore, in the dynamical equations we can identify the conservative terms (those proportional to D_{12}) and the dissipative terms (those proportional to D_{22}). If the dissipative terms were not present, i.e. if $D_{22} = 0$, the potential would take a constant value $E = V(y,z)$ and we would have a conservative system with periodic orbits. The frequency $\omega = 2\pi/T$ (T is the corresponding period) of such an orbit of the conservative system is a function of the potential, i.e. $\omega = \omega(E)$, that can be obtained, using standard methods of Mechanics (7.26). Notice that the periodic orbits, that we write as $[y_0(\tau - \tau_0, E), z_0(\tau - \tau_0, E)]$, depend on an initial time τ_0 and on the value of the Lyapunov potential E.

9.2.1 Pump Modulation

We now include the modulation terms. We first consider the case of modulation in the pump as given in (9.3). In terms of the rescaled variables, y and z [related to the initial variables by (7.5)], the equations become

$$\frac{dy}{d\tau} = D_{12}\frac{\partial V}{\partial z}, \tag{9.4}$$

$$\frac{dz}{d\tau} = -D_{12}\frac{\partial V}{\partial y} - D_{22}\frac{\partial V}{\partial z} + A_m \cos(\bar{\omega}_m \tau), \tag{9.5}$$

with

$$A_m = \frac{2J_b J_m g_N}{e\gamma^2}, \quad \bar{\omega}_m = \frac{2}{\gamma}\omega_m. \tag{9.6}$$

We look for nT responses, i.e. periodic solutions $[y^{(n)}(\tau), z^{(n)}(\tau)]$ of equations (9.4) and (9.5) with a frequency $\omega_n = \bar{\omega}_m/n$, or, equivalently, with a period $T_n = n\bar{T}_m = n2\pi/\bar{\omega}_m$. In this case, the potential function $V(y,z)$ is no longer a constant of motion. However, for a periodic orbit, it is still true that the integral of

$$dV = \left[\frac{\partial V}{\partial y}\dot{y} + \frac{\partial V}{\partial z}\dot{z}\right] d\tau \tag{9.7}$$

over a period is equal to zero. By using this property and after replacing in the previous expression $\dot{y}$ and $\dot{z}$ coming from (9.4, 9.5), we obtain that the periodic solutions must satisfy the condition

$$\begin{aligned} A_m \int_0^{T_n} d\tau\, V_z(y^{(n)}(\tau), z^{(n)}(\tau)) \cos(\bar{\omega}_m \tau) = \\ \int_0^{T_n} d\tau\, D_{22}(y^{(n)}(\tau), z^{(n)}(\tau))[V_z(y^{(n)}(\tau), z^{(n)}(\tau))]^2, \end{aligned} \tag{9.8}$$

where V_z stands for $\partial V/\partial z$. The quasi–conservative theory assumes that the periodic orbits $[y^{(n)}(\tau), z^{(n)}(\tau)]$ can be approximated, near the resonance, by conservative orbits $[y_0(\tau - \tau_0, E_n),\, z_0(\tau - \tau_0, E_n)]$, corresponding to the value of the potential E_n that yields the desired frequency, $\omega_n = \omega(E_n)$. Substitution of this ansatz in the above equation leads to

$$\begin{aligned} A_m \int_0^{T_n} d\tau\, V_z(y_0(\tau, E_n), z_0(\tau, E_n)) \cos(\bar{\omega}_m(\tau + \tau_0)) = \\ \int_0^{T_n} d\tau\, D_{22}(y_0(\tau, E_n), z_0(\tau, E_n))[V_z(y_0(\tau, E_n), z_0(\tau, E_n))]^2. \end{aligned} \tag{9.9}$$

By defining R_n, S_n, θ_n by

$$\begin{aligned} R_n &= \int_0^{T_n} d\tau\, D_{22}(y_0(\tau, E_n), z_0(\tau, E_n))\, [V_z(y_0(\tau, E_n), z_0(\tau, E_n))]^2\,, \\ S_n \sin(\theta_n) &= \int_0^{T_n} d\tau\, V_z(y_0(\tau, E_n), z_0(\tau, E_n)) \sin(\bar{\omega}_m \tau), \\ S_n \cos(\theta_n) &= \int_0^{T_n} d\tau\, V_z(y_0(\tau, E_n), z_0(\tau, E_n)) \cos(\bar{\omega}_m \tau), \end{aligned} \tag{9.10}$$

we arrive at

$$A_m \cos(\bar{\omega}_m \tau_0 + \theta_n) = \frac{R_n}{S_n}. \tag{9.11}$$

According to this equation, for given A_m and $\bar{\omega}_m$ there exist at most $2n$ different orbits of period $n\bar{T}_m$. They correspond to the functions $[y_0(\tau - \tau_0, E_n),\, z_0(\tau - \tau_0, E_n)]$ for the $2n$ values of $\tau_0 = (\alpha_n + k\pi)/\bar{\omega}_m$, $k = 0, \ldots, 2n-1$ and $\alpha_n = \arccos(R_n/(S_n A_m)) - \theta_n$. It turns out that n of these solutions are unstable, while the remaining stable ones correspond in fact to trivial translations by a time amount $\bar{T}_m$ of the same basic solution (pulse position multistability [Gallagher *et al.*, 1985; Chizhevsky and Turovets, 1993]). Therefore, for a given value of A_m and $\bar{\omega}_m$ there is just one corresponding stable orbit of the conservative system.

Alternatively, we can look at the previous equation as a condition for the own existence of periodic orbits. For given modulation frequency $\bar{\omega}_m$ there will exist periodic orbits of period $n\bar{T}_m$ if the amplitude of the modulation verifies $A_m \geq R_n/S_n$. Since resonances almost coincide in this case with the limit of existence of periodic orbits (see Fig. 9.1 and the discussion of the previous section), this criterion implies that the skeleton curves for the nT resonance are

$$A_m = \frac{R_n}{S_n}. \tag{9.12}$$

In practice, it is difficult to find solutions of the conservative motion $[y_0(\tau, E), z_0(\tau, E)]$ analytically and one performs a numerical integration of the conservative system (putting by hand $D_{22} = 0$) in order to find the quantities R_n, S_n. However, in the simple case of $s = 0$ and $\varepsilon = 0$, Eq. (9.9) can be simplified by replacing $V_z = \dot{y}_0/(2y_0)$ with help of (9.4) and (7.21), yielding

$$A_m \int_0^{T_n} d\tau \dot{x}_0(\tau, E_n) \cos(\bar{\omega}_m(\tau + \tau_0)) = \int_0^{T_n} d\tau \left[b + y_{st} \exp(x_0(\tau, E_n))\right] \frac{\dot{x}_0(\tau, E_n)^2}{2}, \tag{9.13}$$

where $x_0 \equiv \ln(y_0/y_{st})$, $y_{st} = a - b$ is the steady state value of y in the absence of modulation, and x_0 is a periodic function of frequency w_n, that can be written as a Fourier series in the form

$$x_0(\tau, E_n) = \frac{Q_0}{2} + \sum_{k=1}^{\infty} Q_k \cos[k w_n(\tau + \mu_k)]. \tag{9.14}$$

Using this expression, and after a simple algebra, the integrals of (9.13) can be performed, giving rise to

$$A_m \sin[n\omega_n(\mu_n - \tau_0)] = \frac{a}{2}\omega_n \frac{\sum_{k=1}^{\infty} Q_k^2 k^2}{nQ_n}. \tag{9.15}$$

As discussed earlier, the nT resonances are obtained for $\sin[n\omega_n(\mu_n - \tau_0)] = 1$, i.e.

$$A_m = \frac{a}{2}\omega_n \frac{\sum_{k=1}^{\infty} Q_k^2 k^2}{nQ_n}. \tag{9.16}$$

This expression has the advantage that the contribution of each coefficient in the Fourier series of x_0 appears explicitly. In particular, it shows that the nT resonance may be excited by a finite amplitude of the external modulation only if the $n - th$ harmonic of the conservative solution is different from zero. Therefore, this effect can be considered as harmonic locking of the fundamental relaxation oscillation by an external modulation.

In the case $s \neq 0$ and $\varepsilon \neq 0$ it is also possible to use a series expansion for the variable x_0. However, the resulting expression is so complicated, in the sense that in the denominator different coefficients of the Fourier expansion contribute, that we find simpler instead to use (9.12) to obtain the theoretical skeleton curve.

9.2.2 Loss modulation

Let us turn now to loss modulation. We consider Eqs. (9.1) and (9.2) with a fixed value of the current J but modulated loss term

$$\gamma \to \gamma\,[1 + \gamma_m \cos(w_m t)]. \tag{9.17}$$

The reduced equations for y and z can be written as

$$\begin{aligned} \frac{dy}{d\tau} &= D_{12}\frac{\partial V}{\partial z} - 2y\gamma_m \cos(\bar{\omega}_m \tau), \\ \frac{dz}{d\tau} &= -D_{12}\frac{\partial V}{\partial y} - D_{22}\frac{\partial V}{\partial z}. \end{aligned} \tag{9.18}$$

It is straightforward now to extend the quasi–conservative theory to this case. Proceeding as in the case of pump modulation we arrive at

$$\gamma_m \cos(\bar{\omega}_m t_0 + \theta_n') = \frac{R_n}{S_n'}, \tag{9.19}$$

where (V_y stands for $\partial V/\partial y$), and

$$\begin{aligned} R_n &= \int_0^{T_n} d\tau\, D_{22}(y_0(\tau, E_n), z_0(\tau, E_n))\,[V_z(y_0(\tau, E_n), z_0(\tau, E_n))]^2, \\ S_n' \sin(\theta_n') &= -2\int_0^{T_n} d\tau\, V_y(y_0(\tau, E_n), z_0(\tau, E_n)) \sin(\bar{\omega}_m \tau) y_0(\tau, E_n), \\ S_n' \cos(\theta_n') &= -2\int_0^{T_n} d\tau\, V_y(y_0(\tau, E_n), z_0(\tau, E_n)) \cos(\bar{\omega}_m \tau) y_0(\tau, E_n). \end{aligned} \tag{9.20}$$

The skeleton curves are then given by

$$\gamma_m = \frac{R_n}{S_n'}. \tag{9.21}$$

In the case $s = 0$ and $\varepsilon = 0$, an expression in terms of Fourier series, similar to (9.16) can be derived,

$$\gamma_m = \frac{a}{2}\frac{\sum_{k=1}^{\infty} Q_k^2 k^2}{n^2 Q_n}. \tag{9.22}$$

This expression is equivalent to the one obtained in [Samson and Turovets, 1987] where a laser with periodic modulation of losses, but neglecting the spontaneous emission and gain saturation terms, is studied in detail. Again for s and ε different from zero we need to solve Eq. (9.21) numerically.

9.3 Numerical results

9.3.1 Pump modulation

We compare in figures 9.7 and 9.8 the predictions of the quasi–conservative theory, as given by (9.12) with the numerical simulations of Sec. 9.1. In order to perform this comparison, the skeleton curves have been plotted in terms of the original variables J_m and ω_m by using (7.8) and (9.6). Figure 9.7 gives evidence that the theoretical predictions coincide with the numerical results with a great degree of accuracy in the case $s = 0$ and $\varepsilon = 0$. This figure also shows that a similar agreement between the theory and simulations can be observed for the case of $s \neq 0$ but still $\varepsilon = 0$. In this case, the role of the gain saturation parameter s is such that, for a fixed value of the frequency ω_m, a larger value of modulation amplitude J_m is needed to obtain the optimal periodic response for each main resonance. The effect is quantitatively more important for higher order resonances, $n > 1$.

More dramatic is the effect of the spontaneous emission term ε. In figure 9.8 we can see that very small values of the noise rate ε strongly modify the skeleton curves for modulation frequencies ω_m smaller than a cut–off value ω_c (marked with an arrow in in the figure), whereas they remain basically unchanged for $\omega_m > \omega_c$. For small ω_m the effect of ε is such that much larger values of the modulation amplitude J_m are needed in order to find the optimal response for a given value of ω_m.

The theoretical prediction behaves qualitatively in the same way and predicts correctly the cut–off frequency ω_c. However, it predicts a much sharper increase of the optimal modulation amplitude. This could be explained as follows: while the period of the conservative solutions always increases when the energy increases in the absence of spontaneous emission terms, as it can be seen from Eq. (7.26), the presence of the spontaneous emission noise terms introduces a maximum in the resulting expression of the period as function of the energy. This fact forbids the conservative orbits with a frequency smaller than the cut–off frequency. This means that the conservative orbit we are using can be very different from the orbit followed by the modulated system. For smaller values of ε the boundary approaches to the one for the case $\varepsilon = 0$, as expected. Finally, in Fig. 9.9, the combined effect of s and ε is shown. The same qualitative effect that was already explained also appears for other values of the bias current J_b. For $J_b > 1.23 J_{th}$, the same boundaries appear but for larger values of J_m. This effect was already reported in [Liu and Ngai, 1993] where it is indicated that higher order bifurcations are more likely to occur for smaller dc bias levels than for higher ones.

9.3.2 Loss Modulation

For the case of loss modulation the analytical and numerical results coincide for $s = 0$ and $\varepsilon = 0$, and for the case $s \neq 0$ and $\varepsilon = 0$, analogously to that of the pump modulation case (see Fig. 9.10). However, when the spontaneous emission term is introduced, the boundaries obtained numerically also depart from the analytical predictions, see Figs. 9.11 and 9.12.

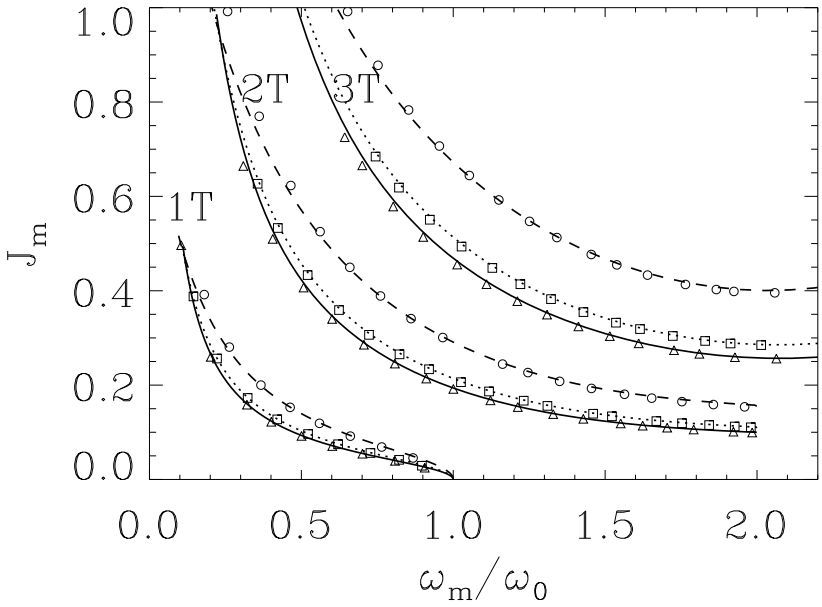

Figure 9.7: Maxima of main resonances in the plane $(\omega_m/\omega_0, J_m)$ for pump modulation. Effect of s. Analytical results (9.12): $s = 0$ (solid line), $s = 6 \times 10^{-9}$ (dotted line), $s = 3 \times 10^{-8}$ (dashed line). Numerical results: $s = 0$ (triangles), $s = 6 \times 10^{-9}$ (squares), $s = 3 \times 10^{-8}$ (circles). $\varepsilon = 0$. Other parameters as in Fig. 9.1.

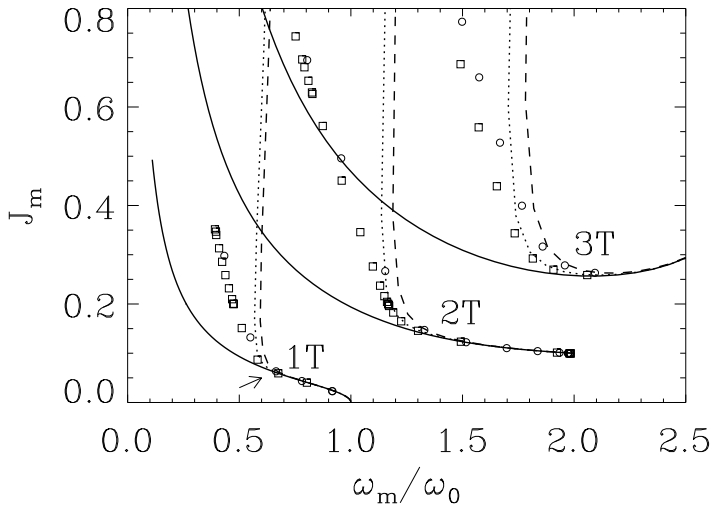

Figure 9.8: Maxima of main resonances in the plane $(\omega_m/\omega_0, J_m)$ for pump modulation. Effect of ε. Analytical results (9.12): $\varepsilon = 0$ (solid line), $\varepsilon = 6.2{\times}10^{-11} ps^{-1}$ (dotted line), $\varepsilon = 2.2{\times}10^{-10} ps^{-1}$ (dashed line). Numerical results: $\varepsilon = 6.2 \times 10^{-11} ps^{-1}$ (squares), $\varepsilon = 2.2 \times 10^{-10} ps^{-1}$ (circles). $s = 0$. Other parameters as in Fig. 9.1. Marked with an arrow the cut-off value ω_c.

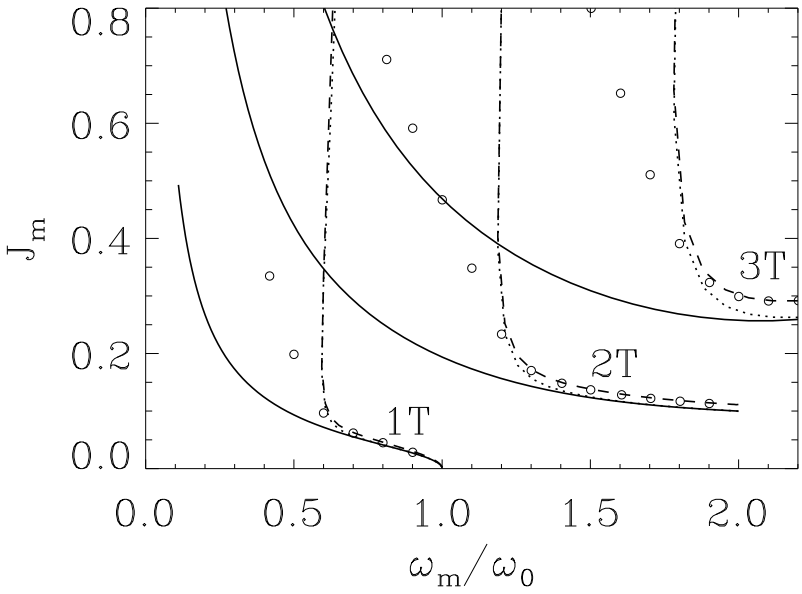

Figure 9.9: Maxima of main resonances in the plane $(\omega_m/\omega_0, J_m)$ for pump modulation. Combined effect of ε and s. Analytical results (9.12): $\varepsilon = 0$, $s = 0$ (solid line), $\varepsilon = 6.2 \times 10^{-11} ps^{-1}$, $s = 0$ (dotted line), $\varepsilon = 6.2 \times 10^{-11} ps^{-1}$, $s = 6 \times 10^{-9}$ (dashed line). Numerical results: $\varepsilon = 6.2 \times 10^{-11} ps^{-1}$, $s = 6 \times 10^{-9}$ (circles). Other parameters as in Fig. 9.1.

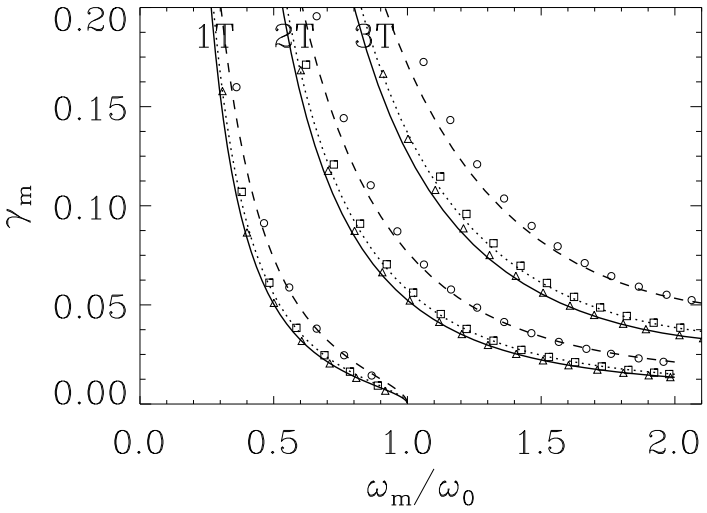

Figure 9.10: Maxima of main resonances in the plane $(\omega_m/\omega_0, J_m)$ for loss modulation. Effect of s. Analytical results (9.21): $s = 0$ (solid line), $s = 6 \times 10^{-9}$ (dotted line), $s = 3 \times 10^{-8}$ (dashed line). Numerical results: $s = 0$ (triangles), $s = 6 \times 10^{-9}$ (squares), $s = 3 \times 10^{-8}$ (circles). $\varepsilon = 0$. Other parameters as in Fig. 9.1.

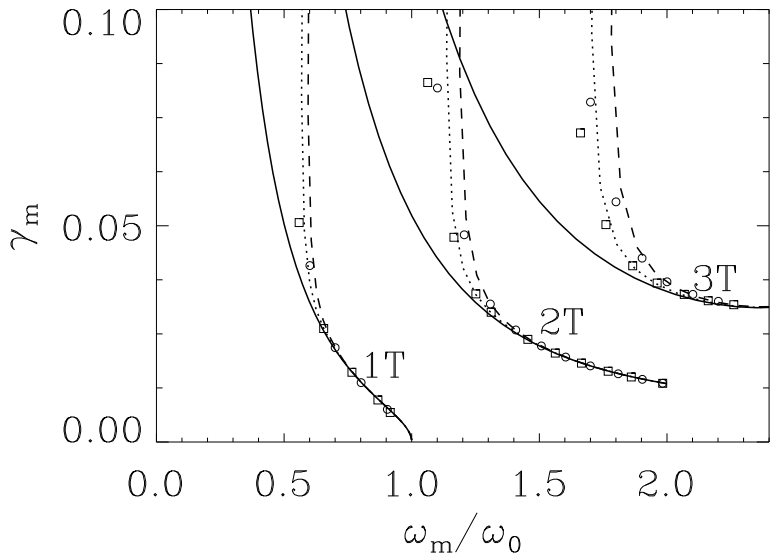

Figure 9.11: Maxima of main resonances in the plane $(\omega_m/\omega_0, J_m)$ for loss modulation. Effect of ε. Analytical results (9.21): $\varepsilon = 0$ (solid line), $\varepsilon = 6.2\times10^{-11}ps^{-1}$ (dotted line), $\varepsilon = 2.2\times10^{-10}ps^{-1}$ (dashed line). Numerical results: $\varepsilon = 6.2 \times 10^{-11}ps^{-1}$ (squares), $\varepsilon = 2.2 \times 10^{-10}ps^{-1}$ (circles). $s = 0$. Other parameters as in Fig. 9.1.

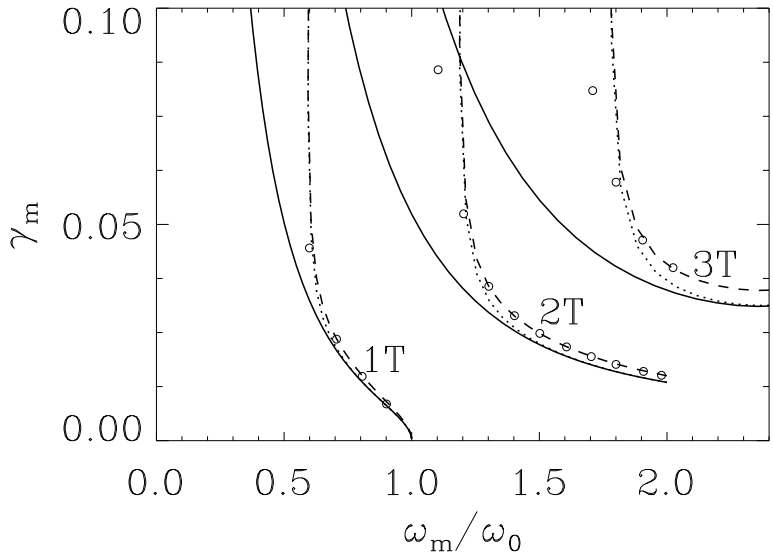

Figure 9.12: Maxima of main resonances in the plane $(\omega_m/\omega_0, J_m)$ for loss modulation. Combined effect of ε and s. Analytical results (9.21): $\varepsilon = 0$, $s = 0$ (solid line), $\varepsilon = 6.2 \times 10^{-11}ps^{-1}$, $s = 0$ (dotted line), $\varepsilon = 6.2 \times 10^{-11}ps^{-1}$, $s = 6 \times 10^{-9}$ (dashed line). Numerical results: $\varepsilon = 6.2 \times 10^{-11}ps^{-1}$, $s = 6 \times 10^{-9}$ (circles). Other parameters as in Fig. 9.1.

It is possible to obtain an interesting relation between the effect produced by loss modulation and pump modulation. The relation can be obtained more clearly if we write the evolution equation for the variable $x = \ln(y/y_{st})$, defined in terms of the stationary value y_{st} of the variable y in the absence of modulation. For small ε, s, it is $y_{st} \approx a - b$. It turns out that the resulting equations in the case of modulation in the pump or in the losses take basically the same form, namely

$$\ddot{x} + \dot{x}^2 G_1(x) + \dot{x} G_2(x) + G_3(x) = F_{P,L}(x, \tau), \tag{9.23}$$

$G_1(x)$, $G_2(x)$, and $G_3(x)$ are given functions of x whose detailed expressions are not needed here. The only difference is in the right hand side of this equation which for the case of modulation in the pump is

$$\begin{aligned} F_P(x,\tau) &= A_m \cos(\bar{\omega}_m \tau)\, F_1(x), \\ F_1(x) &= \frac{2}{1 + \bar{s} y_{st} \exp(x)} + \frac{c}{y_{st} \mathrm{e}^x}, \end{aligned} \tag{9.24}$$

while in the case of modulation in the losses it is:

$$F_L(x, \dot{x}, \tau) = 2\gamma_m \bar{\omega}_m \sin(\bar{\omega}_m \tau) - 2\gamma_m \cos(\bar{\omega}_m \tau) F_2(x, \dot{x}), \tag{9.25}$$

$$F_2(x, \dot{x}) = b + \frac{y_{st} \exp(x)}{1 + \bar{s} y_{st} \exp(x)} + \dot{x} \left[\frac{2\bar{s} y_{st}^2 \mathrm{e}^{2x} + c(1 + \bar{s} y_{st} \mathrm{e}^x)^2}{(1 + \bar{s} y_{st} \mathrm{e}^x)[2 y_{st} \mathrm{e}^x + c \mathrm{e}^{2x}(1 + \bar{s} y_{st} \mathrm{e}^x)]} \right]. \tag{9.26}$$

It is easy to see that the term containing F_2 is negligible compared to the first contribution to $F_L(x, \dot{x}, \tau)$. In fact, if we consider the value of F_2 in the steady state in the absence of modulation, $x = \dot{x} = 0$, we obtain $F_2 \approx a$. A typical value is $a \approx 0.01$ while the product $\gamma_m \bar{\omega}_m$ is of order 1 for $\omega_m \sim \omega_0$. If we replace now $F_1(x)$ by its steady state value $F_1(0)$, approximate the term $1 + \bar{s} y_{st} \approx 1$ and neglect the term proportional to c , we arrive at

$$F_P \approx 2A_m \cos(\bar{\omega}_m \tau), \tag{9.27}$$

$$F_L \approx 2\gamma_m \bar{\omega}_m \sin(\bar{\omega}_m \tau). \tag{9.28}$$

Therefore, we conclude that the role of the modulation in the pump is equivalent to the modulation in the losses, besides a trivial phase shift, if $A_m = \gamma_m \bar{\omega}_m$. In terms of the physical parameters, this is equivalent to

$$J_m = \gamma_m \omega_m \frac{\gamma e}{g_N J_b}. \tag{9.29}$$

This result shows that modulation in the pump or in the losses produce equivalent results if the respective modulation amplitudes are conveniently rescaled. It is possible to arrive at this result directly, in the case $s = \varepsilon = 0$, by comparing the expressions in terms of Fourier coefficients (9.16) and (9.22). The validity of this equivalence of modulation in the pump and in the losses is shown in Figs. 9.13 and 9.14, where we compare, for typical values of s and ε, the skeleton lines in the case of pump and loss modulation after the latter have been rescaled according to (9.29).

It is clear from these figures that the proposed equivalence after parameter rescaling works well in the cases that have been shown. A similar agreement is observed for other boundaries and values of the parameters.

Since relation (9.29) implies, for typical values of the parameters, that $J_m > \gamma_m$ we recover the known results that loss modulation is more efficient to get bifurcations and chaos. This relation can be applied in the large modulation signal regime (nonlinear regime), and hence it can be considered as an extension of previous analytical results in the case of the linear regime [Tredicce *et al.*, 1985b].

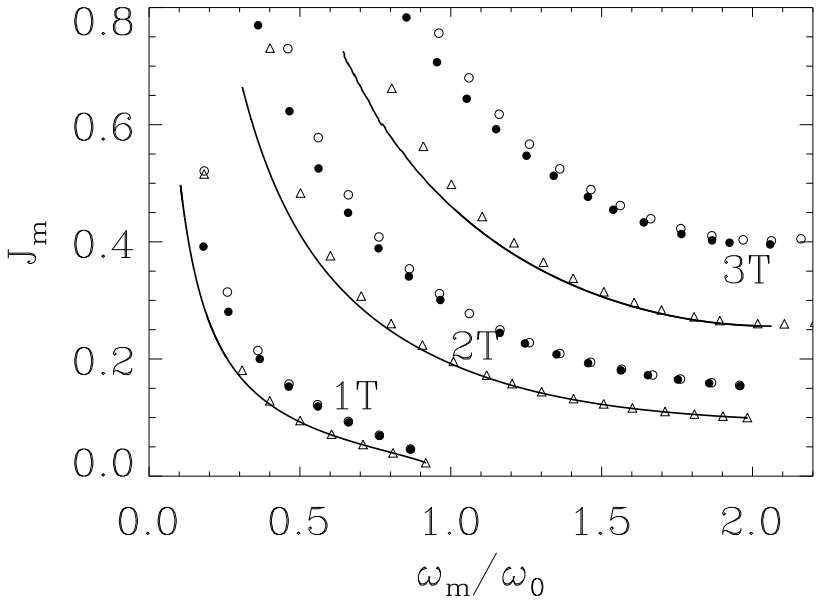

Figure 9.13: Maxima of main resonances in the plane $(\omega_m/\omega_0, J_m)$. Numerical results. Pump modulation: $s = 0$ (solid line) (equivalent to theoretical results), $s = 3 \times 10^{-8}$ (filled circles). Loss modulation multiplied by factor of Eq. (9.29): $s = 0$ (triangles), $s = 3 \times 10^{-8}$ (circles). $\varepsilon = 0$, $J_b = 1.23 J_{th}$.

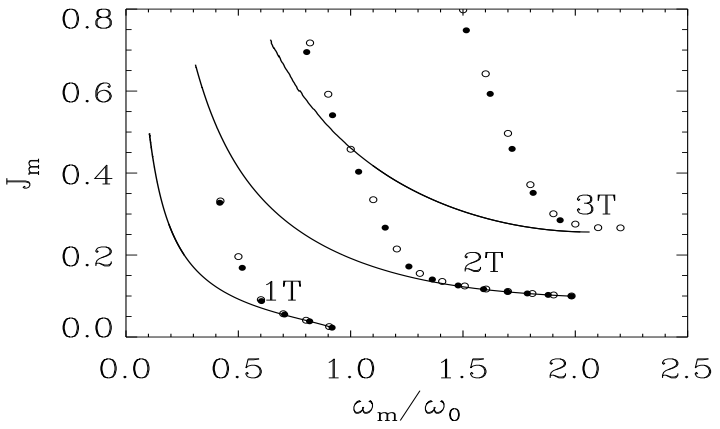

Figure 9.14: Maxima of main resonances in the plane $(\omega_m/\omega_0, J_m)$. Numerical results. Pump modulation: $\varepsilon = 0$ (solid line), $\varepsilon = 2.2 \times 10^{-10} ps^{-1}$ (filled circles). Loss modulation multiplied by factor of Eq. (9.29): $\varepsilon = 2.2 \times 10^{-10} ps^{-1}$ (circles). $s = 0$, $J_b = 1.23 J_{th}$.

9.4 Comparison to experiments

The fingerprints of nT resonance regimes, which discern from non–resonance nT periodic windows in chaos, is a dominant ω_m/n component in microwave spectra. In particular, $\omega_m/2$ component in microwave spectra was dominating in the observations of Refs. [Liu and Ngai, 1993; Bennett *et al.*, 1997; Matsui *et al.*, 1998; Wada *et al.*, 1998], pointing out the resonance $2T$ regime, that in time domain leads to sharp spikes like the ones presented in Fig. 9.2 (b) (no intermediate spikes at interval $2T_m$). A direct example of resonant $2T$ regime observation and possible applications to all-optical clock division can be found in [Yang and Liu, 2001].

According to our predictions, resonant regimes with $n > 2$ also exist in the system. However, they are dynamical isolas that cannot be observed with smooth sweeping of modulation parameters, besides the special cases of pulse excitation [Samson *et al.*, 1990; Chizhevsky and Turovets, 1993; Chizhevsky, 2000] or chaotic crisis on the basic $1T$ periodic branch leading to switching to a $3T$ branch as it was observed in [Liu and Ngai, 1993] and explained in [Lamela *et al.*, 1998a; Lamela *et al.*, 1998b]. Particularly relevant to our work is the paper by Liu and Ngai [Liu and Ngai, 1993] where the response of a single mode distributed feedback laser subjected to current modulation is considered experimentally. We summarize the observations they obtain when changing the modulation frequency and amplitude of the radio frequency signal and compare them to our results:

a) For small modulation frequency there is only a $1T$ period response for any signal amplitude. This behaviour also appears in our system, as it was visualized in Fig. 9.7 for $\omega_m/\omega_0 < 0.2$, for $J_m < 1$.

b) For intermediate modulation frequency there is a transition from $1T$ to $2T$

responses when increasing the modulation amplitude. This fact could be seen in Fig. 9.7 in the region $0.2 < \omega_m/\omega_0 < 2.$, for the corresponding values of J_m. A further transition from $2T$ back to $1T$ is experimentally, but nor numerically, observed.

c) $3T$ and $4T$ solutions appear for large enough modulation frequency and amplitude. We find these solutions also in the case of large enough values of the modulation frequency and amplitude, see Figs. 9.7, 9.8 and 9.9. The $4T$ solution would appear for larger values of the amplitude not plotted in the figure. We have checked that for $s = 0$ and $\varepsilon = 0$ the corresponding $4T$ boundary for pump modulation would have its minimum value at $\omega_m/\omega_0 \sim 2.3$ and $J_m \sim 0.4$. However, identification of the $3T$ branch observed in [Liu and Ngai, 1993; Bennett *et al.*, 1997] is still hard to make as resonant due to the fact that the microwave spectra gives a dominate modulation component at ω_m, but not at the subharmonic $\omega_m/3$ as it might be expected for a purely resonant regime.

9.5 Discussion

We have undertaken a numerical and analytical study to identify the optimal responses of a semiconductor laser subjected to an external periodic modulation in the pump of relative amplitude J_m and frequency ω_m. We have computed the lines in the $(\omega_m/\omega_0, J_m)$ plane that give a maximum response for each type of nT resonance (skeleton lines) and compared them to the numerical results. The influence of saturation and spontaneous emission terms on the dynamics has also been examined. We have found that these specific laser diode parameters increase the thresholds of instabilities in the system, a fact that can be interpreted as an effect of the increase in the damping of relaxation oscillations. A qualitative comparison with experiments has also been performed, our results qualitatively agree in part with the experimental observations with $1.55\mu m$ InGaAs distributed lasers [Liu and Ngai, 1993]. The analytical results we have obtained by an application of the quasi–conservative theory allow us to explain satisfactorily the effect of the saturation term. The role of the gain saturation parameter is such that, for a fixed value of the frequency ω_m, a larger value of modulation amplitude J_m is needed to obtain the optimal periodic response for each main resonance. This effect is more important for higher order resonances. However, the effect of the spontaneous emission term in the skeleton lines has not been completely explained by the analytical results and the discrepancy between the numerical and analytical results is due to the form of the conservative solution.

Loss modulation has also been considered and analytical and numerical results are in reasonable agreement. Furthermore, we have obtained a relation that shows the equivalence between pump and loss modulation. This equivalence relation, having a large validity for the numerical boundaries, allows to compute the boundary limits for pump (or loss) modulation if the loss (pump) boundaries are known. We have explain the experimental results that loss modulation is more efficient to get bifurcation and chaos than pump modulation.

Conclusions

Conclusions i possibles extensions

En aquest treball s'ha estudiat la dinàmica dels làsers de classe A i de classe B en termes del potencial de Lyapunov. En el cas que s'injecti un senyal al làser o es modulin alguns dels paràmetres, apareix un comportament molt més complex i s'estudia el conjunt de bifurcacions.

1) Als làsers de classe A, la dinàmica determinista s'ha interpretat com el moviment damunt el potencial de Lyapunov, i s'han identificat els termes relaxacionals i conservatius en les equacions de la dinàmica. L'efecte combinat d'aquests dos termes produeix una trajectòria espiral en el pla definit per les parts real i imaginària del camp elèctric, amb una velocitat angular proporcional al terme de disintonia.

En la dinàmica estocàstica (quan termes de renou additiu s'inclouen en les equacions) s'obté un *flux sostingut per renou* per a la fase del camp elèctric, que prové de la interacció dels termes conservatius i els termes de renou. Aquest flux en la fase es manifesta com un corriment de la freqüència intrínseca d'emissió de la llum làser. Una expressió analítica permet calcular l'evolució de la fase. Encara que seria interessant comprovar experimentalment l'existència d'aquest corriment de freqüència induït per renou, cal recalcar que d'acord amb els nostres resultats, la intensitat del renou que es requereix per obtenir un corriment de freqüència observable és molt més gran que la intensitat de renou típica en els experiments. No obstant, aquest renou extra necessari podria ésser induït externament. A més, el corriment de freqüència, obtingut en els làsers de classe A, apareix en altres tipus de làsers, com en els làsers de classe B, encara que en aquest cas s'hauria de desenvolupar una teoria apropiada. Caldria resaltar la importància d'aquest flux induït per renou. Aquest podria aparèixer en altres sistemes, i seria en particular interessant considerar un símil mecànic del potencial de Lyapunov que s'ha obtingut.

2) Per als làsers de classe A amb senyal injectat, s'ha descrit el conjunt de bifurcacions complet (de forma analítica i numèrica) i s'ha determinat el conjunt d'amplituds (ρ) i freqüències (η) en el qual el làser respon ajustant la seva freqüència a la del camp extern. Aquest resultat apareix resumit a la Fig. 6.2 (c) on s'ha identificat regions on la resposta no és a la mateixa freqüència de la d'injecció (indicades amb NL a aquella figura). A dins les regions on el làser respon a la mateixa freqüència que la d'injecció es pot distingir entre una regió on hi ha una única resposta estable (L), regions de coexistència de la solució a la mateixa freqüència de la

d'injecció amb una a distinta freqüència (C), i finalment un a regió on hi coexisteixen dues solucions a la mateixa freqüència que la freqüència d'injecció però amb distinta intensitat (B). S'han descrit qualitativament les característiques observades en la dinàmica determinista en termes del potencial de Lyapunov, identificant els termes relaxacionals, conservatius i els residuals en les equacions dinàmiques. Encara que aquesta descripció és estrictament vàlida només en el cas de senyal injectat amb freqüència zero, les característiques qualitatives no canvien quan el producte $\rho\eta$ és petit.

A la dinàmica estocàstica (quan el renou additiu que prové de l'emissió espontània es considera explícitament en les equacions), s'ha utilitzat la imatge del potencial de Lyapunov per explicar la presència del *corriment de freqüència estocàstic* del llum làser igual com s'havia fet en els làsers de classe A sense injecció. El mateix potencial permet realitzar un càlcul quantitatiu d'aquest efecte. Els resultats s'ajusten a les simulacions numèriques de les equacions model i esperam que serveixin de guia per a futurs experiments en l'observació en sistemes làsers reals, tot i que s'hauran de tenir en compte les limitacions experimentals i termes de renou a l'hora de fer comparacions.

3) En el cas dels làsers de class B, s'ha obtingut un potencial de Lyapunov només vàlid en el cas determinista, quan les fluctuacions de renou es menyspreen. La dinàmica és del tipus no relaxacional amb una matriu D no constant. El punt fix corresponent a que el làser es troba a l'estat d'encès s'ha interpretat com el mínim del potencial. La relaxació cap a aquest mínim es realitza a través d'oscil·lacions esmorteïdes. A partir de l'observació que el valor del potencial és quasi bé constant entre dos pics consecutius d'intensitat, durant el procés transitori de relaxació cap a l'estat estacionari, s'ha pogut obtenir una expressió aproximada per al període d'aquestes oscil·lacions. A més, l'expressió que relaciona el període de les oscil·lacions al valor del potencial ens ha permès obtenir una relació semiempírica que ajusta (sense cap paràmetre ajustable i amb gran exactitud) el període de les oscil·lacions des del règim no lineal fins a les oscil·lacions de relaxació a prop de l'estat estacionari.

4) Hem realitzat un estudi del conjunt de bifurcacions parcial al voltant del règim tipus II de la singularitat Hopf–sella–node en un làser de classe B amb senyal injectat, a causa de què existia una falta d'estudi detallat al voltant d'aquest tipus en la literatura existent. Els paràmetres de bifurcació que s'han considerat són la intensitat del senyal injectat i la disintonia entre la freqüència de la pertorbació i la freqüència d'operació del làser sense injecció. El centre d'organització principal és una bifurcació Hopf–sella–node des d'on s'origina una bifurcació secundària d'òrbites periòdiques, i neix un torus a aquella bifurcació. Es veu que la solució làser estable que existeix per a valors d'injecció baixos, també sofreix una bifurcació de Hopf secundària, creant–se un altre torus. Aquests tours tenen resonàncies per alguns dels valors dels paràmetres: poden existir òrbites tancades damunt els torus. L'estructura de resonàncies dels dos torus interacciona, i a més s'obtenen òrbites homoclíniques

a l'estat apagat a dins de cada una de les llengües d'Arnold. Un dels resultats més importants és l'acumulació de totes les resonàncies cap a la singularitat Hopf–sella–node, que indica l'existència d'una bifurcació global altament degenerada en el punt de codimensió–2.

Es pot comparar el conjunt de bifurcacions obtingut pel làser de classe B amb senyal injectat amb el del làser de classe A amb senyal injectat. La diferència principal entre els dos tipus de làsers des del punt de vista dinàmic és el nombre de variables amb què es treballa. Pels làsers de classe A és suficient amb dues variables i es pot descriure el conjunt complet de bifurcacions. Pels làsers de classe B cal considerar tres equations, i és per aquest motiu que una varietat de fenòmens molt més complexa pot aparèixer. Encara que part de l'estructura de bifurcacions dels làsers de classe B ja estava present en els làsers de classe A (esencialment les tres corbes corresponents a les bifurcacions sella–node de punts fixos), la dinàmica completa del làser de classe B és extremadament complicada. Hem vist que la presència del punt Hopf–sella–node és molt important en els làsers de classe B i que distints tipus de comportaments es poden obtenir. En canvi, la intersecció de les bifurcacions Hopf i sella–node de punts fixos en el cas de classe A no pot ser dels tipus Hopf–sella–node sinó que es tracta de singularitats Takens–Bogdanov. No obstant, aquests singularitats ja eren presents (encara que de distinta manera) en els làsers de classe B incloent–hi bifurcacions d'òrbites periòdiques enlloc de punts fixos. Les bifurcacions d'Andronov globals també s'han obtingunt en ambdós tipus de làsers. El conjunt de bifurcacions per als làsers de classe A per $\alpha = 0$ és molt més senzill que el del cas $\alpha \neq 0$, i aquest darrer es pot obtenir a partir del cas $\alpha = 0$ realitzant alguns canvis. Aquesta situació torna a ser reminiscent del cas del làser de classe B.

5) S'han identificat les respostes òptimes pels làsers de semiconductor sotmesos a modulació periòdica externa. S'han obtingut les corbes que donen la resposta màxima per cada tipus de resonància nT en el pla definit per l'amplitud relativa de modulació i la freqüència de modulació. Aquests dominis d'existència de les resonàncies principals s'han obtingut mitjançant l'aplicació de la teoria quasi–conservativa. Les prediccions han estat comparades amb els resultats numèrics obtinguts a partir de la integració directa d'equacions model, així com amb observacions experimentals descrites per altres grups. En ambdós casos s'obté una concordància qualitativa. S'ha considerat un model que conté explícitament els termes de saturació de guany i els termes d'emissió espontània. Els termes d'emissió espontània modifiquen en gran mesura el comportament qualitatitu dels límits de les inestabilitats, mentre que el terme de saturació de guany dóna lloc a un simple corriment dels límits. Els resultats que s'obtenen teòricament reprodueixen aquest comportament qualitatiu. Finalment, s'observa que la modulació en el bombeig i la modulació en les pèrdues produeixen resultats equivalents si les respectives amplituds de modulació es reescalen de manera adequada. Aquesta relació d'equivalència permet calcular límits d'existència per a la modulació al bombeig (o a les pèrdues) a partir dels límits a les pèrdues (o al bombeig). Es recupera el resultat conegut que

la modulació al terme de pèrdues és més eficient que la modulació al bombeig per obtenir bifurcacions i caos.

Algunes posssibles extensions d'aquest treball inclourien:

- Estudiar la dinàmica del làser en presència de renou en el paràmetre de bombeig. En general, degut a la dinàmica lenta dels portadors, el renou no es considerarà blanc, sinó que de manera més realista es modelitzarà com un renou de color. Aquesta font de renou afecta principalment a les característiques espectrals del làsers. Si es pogués obtenir un potencial de Lyapunov, satisfent la relació de fluctuació–dissipació es podria calcular qualsevol valor mig d'interès a l'estat estacionari.

- Obtenir una forma explícita pel potencial de Lyapunov pel làser amb un camp extern injectat. En el cas del làser de classe A en tenim l'expressió en alguns casos particulars, i a partir d'ella, podem inferir la forma qualitativa general. En el cas del làser de classe B es tractaria d'un problema nou.

- Obtenir el potencial de Lyapunov que té en compte la pulsació auto-sostinguda en alguns làsers de semiconductor. En aquests sistemes, el nombre de fotons i les densitats d'electrons no són constants a l'estat estacionari sinó que oscil·len en el temps. Es pot especular que en aquest cas el potencial seria similar a l'obtingut per al làser de classe B però en aquest cas l'estat estacionari no es tractaria d'un punt fix sinó d'un cicle límit, que es podria obtenir a partir d'una dinàmica residual.

- El corriment de freqüència induït per renou en els làsers de classe A també s'ha obtingut numèricament en alguns tipus de làsers de classe B. Per als làsers de classe A és possible obtenir una expressió analítica per al corriment de freqüència estocàstic ja que la descripció mitjançant la funció de Lyapunov de la dinàmica és tal que la relació fluctuació–dissipació es satisfà. No obstant, encara que ha estat possible obtenir una funció de Lyapunov per als làsers de classe B, la relació fluctuació–dissipació no es satisfà per a aquest tipus de làsers i la funció de Lyapunov no pot donar una descripció completa de la distribució estacionària en el cas estocàstic. Per tant, és un problema obert obtenir una descripció teòrica satisfactòria per al corriment de freqüència induït per renou per als làsers de classe B.

- En aquest treball s'ha obtingut part del conjunt de bifurcacions en el cas del làser de classe B amb senyal injectat. Es podria continuar amb aquesta anàlisi i cercar altres bifurcacions en el mateix espai de paràmetres. Seria interessant relacionar les distintes bifurcacions que es troben per als distints tipus de la bifurcació Hopf–sella–node. A més, en el nostre estudi s'ha restringit l'anàlisi a la regió a prop del centre organitzatiu Hopf–sella–node, i es podria realitzar l'estudi en regions allunyades d'aquest punt.

Conclusions and Outlook

In this work we have studied the dynamics of both class A and class B lasers in terms of Lyapunov potentials. In the case of an injected signal or when some laser parameteres are modulated, and more complex behaviour is expected, the bifurcation set is studied. The main results are the following:

1) For class A lasers, the deterministic dynamics has been interpreted as a movement on the potential landscape, and the relaxational and conservative terms in the dynamical equations of motion have been identified. The combined effects of these two terms produce an spiraling trajectory in the plane defined by the real and imaginary parts of the electric field, with an angular velocity proportional to the detuning parameter.

In the stochastic dynamics (when additive noise is included in the equations) we have found a *noise sustained flow* for the phase of the electric field. It arises from the interaction of the conservative terms with the noise terms. This phase flow manifests as an intrinsic frequency shift of the laser light. An analytical expression allows the calculation of the phase evolution. Although it would be interesting to check experimentally the existence of this noise induce phase drift, we have to stress that, according to our results, the noise intensity required for an observable phase drift is much larger than the typical noise intensity in experiments. Nevertheless, this necessary extra noise could be externally induced. Moreover, this phase drift, obtained for class A lasers, is also present in other types of lasers as, e.g., class B lasers, although for the latter an appropriate theory should be developed. We believe that this is an important and new effect that could appear in other laser systems. It would be interesting to develop a mechanical simile of the Lyapunov potential obtained, that could help us to relate the phenomenon predicted here with other cases of noise sustained flow well documented in the literature.

2) For class A lasers with an injected signal, we have been able to describe the whole bifurcation set of this system (by using analytical and numerical tools) and to determine the *locking range*, i.e. the set of amplitudes (ρ) and (detuning) frequencies (η) for which the laser responds adjusting its frequency to that of the external field. This result is summarized in Fig. 6.2 (c) in which we can identify non–locking regions (labelled NL in that figure). Within the locking range one finds a region with a single stable laser response (L), regions of coexistence of a locking

solution with a non–locking solution (C), as well as a region of coexistence of two locking solutions of different light intensity (B). We have described qualitatively the observed features of the deterministic dynamics in terms of a Lyapunov potential function. We have identified the relaxational, conservative and residual terms in the dynamical equations of motion. Although this description is strictly valid only in the case of a zero–detuning injected signal, the qualitative features remain unchanged when the product $\rho\eta$ is small.

In the stochastic dynamics (when the additive noise coming from the spontaneous emission is explicitly considered in the equations) we have used the Lyapunov potential image to explain the presence of a *stochastic frequency shift* of the laser light. The same potential function allows a quantitative calculation of this effect. The results are in good agreement with numerical simulations of the model equations and we hope that they can be a guide for future experiments in observing this effect in laser systems.

3) In the case of class B lasers, we have obtained a Lyapunov potential only valid in the deterministic case, when noise fluctuations are neglected. We have found that the dynamics is non–relaxational with a nonconstant matrix D. Hence, the fixed point corresponding to the laser in the *on* state has been interpreted as a minimum in this potential. Relaxation to this minimum is reached through damped oscillations. The observation that the potential is nearly constant between two consecutive intensity peaks during the transient relaxation process towards the steady state, has allowed us to obtain an approximate expression for the period of these oscillations. Moreover, an expression relating the period of the oscillations to the value of the potential has allowed us to find a semi–empirical relation that fits (with no adjustable parameters and with a high degree of accuracy) the period of the oscillations from the nonlinear regime up to the relaxation oscillations near the steady state.

4) We have performed a study of the partial bifurcation set around the type II regime of the Hopf–saddle–node singularity in a class B laser with injected signal. Such a detailed study around this regime was missing in the previous literature. The bifurcation parameters we have considered are the intensity of the injected signal and the detuning of the perturbation frequency and the unperturbed laser operating frequency. The main organizing center of the system is the Hopf–saddle–node bifurcation from where a secondary Hopf bifurcation of a periodic orbit originates, and a torus is born at this latter bifurcation. We show that the laser's stable cw solution existing for low injections also suffers a secondary Hopf bifurcation and another torus is created. These tori have resonances for some values of the parameters, in the sense that close orbits on the tori can appear. The resonance structure of both tori interact and homoclinic orbits to the off state are found inside each Arnold tongue. A connection between different resonances in the parameter space has also been obtained. One of the main results is the accumulation of all the above resonances towards the Hopf–saddle–node singularity points to the occurrence of a highly degenerate global bifurcation at the codimension–2 point.

We can compare the bifurcation set obtained for a class B laser with injected signal with the one obtained for a class A laser with injected signal. From the dynamical point of view, the main difference between the two kinds of lasers is the number of variables involved. For class A lasers two variables suffice and the full bifurcation set can be described. For class B lasers, a three–equations system, a more complex variety of phenomena can appear and the system can also show chaotic behaviour. Although part of the bifurcation structure of class B lasers is already present in class A lasers (essentially the tree curves of saddle–node bifurcations of fixed points), the overall dynamics of the former becomes extremely complicated. We have seen that the presence of the Hopf–saddle–node point has a crucial importance for class B lasers and different types of flows can be obtained. Note as contrast that the intersection of Hopf and saddle–node bifurcations of fixed points in class A lasers cannot be of Hopf–saddle–node types but are Takens–Bogdanov singularities instead. Such singularities are also present (in a different form) in class B lasers, not involving bifurcations of fixed points but of periodic orbits. Andronov global bifurcations have also been found in both types of lasers. The bifurcation set for a class A laser in the case $\alpha = 0$ is much simpler than the one found for $\alpha \neq 0$ although the former can be obtained by suitable reduction of the latter. This situation is again reminiscent of the class B laser case.

5) We have identified the optimal responses of a semiconductor laser subjected to an external periodic modulation. The lines that give a maximum response for each type of nT resonance (skeleton lines) are obtained in the plane defined by the relative amplitude modulation and frequency modulation. The domains of existence of the main resonances are obtained by application of the quasi–conservative theory. The predictions are compared with numerical results coming from a direct integration of the model equations and with experimental observations reported by other groups. In both cases we find a good qualitative agreement. We have considered a model that contains explicitly the gain saturation and spontaneous emission terms and we have focused mainly on the effect that these terms have in the regime of large amplitude modulation. We find that the spontaneous emission qualitatively modifies the behaviour of the instabilities boundaries, while the gain saturation leads to a simple quantitative shift of boundaries. Our theoretical results reproduce this overall behaviour. We also find that modulation in pump or losses produce equivalent results if the respective modulation amplitudes are conveniently rescaled. This equivalence relation allows to compute the boundary limits for pump (or loss) modulation if the loss (pump) boundaries are know. We have recovered the results that loss modulation is more efficient to get bifurcations and chaos than pump modulation.

Some possible extensions of this work include:

- To study laser dynamics in the presence of noise in the pump parameter. In general, and due to the slower dynamics of the carriers variable, the noise

should not be considered as white but more realistically it should be modelled as a colored noise. This noise source mainly affects the spectral characteristics of the lasers. If a Lyapunov Potential, satisfying the fluctuation–dissipation relation could be obtained then any mean value of interest in the steady state could be calculated.

- To obtain a complete Lyapunov potential for lasers in the presence of an external field. For class A lasers this has been done for some particular cases and it was possible to infer the qualitative form of the potential in the most general case. For class B lasers with injected signal it would be interesting to perform the description of its dynamics in terms of a Lyapunov potential.

- To obtain a Lyapunov potential that accounts for the self–sustained pulsation phenomena that occurs in some semiconductor lasers. In these systems, the photon number and electron densities are not constant in the steady state but oscillate in time. We speculate that in this case, the potential would be quite similar to that obtained for class B lasers, but the steady state will not be a fixed point, but a limit cycle instead, which could be obtained as a residual dynamics.

- The noise frequency shift obtained in class A lasers has also been found numerically in some class B lasers. For class A lasers it is possible to reach a complete understanding of this stochastic frequency shift since the Lyapunov function description of the dynamics is such that the fluctuation–dissipation relation is satisfied. However, although we have been able to find a Lyapunov function for class B lasers, the fluctuation–dissipation relation is not satisfied for this kind of lasers and the Lyapunov function can not give us a complete description of the stationary distribution in the stochastic case. Therefore, it is an open problem to obtain a satisfactory theoretical description of the noise induced frequency shift for class B lasers.

- We have obtained a subset of the bifurcation set in the case of a class B laser with injected signal. It would be interesting to follow the analysis of this bifurcation set and look for other bifurcations. The important point should be to relate the bifurcations encountered for one type of the Hopf–saddle–node bifurcation to another. Moreover, the analysis of the bifurcation set has been restricted to a region in the space of parameters near the Hopf–saddle-node organizing center, it would be interesting to perform an study in a region far of that center.

List of Figures

3.1 Saddle–node bifurcation. 41
3.2 Transcritical bifurcation. 41
3.3 Pitchfork bifurcation (supercritical). 41
3.4 Pitchfork bifurcation (supercritical), including a high order term. . . 41
3.5 Pitchfork bifurcation (subcritical). 42
3.6 Hopf bifurcation. 43
3.7 Hopf–saddle–node bifurcation for the type *I* case. 45
3.8 Hopf–saddle–node bifurcation for the type *II* case. 45
3.9 Hopf–saddle–node bifurcation for the type *III* case. 46
3.10 Hopf–saddle–node bifurcation for the type *IV* case. 46

5.1 Time evolution of the variables in the deterministic case of a class A laser ($\alpha = 5$). 60
5.2 x_2 versus x_1 for a class A laser ($\alpha = 5$). 61
5.3 x_2 versus x_1 for a class A laser ($\alpha = 0, 1, 5$). 62
5.4 x_2 versus x_1 for a class A laser ($\alpha = -5, -1, 0$). 62
5.5 Potential for a class A laser. 63
5.6 Potential for a class A laser and trajectory. 63
5.7 Vector field and simulation of the deterministic equations ($\alpha = 5$). . . 64
5.8 Evolution of the intensity and the potencial with time for a class A laser. 65
5.9 Vector field and simulation of the deterministic equations ($\alpha = -5$). . 65
5.10 Simulation of the dynamical equations with noise ($\alpha = 5$). 66
5.11 Phase evolution with time for a class A laser with noise ($\alpha = 5$). . . . 67
5.12 Simulation of the dynamical equations with noise ($\alpha = 0$). 67
5.13 Time evolution of the mean value of the phase ϕ in a class A laser. . 68
5.14 Probability distribution function for intensity in a class A laser (small noise parameter). 69
5.15 Probability distribution function for intensity (large noise parameter). 70
5.16 Evolution of $< I >_{st}$ with ϵ (noise parameter). 71
5.17 $< \dot{\phi} >_{st}$ versus ϵ. 72

6.1 Fixed points for the intensity for a class A laser with injected signal for different values of the amplitude of the external signal. 78
6.2 Bifurcation set for a class A laser with an injected signal ($\alpha = 2$). . . 81
6.3 Bifurcation set for a class A laser with an injected signal ($\alpha = 0$). . . 82

6.4 Period of the stable periodic orbit versus ρ. 82
6.5 Phase portraits in different regions of the bifurcation set of a class A laser. 87
6.6 Sketch of the partial bifurcation set for a class A laser with injected signal. 88
6.7 Phase portrait at region 11 of the bifurcation set. 88
6.8 Fixed points and potential evaluated at the different fixed points versus ρ. 90
6.9 Potential for a class A laser with an injected signal. 91
6.10 Simulation of the dynamical equations with noise ($\alpha = 2$) and $\rho = 0.05$. 94
6.11 Mean value of the intensity in the steady state in a class A laser with zero–detuning injected signal. 95
6.12 Time evolution of the mean value of the phase ϕ in a class A laser with injected signal. 96
6.13 Stochastic frequency shift $\Delta\omega \equiv \langle\dot{\phi}\rangle$ in a class A laser with injected signal. 97

7.1 Intensity, carriers number and potential versus time in a class B laser. 106
7.2 Enlargement of Fig. 7.1. 106
7.3 Number of carriers versus intensity. 107
7.4 Potential for a class B laser. 109
7.5 Phase of the electric field versus time in a class B laser. 110
7.6 Period versus potential for a class B laser. 111
7.7 Period versus time in a class B laser. 112
7.8 Logarithm of the potential difference versus time in a class B laser. . 115
7.9 Logarithm of the period difference versus time in a class B laser. . . . 116

8.1 Numerical bifurcation set in parameters (β, η) for a class B laser with injected signal, type II of the Hopf–saddle–node bifurcation. Saddle–node of fixed points and Hopf bifurcations. 123
8.2 Partial bifurcation set: Transversal secondary Hopf bifurcation, saddle–node bifurcation of transversal periodic orbits and period doubling bifurcation of transversal periodic orbits. 125
8.3 Phase portrait in $(E_r = Re(E), E_i = Im(E))$ of periodic orbits in the neighbourhood of the (secondary) Hopf bifurcation of T. 126
8.4 Intensity versus time for the unstable transversal torus created in the Hopf bifurcation of T periodic orbits. 126
8.5 Projections in the plane (E_r, E_i) of the orbits that exist in each side of the period doubling bifurcation. 127
8.6 Projections in the plane (E_r, E_i) of the orbits that exist in different regions of Fig. 8.15: B, F, G and H. 127
8.7 Resonance structure for the transversal and longitudinal Hopf bifurcations, together with the homoclinic bifurcation to fixed point C. . . 128
8.8 Secondary Hopf bifurcation and its resonances $p/q = \{1/2, 1/3, 1/4, ..\}$ from an estimation of the Hopf–saddle–node normal form. 129

8.9 Partial numerical bifurcation set around the 1/3 resonance. 130
8.10 Period versus β of periodic orbits inside the resonance $q = 3$. 132
8.11 Period of the orbits versus β for different values of η: (a) $\eta = -1.2$, (b) $\eta = -1$, (c) $\eta = -0.9$, (d) $\eta = -0.85$, (e) $\eta = -0.8$. 133
8.12 Phase portraits of resonance orbits, together with T and L. 134
8.13 Projections in the plane (E_r, E_i) of the orbits that exist in each side of the Hopf bifurcation of L periodic orbits. 135
8.14 Intensity versus time for the torus created at the Hopf bifurcation of L periodic orbits. 135
8.15 Blowup of 1/1 resonance of transversal T and longitudinal L orbits. . 136
8.16 Phase portraits of the Poincaré section $W = 0$ for the homoclinic bifurcation of the 1/1 transversal resonance. 137
8.17 Homoclinic bifurcation in 1/3 resonance. 137
8.18 Higher order resonance structure between 1/2 and 1/3 transversal resonance. 138
8.19 One–parameter unfolding of Andronov bifurcation. 139
8.20 T–point bifurcation. 140
8.21 Locus of homoclinic bifurcation to C fixed point, T–point, and Andronov bifurcation. 141
8.22 Final partial numerical bifurcation set for type *II* Hopf–saddle–node in laser with injected signal. 142

9.1 Responses, I_{max}, versus the normalized external frequency ω_m/ω_0 in a diode laser with pump modulation, $s = 0$ (gain saturation parameter), $\varepsilon = 0$ (spontaneous emission term). 150
9.2 Intensity versus time for different values of ω_m/ω_0. 151
9.3 Maxima of main resonances in the plane $(\omega_m/\omega_0, J_m)$ in a laser with pump modulation, $s = 0$ and $\varepsilon = 0$. 153
9.4 Maxima of main resonances: effect of s. 154
9.5 Maxima of main resonances: effect of ε. 155
9.6 Responses, I_{max} versus ω_m/ω_0, $s = 0$, $\varepsilon \neq 0$. 156
9.7 Maxima of main resonances for pump modulation: Effect of s. Comparison of analytical and numerical results. 162
9.8 Maxima of main resonances for pump modulation: Effect of ε. Comparison of analytical and numerical results. 162
9.9 Maxima of main resonances for pump modulation: Combined effect of ε and s. Comparison of analytical and numerical results. 163
9.10 Maxima of main resonances for loss modulation: Effect of s. Comparison of analytical and numerical results. 163
9.11 Maxima of main resonances for loss modulation: Effect of ε. Comparison of analytical and numerical results. 164
9.12 Maxima of main resonances for loss modulation: Combined effect of ε and s. Comparison of analytical and numerical results. 164
9.13 Equivalence of pump and loss modulation. Effect of s. 166
9.14 Equivalence of pump and loss modulation. Effect of ε. 167

Bibliografia

Adler, R. [1946]. A study of locking phenomena in oscillators. *Proc. IRE*, **34**, 351–357. Reprinted in *Proc. IEEE* **61**, 1380 [1973].

Agrawal, G.P. [1986]. Effect of gain nonlinearities on period doubling and chaos in directly modulated semiconductor lasers. *Appl. Phys. Lett.*, **49** (16), 1013–1015.

Agrawal, G.P. [1987]. Gain nonlinearities in semiconductor lasers: theory and application to distributed feedback lasers. *IEEE Journal of Quantum Electronics*, **QE-23**, 860–868.

Agrawal, G.P., and Dutta, N.K. [1986]. *Long–Wavelength Semiconductor Lasers.* New York: Van Nostrand Reinhold.

Arecchi, F.T., Lippi, G.L., Puccioni, G.P., and Tredicce, J.R. [1984]. Deterministic chaos in laser with injected signal. *Opt. Comm.*, **51**, 308.

Arnold, V. [1983]. *Geometrical Methods in the Theory of Ordinary Differential Equations.* New-York: Springer–Verlag.

Aronson, D.G., Hall, M.A., Hall, G.R., and McGehee, R.P. [1982]. Bifurcations from an invariant circle for two–parameter families of maps of the plane: A computer–assisted study. *Commun. Math. Phys.*, **83**, 303–354.

Balle, S., Colet, P., and San Miguel, M. [1991]. Statistics for the transient response of single–mode semiconductor laser gain swiching. *Physical Review A*, **43** (11), 498–506.

Bennett, S., Snowden, C.M., and Iezekiel, S. [1997]. Nonlinear dynamics in directly modulates multiple–quantum–well laser diodes. *IEEE Journal of Quantum Electronics*, **33** (11), 2076–2083.

Braza, P.A., and Erneux, T. [1990]. Constant phase, phase drift, and phase entrainment in lases with an injected signal. *Physical Review A*, **41** (11), 6470–6479.

Breuer, D., and Petermann, K. [1997]. Comparison of NRZ- and RZ- Modulation Format for 40–Gb/s TDM Standard–Fiber Systems. *IEEE Photonics Technology Letters*, **9**, 398–400.

Bykov, V.V. [1993]. The bifurcations of separatrix contours and chaos. *Physica D*, **62**, 290–299.

Cahn, J.W., and Hilliard, J.E. [1958]. Free energy of a nonuniform system. I. Interfacial free energy. *J. Chem. Phys.*, **28**, 258–267.

Chizhevsky, V.N. [2000]. Coexisting attractors in a CO_2 laser with modulated losses. *J. Opt. B: Quantum Semiclass. Opt.*, **2**, 711–717.

Chizhevsky, V.N., and Turovets, S.I. [1993]. Small signal amplification and classical squeezing near period doubling bifurcations in a modulated CO_2–laser. *Opt. Commun.*, **102**, 175–182.

Ciuchi, S., de Pasquale, F., San Miguel, M., and Abraham, N. B. [1991]. Phase and amplitude correlations in the transient evolution of a detuned laser after switch-on. *Physical Review A*, **44**, 7657.

Descalzi, O., and Graham, R. [1992]. Gradient expansion of the nonequilibrium potential for the supercritical Ginzburg–Landau equation. *Phys. Lett. A*, **170**, 84.

Descalzi, O., and Graham, R. [1994]. Nonequilibrium potential for the Ginzburg–Landau equation in the phase–turbulent regime. *Z. Phys. B*, **93**, 509–513.

Doedel, E., Fairgrieve, T., Sandstede, B., Champneys, A., Kuznetsov, Y., and Wang, S. [1997]. AUTO97: Continuation and bifurcation software for ordinary differential equations. *http://indy.cs.concordia.ca/auto/main.html.*

Drozdov, Yu.M. [1955]. Forced oscillations in the quasiconservative nonlinear systems with one degree of freedom: Examples (In Russian). *Prikladnaya Matematika i Mekhanika*, **19**, 33–40.

Erneux, T., Baer, S.M., and Mandel, P. [1987]. Subharmonic bifurcation and bistability of periodic solutions in a periodically modulated laser. *Physical Review A*, **35**, 1165–1171.

Fisher, I., Liu, Y., and Davis, P. [2000]. Synchronization of chaotic semiconductor laser dynamics on sub–ns timescales and its potential for chaos communication. *Physical Review A*, **62**, R011801.

Gallagher, D.F.G., White, I.H., Carroll, J.E., and Plumb, R.G. [1985]. Gigabit pulse position bistability in semiconductor lasers. *L. Lightwave Technology*, **LT-5**, 1391–1398.

Gard, T.C. [1987]. *Introduction to Stochastic Differential Equations.* Monographs and Textbooks in Pure and Applied Mathematics, vol. 114. Marcel Dekker.

Gardiner, C.W. [1985]. *Handbook of Stochastic Methods.* Springer–Verlag.

Gavrielides, A., Kovanis, V., and Erneux, T. [1997]. Analytical stability boundaries for a semiconductor laser subject to optical injection. *Optics Communications*, **136**, 253–256.

Glendinning, P., and Sparrow, C. [1986]. T–points: a codimension two heteroclinic bifurcation. *Journal of Statistical Physics*, **43**, 479–488.

Goedgebuer, J.P., Larger, L., and Porte, H. [1998]. Optical cryptosystem based on synchronization of hiperchaos generated by a delayed feedback tunable laser diode. *Phys. Rev. Lett.*, **80**, 2249–2252.

Graham, R. [1987]. Weak noise limit and nonequilibbrium potential of dissipative dynamical systems. *Instabilities and Nonequilibrium Structures.*

Graham, R. [1991]. Nonequilibrium potentials in spatially extended pattern forming systems. *Instabilities and Nonequilibrium Structures III.*

Greiner, A., Strittmatter, W., and Honerkamp, J. [1988]. Numerical integration of stochastic differential equations. *J. Stat. Phys*, **51** (1/2), 95–108.

Guckenheimer, J., and Holmes, P. [1983]. *Nonlinear Oscillations, Dynamical Systems and Bifurcations of Vector Fields.* New York: Springer–Verlag.

Gunton, J.D., San Miguel, M., and Sahni, P. [1983]. The dynamics of first order phase transitions. *Phase Transitions and Critical Phenomena*, **8**.

Haken, H. [1983]. *Synergetics.* Springer–Verlag.

Haken, H. [1984]. *Laser Theory.* Springer–Verlag.

Haken, H. [1985]. *Light.* Laser Light Dynamics, vol. 2. Amsterdam: North–Holland.

Haken, H., and Sauermann, H. [1963]. Nonlineal interactions of laser modes. *Z. Phys.*, **173**, 261.

Haug, H. [1969]. Quantum–mechanical rate equations for semiconductor lasers. *Physical Review*, **184** (2), 338–348.

Hecht, E., and Zajac, A. [1986]. *Óptica.* Addison–Wesley Iberoamericana.

Hemery, E., Chusseau, L., and Lourtioz, J.M. [1990]. Dynamical behaviors of semiconductor lasers under strong sinusoidal current modulation: Modelling and experiment at 1.3μm. *IEEE Journal of Quantum Electronics*, **26**, 633–641.

Henry, C.H. [1982]. Theory of the linewidth of semiconductor lasers. *IEEE Journal of Quantum Electronics*, **QE-18** (2), 259–264.

Henry, C.H. [1983]. *IEEE Journal of Quantum Electronics*, **QE-19**, 1391.

Hernández-García, E., Toral, R., and San Miguel, M. [1990]. Intensity correlation functions for the colored gain–noise model of dye lasers. *Physical Review A*, **42** (11), 6823–6830.

Hilborn, R.C. [1994]. *Chaos and Nonlinear Dynamics.* New York: Oxford University Press.

Hirschberg, P., and Laing, C. [1995]. Succesive homoclinic tangencies to a limit cycle. *Physica D*, **89**, 1–14.

Hohenberg, P.C., and Halperin, B.I. [1977]. Theory of dynamical critical phenomena. *Rev. Mod. Phys.*, **49**, 435–485.

Homar, V.M. 1996. *Semiconductor Laser Dynamics under Feedback and Modulation. Single and Multimode Operation.* Ph.D. thesis, Universitat de les Illes Balears.

Hori, Y., Serizawa, H., and Sato, H. [1988]. Chaos in a directly modulated semiconductor lasers. *J. Opt. Soc. Am. B*, **5** (5), 1128–1132.

Jackson, E.A. [1989]. *Perspectives of Nonlinear Dynamics.* Cambridge: Cambridge University Press.

Kao, Y.H., and Lin, H.T. [1993]. Virtual Hopf precursor of period doubling route in directly modulated semiconductor lasers. *IEEE J. Quantum Electronics*, **29**, 1617–1623.

Katz, A.M. [1955]. Forced oscillations in the quasiconservative nonlinear systems with one degree of freedom (In Russian). *Prikladnaya Matematika i Mekhanika*, **19**, 13–32.

Kawaguchi, H. [1994]. *Bistabilities and Nonlinearities in Laser Diodes.* Boston-London: Artech House.

Kirk, V. [1991]. Breaking of symmetry in the saddle–node Hopf bifurcation. *Physics Letters A*, **154**, 243–248.

Kloeden, P.E., and Platen, E. [1992]. *Numerical Solution of Stochastic Differential Equations.* Berlin: Springer–Verlag.

Krauskpof, B., Wieczork, S., and Lenstra, D. [2000]. Routes to chaos in an optically injected semiconductor laser. *Proceedings of SPIE*, **3944**, 612–619.

Kressel, M.P., and Ippen, E.P. [1987]. *Appl. Phys. Lett.*, **51**, 1765.

Kuznetsov, Y. [1997]. *Elements of Applied Bifurcation Theory.* Series of Applied Mathematical Sciences, vol. 112. Springer.

Lamb, W.E. [1964]. Theory of optical masers. *Phys Rev.*, **134**, 1429–1450.

Lamela, H., Carpintero, G., and Mancebo, F. [1998a]. Period tripling and chaos in the dynamic behavior of directly modulated diode lasers. *IEEE Journal of Quantum Electronics*, **34** (10), 1797–1801.

Lamela, H., Carpintero, G., and Acebo, P. [1998b]. Truncation of the Feigenbaum sequence in directly modulated semiconductor lasers. *IEEE Journal of Quantum Electronics*, **34** (3), 491–496.

Lee, C.-H., and Shin, S.-Y. [1989]. Transformation of rate equations and approximate transient solutions for semiconductor lasers. *IEEE Journal of Quantum Electronics*, **25** (5), 878–884.

Lim, C.G., Iezekiel, S., and Snowden, C.M. [2000]. Is noise a crucial factor in rate equation modeling of nonlinear dynamics in laser diodes? *Applied Physics Letters*, **77**, 3493–3495.

Liu, H.F., and Ngai, W.F. [1993]. Nonlinear dynamics of a directly modulated 1.55 μm InGaAsP distributed feedback semiconductor laser. *IEEE Journal of Quantum Electronics*, **29** (6), 1668–1675.

Lyapunov, A.M. [1992]. *Stability of Motion.* London: Taylor & Francis.

Matsui, Y., Kutsuzawa, S., Arahira, S., Ogawa, Y., and Suzuki, A. [1998]. Bifurcation in 20–Ghz gain–switched 1.55–μm MQW lasers and its control by CW injection seeding. *IEEE Journal of Quantum Electronics*, **34**, 1213–1223.

Milshtein, G.N. [1974]. Approximate integration of stochastic differential equations. *Theory Prob. Appl.*, **19**, 557–562.

Milshtein, G.N. [1978]. A method of second order accuracy integration of stochastic differential equations. *Theory Prob. Appl.*, **23**, 396–401.

Mirasso, C.R., Colet, P., and San Miguel, M. [1993]. Dependence of time jitter on bias level for single–mode semiconductor lasers under high speed modulation. *IEEE Journal of Quantum Electronics*, **29**, 23–31.

Mirasso, C.R., Colet, P., and García-Fernández, P. [1996]. Synchronization of chaotic semiconductor lasers: Application to encoded communications. *Phot. Tech. Lett.*, **8**, 299–301.

Montagne, R., Hernández-García, E., and San Miguel, M. [1996]. Numerical study of a Lyapunov functional for the complex Ginzburg–Landau equation. *Physica D*, **96**, 47–65.

Nizette, M., and Erneux, T. [1999]. Injection locked semiconductor lase dynamics from large to small detunings. *Physics and Simulation of Optoelectronic Devices VII. Eds., Proc. SPIE 3625*, 679–691.

Novikov, E.A. [1964]. *Zh. Eksp. Teor. Fiz.*, **47**, 1919.

Novikov, E.A. [1965]. *Soviet Physics JETP*, **20**, 1290–1294.

Olshansky, R., Su, C.B., Manning, J., and Powazinik, W. [1984]. Measurement of radiative and nonradiative recombination rates in InGaAsP and AlBaAs light sources. *IEEE Journal of Quantum Electronics*, **QE-20**, 838–854.

Oppo, G-L., Politi, A., Lippi, G-L., and Arecchi, F.T. [1986]. Frecuency pushing in lasers with injected signal. *Physical Review A*, **34** (5), 4000–4007.

Oppo, G.L., and Politi, A. [1985]. Toda potential in laser equations. *Zeitschrift für Physik B - Condensed Matter*, **59**, 111–115.

Petermann, K. [1988]. *Laser Diode Modulation and Noise.* Dordrecht: Kluwer Academic Publishers.

Risken, H. [1989]. *The Fokker–Plank Equation.* Springer–Verlag.

Saleh, B.E.A., and Teich, M.C. [1991]. *Fundamentals of Photonics.* New York: Wiley.

Samson, A.M., and Turovets, S.I. [1987]. Hierarchy of bifurcations in a laser with periodic modulation of losses. *Doklady AN BSSR*, **31**, 888–890.

Samson, A.M., Logvin, Yu.A., and Turovets, S.I. [1990]. Therole of potential symmetry and shape of a nonlinear oscillator in the bifurcation hierarchy for harmonic action. *Sov. Radiophysics and Quantum Electronics*, **33**, 40–50.

Samson, A.M., Turovets, S.I., Chizhevsky, V.N., and Churakov, V.V. [1992]. Nonlinear dynamics of a loss–switched CO_2 laser. *Sov. Phys. JETP*, **74** (4), 628–639.

San Miguel, M., and Sagues, F. [1987]. Dynamics of transient pattern formation in nematic liquid crystals. *Physical Review A*, **36**, 1883–1893.

San Miguel, M., and Toral, R. [1997]. *Stochastic effects in physical systems in Instabilities and Nonequilibrium Structures VI.* Kluwer acad. pub. edn. E. Tirapegui and W. Zeller.

San Miguel, M., Montagne, R., Amengual, A., and Hernández-García, E. [1996]. *Instabilities and Nonequilibrium Structures V.* Kluwer acad. pub. edn. E. Tirapegui and W. Zeller.

Sancho, J.M., San Miguel, M., Katz, S.L., and Gunton, J.D. [1982]. Analytical and numerical studies of multiplicative noise. *Physical Review A*, **26**, 1589–1609.

Sargent, M., Scully, M.O., and Lamb, W.E. [1974]. *Laser Physics.* Reading Mass. Addison–Wesley Publ. Comp.

Schecter, S. [1987]. The saddle–node separatrix–loop bifurcation. *SIAM J. Math. anal.*, **18**, 1142–1156.

Schwartz, I.B. [1988]. Infinite primary saddle–node bifurcation in periodically forced systems. *Phys. Lett. A*, **126** (7), 411–418.

Schwartz, I.B., and Erneux, T. [1994]. Subharmonic hysteresis and period doubling bifurcations for a periodically driven laser. *SIAM J. Appl. Math.*, **54** (4), 1083–1100.

Simpson, T., Liu, J.M., Huang, K.F., and Tai, K. [1997]. Nonlinear dynamics induced by external optical injection in semiconductor lasers. *Quantum Semiclass. Opt.*, **9**, 765–784.

Solari, H.G., and Oppo, G-L. [1994]. Laser with injected signal: Perturbation of an invariant circle. *Optics Communications*, **111**, 173–190.

Solari, H.G., Natiello, M.A., and Mindlin, G.B. [1996]. *Nonlinear Dynamics. A two way trip from physics to math.* London: Institute of Physics Publishing.

Sparrow, C., and Swinnerton-Dyer, H.P.F. [1995]. The Falkner–Skan equation I: creation of strange invariant sets. *Journal of Differential Equations*, **199** (2), 336–394.

Statz, H., and deMars, G.A. [1960]. *Quantum Electromics.* New York: C. H. Townes. Colombia University Press.

Strogatz, S.H. [1994]. *Nonlinear Dynamics and Chaos.* Reading: Addison–Wesley Publ. Co.

Svelto, O. [1982]. *Principles of Lasers.* New York: Plenum Press.

Tang, C.L., Statz, H., and deMars, G.A. [1963]. Spectral output and spiking behavior of solid state lasers. *J. Appl. Phys.*, **34**, 2289–2295.

Tang, M., and Wang, S. [1986]. Simulation studies of bifurcation and chaos in semiconductor laser. *Appl. Phys. Lett.*, **48** (14), 900–902.

Tang, M., and Wang, S. [1987]. Simulation studies of dynamical behaviour of semiconductor laser with Auger recombination. *Appl. Phys. Lett.*, **50**, 1861–1863.

Toral, R., and Chakrabarti, A. [1993]. Generation fo Gaussian distributed random numbers by using a numerical version method. *Comp. Phys. Comm.*, **74**, 327.

Tredicce, J.R., Arecchi, F.T., Lippi, G-L., and Puccioni, G.P. [1985a]. Instabilities in lasers with an injected signal. *Journal of the Optical Society of America B*, **2**, 173.

Tredicce, J.R., Abraham, N.B., Puccioni, G.P., and Arecchi, F.T. [1985b]. On chaos in lasers with modulated parameters: a comparative analysis. *Optics Communications*, **55**, 131–134.

Šil'nikov, L.P. [1965]. A case for the existance of a denumerable set of periodic motions. *Sov. Math. Dokl.*, **6**, 163–166.

Šil'nikov, L.P. [1966]. On the generation of a periodic motion from a trajectory which leaves and re–enters a saddle–saddle state of equilibrium. *Sov. Math. Dokl.*, **7**, 155–1158.

van der Graaf, W.A. 1997. *Nonlinear Dynamics of Semiconductor Lasers Driven by External Optical Fields.* Ph.D. thesis, Amsterdam.

van Kampen, N.G. [1981]. *Stochastic Processes in Physics and Chemistry.* North–Holland.

van Tartwijk, G.H.M., and Lenstra, D. [1995]. Semiconductor lasers with optical injection and feedback. *Quantum Semiclass. Opt.*, **7**, 87–143.

Wada, K., Marui, H., Horinaka, H., and Cho, Y. [1998]. Disappearance of chaos on a 0.8 μm AlGaAs Fabry–Perot semiconductor laser modulated near the relaxation oscillation frequency. *Optics Communications*, **155**, 301–305.

Weiss, C.O., and Vilaseca, R. [1991]. *Dynamics of Lasers.* Weinhemim: VCH Publishers.

Wieczorek, S., Krauskopf, B., and Lenstra, D. [2000a]. Global view of complicated dynamics in optically injected semiconductor lasers. *Procedings of SPIE*, **3944**, 602–611.

Wieczorek, S., Krauskopf, B., and Lentra, D. [2000b]. Mechanism for multistability in a semiconductor laser with optical injection. *Optics communications*, **183** (1-4), 215–226.

Wieczorek, S., Krauskopf, B., and Lenstra, D. [2000c]. A unifying view of bifurcations in semiconductor lasers subject to optical injection. *Optics Communications*, **172**, 279–295.

Wiggins, S. [1991]. *Introduction to Applied Nonlinear Dynamical Systems and Chaos.* Vol. 2. Springer–Verlag.

Wilson, J., and Hawkes, J.F.B. [1989]. *Optoelectronics, An Introduction.* 2nd edn. Cambridge: Prentice Hall.

Yang, Y.M., and Liu, H.F. 2001. *Control of period doubling in modulated semiconductor lasers and its application to all–optical clock division.* Tech. rept. Paper 4283-47. Photonic West 2001, San José, USA.

Yeung, M.K.S., and Strogatz, S. [1998]. Nonlinear dynamics of a solid–state laser with injection. *Physical Review E*, **58**, 4421–4435.

Yoon, T.H., Lee, C.H., and Shing, S.Y. [1989]. Perturbation analysis of bistability and period doubling in directly–modulated laser diodes. *IEEE Journal of Quantum Electronics*, **25**, 1993–2000.

Zimmermann, M.G., and Natiello, M.A. [1998]. Homoclinic and heteroclinic bifurcations close to a twisted heteroclinic cycle. *International Journal of Bifurcation and Chaos*, **8**, 359.

Zimmermann, M.G., Natiello, M.A., and Solari, H.G. [1997]. Šil'nikov–saddle–node interaction: laser with injected signal. *Physica D*, **109**, 293–314.

Zimmermann, M.G., Natiello, M.A., and Solari, H.G. [2001]. Global bifurcations in a laser with injected signal: beyond Adlers approximation. *Chaos*, **11**, 500–513.

Currículum

FORMACIÓ ACADÈMICA

- LLICENCIATURA: Ciències Físiques. Universitat de les Illes Balears (UIB). Juny de 1996.
- Memòria d'Investigació. UIB. Març de 2000.
- Suficiència Investigadora. UIB. Juliol de 2000.

ASISTÈNCIA A CURSOS I REUNIONS

- "VI Curso de Introducción a la Investigación en Óptica" al **Instituto de Óptica Daza de Valdés (CSIC)**. Madrid, 11 i 12 d'abril de 1996. Rebut borsa de viatge.
- Curs d'estiu de la **Fundación General de la UCM** : "Iniciación a los Sistemas Dinámicos". San Lorenzo de El Escorial, 7 a 11 de juliol de 1997. Dirigit per Rafael de la Llave Canosa. Modalitat becària.
- Participació en el curs de la **7th Jyväskylä International Summer School**: "Introduction to extended dynamical systems". Jyväskylä, Finlàndia, 11 a 15 d'agost de 1997. Prof. T. Gallay. Rebut beca del programa EU TMR.
- Asistència a la "III Reunión Barcelona–Palma de Física Estadística y No Lineal". Barcelona, 30 i 31 de gener de 1998.
- Asistència al curs: " Optical solitons: theoretical challenges and industrial perspectives" al Centre de Physiques des Houches. Les Houches, França, 28 de setembre a 2 d'octubre de 1998. Rebut beca del programa EU TMR.
- Participació en l'escola internacional: "Space time chaos: characterization, control and synchronization". Instituto de Física, Universidad de Navarra. Pamplona, 19 a 23 de juny de 2000.
- Curs d'estiu de la **Fundación General de la UCM** : "Hitos matemticos de finales del siglo XX". San Lorenzo de El Escorial, 6 al 10 d'agost de 2001. Dirigit per Carlos Andradas. Modalitat becària.

CURSOS DE DOCTORAT

- Sistemes dinàmics (3 c). Curs 1996-97. UIB
- Mecànica estadística: Transicions de fase (3 c). Curs 1996-97. UIB
- Introducció a la dinàmica no lineal de làsers (2 c). Curs 1996-97. UC
- Introducció als làsers de semiconductor (2 c). Curs 1996-97. UC
- Làsers de semiconductor per a comunicaciones òptiques (2 c). Curs 1996-97. UC
- Mètodes de simulació numèrica en física. (3 c). Curs 1997-98. UIB
- Dinàmica d'estructures espaciotemporals (5 c). Curs 1997-98. UIB

ALTRES CURSOS DE DOCTORAT – ESPECIALIZACIÓ

- Solitons en comunicacions òptiques (2 c). Prof. L. Pesquera. 2 i 3 de juny de 1998. UC
- Solitons òptics espacials: propietats i aplicacions a dispositius fotònics (2 c). Prof. Ll. Torner. 4 i 5 de juny de 1998. UC
- Tècniques de supercomputació. Prof. J. Massó. Juliol de 1998. UIB

COMUNICACIONS

- C. Mayol, R. Toral i C. R. Mirasso, "A Lyapunov potential description for laser dynamics" (pòster); *VIII Reunión de Física Estadística, FISES '97.* Getafe, Madrid. 25 a 27 de setembre de 1997.
- C. Mayol, R. Toral i C. R. Mirasso, "A Lyapunov potential description for semiconductor lasers" (pòster); Centre de Physique des Houches, Les Houches, França, 28 de setembre a 2 d'octubre de 1998.
- C. Mayol, S.I. Turovets, R. Toral, C.R. Mirasso i L. Pesquera, "Asymptotic theory of instabilities in directly modulated semiconductor lasers", *Semiconductor and Integrated Optoelectronics 2000 Conference (SIOE '2000)*, Cardiff, UK, 17 a 19 d'abril de 2000.
- C. Mayol, M.A. Natiello i M.G. Zimmermann, "Laser with injected signal (LIS): small detuning" (pòster), Escuela internacional sobre *Space time chaos: characterization, control and synchronization.* Universidad de Navarra, Pamplona, 19 a 23 de juny de 2000.

- C. Mayol, S.I. Turovets, R. Toral, C.R. Mirasso i L. Pesquera, "Asymptotic Theory of Instabilities in Directly Modulated Semiconductor Lasers" (pòster), *International Quantum Electronics Conference (IQEC '00)*, Niza, França, 10 a 15 de setembre de 2000.

- C. Mayol, S.I. Turovets, R. Toral, C.R. Mirasso i L. Pesquera, "Asymptotic Theory of Instabilities in Directly Modulated Semiconductor Lasers" (pòster), *X Reunión de Física Estadística, FISES 2000.* Santiago de Compostela, Espanya. 21 a 23 de setembre de 2000.

PUBLICACIONS DE PRESENTACIONS EN CONGRESSOS

- C. Mayol, R. Toral, and C.R. Mirasso, "A Lyapunov Potential for Laser Dynamics". Proceeding of the *VIII Reunión de Física Estadística, FISES '97*, Anales de Física, Monografías 4 RSEF (1998). pàg. 271-272.

- C. Mayol, S.I. Turovets, R. Toral, C.R. Mirasso, and L. Pesquera, "Asymptotic Theory of Instabilities in Directly Modulated Semiconductor Lasers". Technical Digest of SIOE '2000. Paper Poster 47.

- C. Mayol, S.I. Turovets, R. Toral, C.R. Mirasso, and L. Pesquera, "Asymptotic Theory of Instabilities in Directly Modulated Semiconductor Lasers". Conference Digest of IQEC '00. Paper Poster QTuE4.

- C. Mayol, S.I. Turovets, R.Toral, C.R. Mirasso, and L. Pesquera, "Asymptotic Theory of Instabilities in Directly Modulated Semiconductor Lasers". Llibre del congrés FISES 2000. *X Congreso de Física Estadística.* Setembre 2000. pàg. 128.

PUBLICACIONS EN REVISTES AMB "REFEREE"

- C. Mayol, R. Toral, and C.R. Mirasso, "Lyapunov Potential Description for Laser Dynamics". Physical Review A, **59**, 4690–4698 (1999).

- C. Mayol, S.I. Turovets, R. Toral, C.R. Mirasso, and L. Pesquera, "Main Resonances in Directly Modulated Semiconductor Lasers: Effect of Spontaneous Emission and Gain Saturation". IEE Proc.–Optoelectronics, **148** (1), 41–45 (2001).

- C. Mayol, M.A. Natiello, and M.G. Zimmermann, "Resonance structure in a weakly detuned laser with injected signal", International Journal of Bifurcation and Chaos, **11** (10), 2587–2605 (2001).

- C. Mayol, R. Toral, C.R. Mirasso, S.I. Turovets, and L. Pesquera, "Theory of Main Resonances in Directly Modulated Diode Lasers". Acceptat a IEEE Journal of Quantum Electronics, a publicar–se el març de 2002.

- C. Mayol, R. Toral, C.R. Mirasso, and M. Natiello, "Class *A* lasers with injected signal: bifurcation set and Lyapunov potential function". Enviat a Physical Review E (2002).

ESTADES ALTRES CENTRES

- Estada predoctoral, Programa de Formació de Professorat Universitari. Departament de Matemàtiques, *Lunds Tekniska Hogskola*, Lund, Suècia. 6 d'agost a 29 d'octubre de 1999 (12 setmanes). Prof. responsable: Mario Natiello.
- Departamento de Física Moderna. Universidad de Cantabria, Santander. Estada mitjançant el conveni entre la Universidad de Cantabria i la Universitat de les Illes Balears. 13 a 26 de març de 2000 (2 setmanes). Prof. responsables: Luis Pesquera i Sergei I. Turovets.
- Estada predoctoral, Programa de Formació de Professorat Universitari. Departament de Matemàtiques, *Lunds Tekniska Hogskola*, Lund, Suècia. 27 d'abril a 19 de maig de 2000 (3 setmanes). Prof. responsable: Mario Natiello.